ABSTRACT

Title of Dissertation: ELECTROMAGNETIC PROPERTIES OF TOPOLOGICAL QUANTUM MATERIALS

Yahya Alavirad
Doctor of Philosophy, 2020

Dissertation Directed by: Professor Jay Deep Sau
Department of Physics

In the past few decades, research into electromagnetic properties of topological quantum materials has been one of the most active research areas in the field of condensed matter physics. Physicists have discovered a large class of materials, e.g. Weyl semimetals, topological insulators, and topological superconductors that can host a plethora of interesting topological properties. In addition to their theoretical value as novel and exotic phases of quantum matter, topological quantum materials provide a promising platform for an array of technological applications, particularly as building blocks of topological quantum computers. Unfortunately, despite great progress in the theoretical understanding of topological phases of matter, practical problems have made it difficult to: (i) identify unambiguous examples of topological quantum material and (ii) harness their potential for technological applications. The overarching goal of this thesis is to understand such difficulties and to find ways to overcome them by studying specific problems.

This thesis is divided into four independent parts, each of which is dedicated to a particular problem: In the first part, we study chiral magnetic effect in Weyl

semimetals and discuss whether it can be used to probe topological properties of Weyl semimetals in real experiments.

In the second part, we propose an experimental setup to realize a certain type of topological excitation called $\mathbb{Z}_3$ parafermionic zero mode using a quantum dot array structure from the 2/3 fractional quantum Hall state. Importantly, our proposal does not rely on Andreev backscattering. We argue that this feature makes our proposal suitable for experimental realization.

In the third part, we provide a quantitative analysis of supercurrent in superconductor/quantum Hall/superconductor junctions and show that by making critical assumptions about the interface, it is possible to obtain a quantitative agreement between theory and the magnitude of the observed supercurrent.

In the fourth part, we study quantum anomalous Hall effect and flavor ferromagnetism in twisted bilayer graphene and argue that the one-magnon spectrum can be used as a numerically accessible tool to study the stability of the quantum anomalous Hall phase in twisted bilayer graphene.

ELECTROMAGNETIC PROPERTIES OF TOPOLOGICAL QUANTUM MATERIALS

by

Yahya Alavirad

Dissertation submitted to the Faculty of the Graduate School of the
University of Maryland, College Park in partial fulfillment
of the requirements for the degree of
Doctor of Philosophy
2020

Advisory Committee:
Professor Jay Deep Sau, Chair/Advisor
Professor Maissam Barkeshli
Professor Theodore Einstein
Professor Mohammad Hafezi
Professor Christopher Jarzynski

Acknowledgments

I am incredibly grateful to many colleagues and friends that I interacted with during my time at UMD, without them this thesis would not be possible. First, I'd like to thank my advisor, Jay Sau for his mentorship and support. He has always made himself available for help and advice. I have learnt a lot from his creativity and breadth of knowledge.

I would also like to thank Maissam Barkeshli for many interesting discussions and enjoyable collaborations. Working with him showed me an entirely new and fascinating side of research in condensed matter physics. It has been a great pleasure to work with and learn from him.

I am also grateful to Sankar Das Sarma for his support, and providing valuable advice on my career direction.

I would like to thank Professors Ted Einstein, Mohammad Hafezi, and Christopher Jarzynski for serving on my dissertation committee.

I have benefited immensely from discussions with many postdoctoral researchers and PhD students at UMD Mohammad Maghrebi, Alireza Seif, Setiawan, Hoi-Yin Hui, Juraj Radic, Amit Nag, Yingyi Huang, Tamoghna Barik, Aydin Keser, Ali Hamed Mousavian, Fatholah Salehi, Chunxiao Liu, Will Cole, David Clarke, Junhyun Lee, Jed Pixley, Ching-Kai Chiu, Fengcheng Wu, Xiaopeng Li, Bitan Roy, Philip Brydon, and many others. I would especially like to thank Ali Lavasani and Kasra Hejazi who have been among my closest friends for the better part of the past decade.

Finally, I want to thank my parents, sisters, and wife for their unconditional love and support. My moms constant support and encouragement has been the most unwavering constant of my life. I am extremely indebted to my wife Shakiba Rafiee who has shared every single delightful and stressful moment in my PhD. I would have not made it so far without her love, friendship and support.

Table of Contents

List of Tables

List of Figures

List of Abbreviations

CME	Chiral Magnetic Effect
DMRG	Density Matrix Renormalization Group
FQH	Fractional Quantum Hall
QAH	Quantum Anomalous Hall
QH	Quantum Hall
QHE	Quantum Hall Effect
MZM	Majorana zero mode
PZM	Parafermionic zero mode
SC	Superconductor
SPT	Symmetry-Protected Topological
TBLG	Twisted-Bilayer Graphene
TI	Topological Insulator
TSC	Topological Superconductor

Chapter 1: Introduction

1.1 Introduction to topological quantum material

Topological phases can be roughly defined as distinct phases of matter (i.e. they cannot be smoothly connected) that do not break any symmetries. The first theoretical example of topological matter dates back to the Su-Schrieffer-Heeger model in the 1970s [2]. Later on, experimental discovery of the quantum Hall effect (QHE) in 1980s provided the first and perhaps, even to this day, the most striking example of experimentally realizable topological quantum phases [3]. Prior to the discovery of "topological quantum matter" phases of matter were thought to be classified only using patterns of symmetry and symmetry breaking known as the Landau paradigm. However, topological phases are beyond the Landau theory as distinct topological phases do not break any symmetries.

In the decades following the discovery of QHE, it was realized to topological phases of matter offer fascinating technological applications. Specifically, their potential application in building topological quantum computers has led to a surge of renewed interest in topological quantum material. However, despite the fascinating possibilities, harnessing their power to build realistic topological quantum bits has proven to be extremely difficult. Furthermore, since the direct observation of topo-

logical features is usually difficult, establishing the existence of a topological phase has to rely on indirect experimental evidence, which in turn, demands research into finding experimentally viable probes of topological phases. The goal of this thesis is to understand these problems and to take steps towards solving them by studying specific examples of topological quantum materials.

Recently, the class of theoretical models and experimental materials that host a wide range of interesting topological phenomena has grown significantly. In the following, we briefly review different major classes of topological quantum materials with an emphasis on what is relevant for this thesis.

1.1.1 Symmetry-protected topological phases

Symmetry-protected topological (SPT) phases can be defined as gapped phases of quantum matter that cannot be adiabatically deformed into a trivial product state without breaking the symmetry or closing the bulk gap. SPTs are gapped (insulating) in the bulk, while usually (if the boundary does not break the symmetry) possessing robust gapless surface states.

Topological insulators (TI) and topological superconductors (TSC) are both examples of SPT phases. A particularly intriguing feature of TSCs is that edge states of one-dimensional TSCs or vortices of two-dimensional TSCs can host Majorana zero modes, which are particle-like excitations with non-Abelian statistics [4]. Non-Abelian statistics makes these systems particularly interesting due to their potential application in building topological quantum computers [4]. Most of the promising

routes to realize TSCs rely on an architecture that uses a regular TI in proximity to a normal superconductor (SC).

In chapter 3 we present a realistic experimental proposal to realize a generalization of MZMs (parafermionic zero modes) using a hybrid fractional QH-SC structure. In chapter 4 we study SC/QH/SC Josephson junctions quantitatively. Understanding the SC/QH interfaces is an important step towards realizing a large class of exotic topological phases in a lab.

1.1.2 Topological order

Analogous to SPTs, topologically ordered phases can be defined as gapped phases of quantum matter that cannot be adiabatically deformed into a trivial product state without closing the bulk gap. However, note that topologically ordered phases crucially do not rely on the symmetries protecting them. Topologically ordered phases have a number of interesting properties that are absent in SPTs, including a ground-state degeneracy that depends on the topology of the underlying manifold, existence of charged fractional excitations in the bulk and non-local patterns of entanglement.

Fractional quantum Hall (FQHE) states and the $\mathbb{Z}_2$ gauge theory (toric-code) provide the best known examples of topologically ordered phases. At this time, FQH states seem to be the only unambiguous example of a topologically ordered phase that has been observed in nature.

As mentioned earlier, in chapter 3, we present a realistic proposal to realize

parafermionic zero modes that relies on crucial features of FQH states.

1.1.3 Topological semimetals

While most of the theory of the topological phase is only applicable to gapped phases, it is still possible to see at least remnants of topology in gapless systems. The best known example of topology in gapless systems is provided by Weyl semimetals. Weyl semimetals are 3D material whose electronic dispersion exhibits point nodes at the Fermi level, and the low-energy physics is effectively described by a Weyl Hamiltonian. A striking feature of the Weyl semimetals is the existence of gapless surface Fermi arcs which can be thought of as edges states of 2D gapped Chern insulators that are present at a fixed value of momentum along a particular direction and are therefore topological in nature.

A combination of intriguing topological properties and experimental accessibility has led to a surge of interest in Weyl semimetals in the past decade.

In chapter 2, we study the chiral magnetic effect, which was originally proposed as a signature of topology in Weyl semimetals and argue that in fact, it cannot serve as a probe of topology in topological semimetals.

1.2 Organization of thesis

The rest of this thesis interpolates material from four papers by the author [5–8]. Each of the following chapters is meant to be rather self-contained and independent from the rest of the thesis. Chapter 2 is based on [5] and is devoted to a detailed

study of chiral magnetic effect in Weyl semimetals, in particular, we are interested in the role of topology and disorder in chiral magnetic effect. Chapter 3 is based on [6] and presents an original experimental proposal that realizes $\mathbb{Z}_3$ parafermionic zero modes from a quantum dot array of 2/3 filled FQH states that is in proximity to a superconductor. Chapter 4 is based on [7] and provides a detailed, quantitive study of supercurrent in SC/QH/SC junctions and emphasizes the role of the chiral nature of edges states in supercurrents that exist in the quantum Hall regime. Chapter 5 is based on [8], which provides a detailed study of quantum anomalous Hall ferromagnetism in twisted bilayer graphene and argues in favor of using the one-magnon spectrum as a probe of the stability of flavor ferromagnetism in nearly flat-band systems. Chapter 6 provides a summary and conclusion.

Chapter 2: Chiral Magnetic Effect in Weyl Semimetals

2.1 Introduction

Weyl semimetals, which are three-dimensional analogues of graphene, have generated a lot of interest in the past decade because of the combination of their peculiar properties [9–13] and experimental accessibility [14–19]. Unlike graphene, the gapless nature of the Weyl points in the energy spectrum of a Weyl semimetal are protected by topology through the presence of a non-zero Berry flux in momentum space [12]. The non-zero Berry flux has certain unique characteristics such as chiral Landau levels when subjected to a magnetic field [20, 21]. Electrons in the zero energy Landau levels in a Weyl semimetal propagate either parallel or antiparallel to the magnetic field and can form a closed loop only with the aid of Fermi arc states on the surface of the Weyl semimetals [12]. Recently some evidence for such Fermi arcs [22] and the chiral Landau levels [23] has become available. However, the Landau-level trajectories of electrons by themselves do not form a macroscopic response function that can be measured without direct reference to the single electrons. On the other hand, the topological Berry flux in Weyl semimetals is also predicted to give rise to a such a response through the so-called "chiral anomaly" in three dimensions known from quantum field theory [10, 24]. It has been shown

that this chiral anomaly could be applicable to Weyl semi-metals in the solid state systems in the form of the "chiral magnetic effect" (CME) [25–33].

The CME, which is originally a prediction from the continuum field theory of Weyl Fermions in three dimensions, has been the subject of some debate when applied to solid state systems on a lattice. Lattice regularization itself is known to limit Weyl points to exist in pairs so as to ensure the vanishing of the total Berry flux in momentum space. Denoting the separation in energy of a pair of such Weyl points by δk_0, the CME predicts a current $\mathbf{j} = \left(\frac{e}{2\pi}\right)^2 \delta k_0 \mathbf{B}$ in response to the application of a static magnetic field $\mathbf{B}$. This is a rather unusual prediction since in the solid state, with the exception of superconductors, the flow of a current always requires an applied electric field. The subtle nature of the field theory prediction was further substantiated by the demonstration of regularization schemes where the CME would not occur in Weyl semimetals [30, 31]. Using different limits from field theory, a variety of other conclusions were reached for the existence of the CME, such as a critical momentum-space separation of the Weyl points [33], and presence of a gap [32]. Semiclassical analysis [27, 28] of the magnetic field response also concluded the CME to be absent in Weyl semimetals. Following this, direct (numerical) linear response calculations of CME for specific lattice models [26, 29] of Weyl semimetals, it is concluded that the CME can indeed occur as predicted by field theory in the appropriate momentum and frequency limit. However, the numerical confirmation of the CME by linear response studies of lattice models does not address the counter-intuitive nature of the CME, i.e. how a current can flow in response to just a magnetic field. In fact, Vazifeh and Franz [25] and later

Yamamoto [34] have shown rigorously that the current in thermal equilibrium in any solid state material must vanish in the absence of an electric field, which would automatically constrain the CME to vanish.

A finite frequency analog of CME can be defined as the current flowing parallel to a time-dependent magnetic field $\mathbf{j} = \sigma(\omega)\mathbf{B}(\omega)$, finite frequency CME can be computed by considering the corresponding component of the linear response at finite frequency. However, the finite-frequency analog of the CME is indistinguishable from a non-colinear response to the electric field induced by the time-dependent magnetic field. As a result, so far studies of CME have been limited to the static and homogeneous case of $\omega, \mathbf{q} \to 0$ (we discuss the order of limits in more detail in Sec. 2.3.2) and an explicit calculation of finite frequency CME in Weyl semimetals is lacking. While the focus of our work is the more counterintuitive case of the DC limit of a magnetic field, we do find that the finite frequency response also bears interesting signatures of the Berry curvature (as found in independent parallel work in Refs. [35, 36]).

In this chapter, we address these questions by studying the magnetic field response of the current in metals in different situations. We start in Sec. 2.2 by using a model Hamiltonian to demonstrate that an adiabatically increasing magnetic field can generate a charge current along the direction of the magnetic field even without any topological properties such as Weyl nodes in the dispersion. This establishes that not only is a CME-like current response possible, it is not unique to topological systems. In Sec. 2.3 we carefully re-examine the linear response properties and distinguish two kinds of linear response namely - thermal equilibrium

response and dynamical response in the DC limit. In Sec. 2.3.1, we review how the equilibrium linear response must identically vanish. Furthermore, we show that for finite wave-vector magnetic fields in periodic boundary condition systems the DC limit of the dynamical response coincides with the equilibrium response and therefore also vanishes. In Sec. 2.3.2 we explain the apparent discrepancy between linear response and existing field-theory calculations, we also provide an explicit expression for finite frequency CME in Weyl semimetals and show that it has a universal nonzero limit at $\omega >> \mathbf{q}$. In Sec. 2.3.3, we resolve the apparent discrepancy between the results of Sec. 2.2, which show a finite CME-like response, the linear response calculations in this section that prove vanishing CME. We find here, that the open boundaries in Sec. 2.2 lead to the DC limit of the dynamical response being different from the vanishing equilibrium response and remaining finite. Finally in Sec. 2.4, we show that while disorder might be used to make the notion of a perturbative magnetic field better defined, it still leads to a vanishing CME response due to scattering.

2.2 Chiral magnetic response of conventional systems at finiite B field

In this section we present an example of a system which develops a DC current in response to the application of a DC magnetic field $\mathbf{B}$ that is parallel to the direction of the current. Therefore, in a sense we will see that the key surprising aspect of the chiral magnetic response i.e. a current response to a magnetic field is not only

possible, but is not unique to non-topological systems.

The model we study is described by the Hamiltonian

$$\hat{H}(\mathbf{k}) = \mathbf{k}^4 + \alpha k_F k_z^3 - k_F^4 \tag{2.1}$$

which is parametrized by k_F and α. In the isotropic limit $\alpha \to 0$, k_F describes the Fermi wave-vector of the system. The parameter α is key to breaking time-reversal and inversion symmetries along the z-direction, which are symmetries that would forbid a current response. We will choose this parameter to be small i.e. $\alpha \ll 1$, so that the modification of the dispersion around the Fermi surface can be computed perturbatively in α.

Applying a constant magnetic field along the z axis in Landau gauge changes $\hat{H}$ to

$$\begin{aligned} &\hat{H}(k_x - eBy, -i\partial_y, k_z) = \\ &[(k_x - eBy)^2 - \partial_y^2 + k_z^2]^2 + \alpha \mathbf{k}_F k_z^3 - \mathbf{k}_F^4. \end{aligned} \tag{2.2}$$

This has the same eigenstates as a two-dimensional electron gas in a magnetic field, these eigenstates are well known [1].The spectrum for states in the bulk are given by

$$E(B, n, k_z) = \left[\omega_c \left(n + \frac{1}{2}\right) + k_z^2\right]^2 + \alpha \mathbf{k}_F k_z^3 - \mathbf{k}_F^4 \tag{2.3}$$

where $\omega_c = eB$ is the cyclotron frequency. Since the vector potential $A_x(y) = By$ is not periodic in the y-drection, we will consider the system to to be open along the y direction with width W and have periodic boundary conditions along the x and z direction. For this system the bulk extends for a range of $|k_x| < W/2eB$, beyond

which the bulk states merge into chiral edge states. Assuming that the system to be terminated in the y-drection by a potential $V(y)$, which varies smoothly on the scale of the magnetic length, the dispersion including both bulk and edge states is given by

$$E(B, n, k_x, k_z) = [\omega_c(n + \frac{1}{2}) + k_z^2]^2 + \alpha \mathbf{k}_F k_z^3 - \mathbf{k}_F^4 + V\left(\frac{k_x}{eB}\right). \tag{2.4}$$

The mean current carried by the system along the z-direction in steady state can be written as

$$\langle \mathbf{j}_z \rangle = -e \sum_{n,k_x} \int_{BZ} \frac{dk_z}{2\pi} \frac{\partial E(B, n, k_x, k_z)}{\partial k_z} f_n(k_x, k_z), \tag{2.5}$$

where $\frac{\partial E(B,n,k_x,k_z)}{\partial k_z}$ is the group velocity of the electrons along the z-direction and $f_n(k_x, k_z)$ is the occupation of the electronic states in the nth Landau level at wave-vector k_x, k_z. For simplicity, we consider a system starting at a finite uniform magnetic field $B = B_1$. At such a finite magnetic field B, the Landau levels indexed by n at any given momentum point (k_x, k_z) are separated in energy and adiabatically increasing the magnetic field B from $B = B_1$ to $B = B_2$ preserves the initially equilibrium occupation of the electronic levels which is given by

$$f_n(k_x, k_z) = n_F(E(B_1, n, k_x, k_z)), \tag{2.6}$$

where $n_F(E)$ is the Fermi function at some temperature T.

It should be noted that as the magnetic field is raised, the distribution no longer remains an equilibrium distribution. In fact, the current can be shown to vanish in equilibrium, in complete agreement with Refs . [25, 34] since

$$\langle \mathbf{j}_z \rangle = -e \sum_{n,k_x} \int_{BZ} \frac{dk_z}{2\pi} \frac{\partial \tilde{n_F}(E(B, n, k_x, k_z))}{\partial k_z}. \tag{2.7}$$

where $\tilde{n}_F(x) = \int_{-\infty}^{x} dx' n_F(x')$ is the integrated Fermi function. Noting that this function must approach a constant at the edge of the BZ where $n_F = 0$, the current density then vanishes as $\langle \mathbf{j}_z \rangle = -e \sum_{n,k_x} [\tilde{n_F}(E \to \infty) - \tilde{n_F}(E \to \infty)] = 0$.

On the other hand, in the limit of a small but finite change in the magnetic field, the current density aquires a finite expectation value that can be expanded to lowest order in $(B_2 - B_1)$ as

$$\langle \mathbf{j}_z \rangle = -e(B_2 - B_1) \sum_{n,k_x} \int_{BZ} \frac{dk_z}{2\pi} \frac{\partial^2 E(B, n, k_x, k_z)}{\partial B \partial k_z}|_{B=B_1}$$

$$n_F(E(B_1, n, k_x, k_z)). \tag{2.8}$$

Assuming the zero-temperature limit, the above integral can be restricted to be between $k_z = k_{z,1}$ and $k_z = k_{z,2}$, which are the unperturbed Fermi points defined by $E(B, n, k_x, k_z) = 0$. With this simplification, the current density is written as

$$\langle \mathbf{j}_z \rangle = -\frac{e}{2\pi} \sum_{n,k_x} (B_2 - B_1)$$

$$[\partial_B E(B, n, k_x, k_{z2}) - \partial_B E(B, n, k_x, k_{z1})]|_{B=B_1}. \tag{2.9}$$

Substituting in E from equation (2.4) gives

$$\langle \mathbf{j}_z \rangle = -\frac{e^2}{\pi} \sum_{n,k_x} \left(n + \frac{1}{2}\right) (B_2 - B_1)(k_{z2}^2 - k_{z1}^2) \tag{2.10}$$

Using k_{z1},k_{z2} to first order in α, we obtain

$$\langle \mathbf{j}_z \rangle = \frac{e^2}{\pi} \alpha k_F (B_2 - B_1)$$

$$\sum_{n,k_x} \frac{(n + \frac{1}{2}) \left[\left(k_F^4 - V(\frac{k_x}{eB})\right)^{1/2} - eB_1(n + \frac{1}{2}) \right]^{3/2}}{\left(k_F^4 - V(\frac{k_x}{eB})\right)^{1/2}} \tag{2.11}$$

which is nonzero in general even though the original Hamiltonian has no Berry curvature.

2.3 Linear response in the clean systems

2.3.1 Vanishing of low-frequency linear response for periodic boundary conditions

In apparent contradiction to the previous section, the dynamical linear response of the current to a low-frequency magnetic field has been shown to vanish [25]. To facilitate a direct comparison with our example, we review the argument in some detail. The key ingredient in this argument is to consider the response function in thermal equilibrium referred to as the equilibrium response, which is distinct from the DC limit of the dynamical response in general. The DC limit of the dynamical response is the real-frequency response with the frequency being finite but small.

The response of the current operator $\mathbf{j}(\mathbf{r})$ in thermal equilibrium to linear order in an external magnetic field is given by

$$\langle \hat{j}_a(\mathbf{r}) \rangle = \frac{Tr[\hat{j}_a(r) e^{-\beta(\hat{H}_0 + \int d\mathbf{r}' \mathbf{j}(r').\mathbf{A}(r'))}]}{Tr[e^{-\beta(\hat{H}_0 + \int d\mathbf{r}' \mathbf{j}(r').\mathbf{A}(r'))}]} + \langle \frac{\delta \hat{j}_a(\mathbf{r})}{\delta B} \rangle_0 \tag{2.12}$$

where the second term accounts for the intrinsic change of the current operator $\mathbf{j}$ due to the application of the magnetic field. Here $\mathbf{A}(\mathbf{r})$ is the vector potential generated by the magnetic field and $\beta = 1/k_B T$ is the inverse temperature. Defining

$$\hat{u}(\beta) = e^{-\beta(\hat{H}_0 + \int d\mathbf{r}' \mathbf{j}(r').\mathbf{A}(r'))} e^{\beta \hat{H}_0} = \tag{2.13}$$
$$1 + \int dr' \int_0^\beta d\tau e^{-\tau \hat{H}_0} \mathbf{j}(r').\mathbf{A}(r') e^{\tau \hat{H}_0} + O(A^2)$$

and using it to expand equation (3.6) first order gives

$$\begin{aligned}\langle\hat{j}_a(\mathbf{r})\rangle &= \langle\hat{j}_a(\mathbf{r})\rangle_0 + \langle\frac{\delta\hat{j}_a(\mathbf{r})}{\delta B}\rangle_0 \\ &+ \frac{Tr[\int dr' \int_0^\beta d\tau \hat{j}_a(r) e^{-\tau\hat{H}_0}\mathbf{j}(r').\mathbf{A}(r')e^{(\tau-\beta)\hat{H}_0}]}{Tr[e^{-\beta\hat{H}_0}]} \\ &- \langle\hat{j}_a(\mathbf{r})\rangle_0 \frac{Tr[\int dr' \int_0^\beta d\tau e^{-\tau\hat{H}_0}\mathbf{j}(r').\mathbf{A}(r')e^{(\tau-\beta)\hat{H}_0}]}{Tr[e^{-\beta\hat{H}_0}]}\end{aligned} \tag{2.14}$$

The first and the fourth terms evaluate to zero since $\langle\hat{j}_a(\mathbf{r})\rangle_0 = 0$. For a translationally invariant system, we can write

$$\begin{aligned}\langle\hat{j}_a(\mathbf{r})\rangle &= \frac{Tr[\Big(\int dr' \int_0^\beta d\tau \hat{j}_a(r) e^{-\tau\hat{H}_0}\hat{j}_b(r')e^{(\tau-\beta)\hat{H}_0}\Big)]}{Tr[e^{-\beta\hat{H}_0}]}\mathbf{A}_b(r') \\ &+ \langle\frac{\delta\hat{j}_a(\mathbf{r})}{\delta B}\rangle_0 = \int d\mathbf{r}'\Pi_{ab}(\mathbf{r}-\mathbf{r}')A_b(\mathbf{r}') + \langle\frac{\delta\hat{j}_a(\mathbf{r})}{\delta B}\rangle_0\end{aligned} \tag{2.15}$$

Translational invariance suggests that the transformation to the Fourier domain would simplify the results. However, it turns out that periodic boundary conditions restrict us from using a strictly uniform magnetic field, and we must consider a magnetic field with a finite but small wave-vector $\mathbf{q}$. At such a wave-vector we can readily choose the Fourier transform of the vector potential $\mathbf{A}(r)$ to be $\mathbf{A}(\mathbf{q}) = \frac{i}{q^2}\mathbf{B}\times\mathbf{q}$. Using this, we can obtain the response of the lowest Fourier components of the current density as

$$\begin{aligned}\langle\hat{j}_a(\mathbf{q})\rangle =& \frac{Tr[\Big(\int_0^\beta d\tau \hat{j}_a(\mathbf{q}) e^{-\tau\hat{H}_0}\hat{j}_b(-\mathbf{q})e^{(\tau-\beta)\hat{H}_0}\Big)]}{Tr[e^{-\beta\hat{H}_0}]}\mathbf{A}_b(\mathbf{q}) \\ =& \sum_b \Pi_{ab}(\mathbf{q})\mathbf{A}_b(\mathbf{q}) + \langle\frac{\delta\hat{j}_a(\mathbf{q})}{\delta B}\rangle_0\end{aligned} \tag{2.16}$$

The second term vanishes in many of our examples and will be assumed to be zero for simplicity in the remainder of this section. By relating the vector potential to

the magnetic field, we can rewrite equation (2.16) as

$$\langle \hat{j}_c(\mathbf{q})\rangle = \Big(\epsilon_{abc}\frac{1}{2iq}(\Pi^R_{ab})^{ant}\Big)\mathbf{B}_c \equiv \sigma_{ch}\mathbf{B}_c. \tag{2.17}$$

Where $(\Pi^R_{ab})^{ant}$ is the anti symmetric part of Π_{ab}. Expanding the current operator in terms of the creation operators $\hat{c}^\dagger_{n,\mathbf{k}}$ for eigenstates $|m,\mathbf{k}\rangle$ of the Bloch Hamiltonian with eigenvalues $\varepsilon_{n,\mathbf{k}}$ as

$$\hat{j}_a(\mathbf{q}) = \sum_{n,m,\mathbf{k}} \langle n,\mathbf{k}-\frac{\mathbf{q}}{2}|\hat{J}_a(\mathbf{k})|m,\mathbf{k}+\frac{\mathbf{q}}{2}\rangle \hat{c}^\dagger_{n,\mathbf{k}-\frac{\mathbf{q}}{2}}\hat{c}_{m,\mathbf{k}+\frac{\mathbf{q}}{2}} \tag{2.18}$$

where $\hat{J}_a(\mathbf{k})$ are the single-particle current operators that are derived from the Bloch Hamiltonian. The response function Π_{ab} in Eq. 2.16 can be expanded in the single-particle energy basis to look like,

$$\begin{aligned}\Pi^{ant}_{ab}(\mathbf{q}) &= \frac{Tr\left[\Big(\int_0^\beta d\tau \hat{j}_a(\mathbf{q})e^{-\tau\hat{H}_0}\hat{j}_b(-\mathbf{q})e^{(\tau-\beta)\hat{H}_0}\Big)\right]}{Tr[e^{-\beta\hat{H}_0}]} \\ &= e^2\sum_{n,m,k}\Big[\frac{\int_0^\beta d\tau e^{-\tau\varepsilon_{m,k+\frac{q}{2}}}e^{(\tau-\beta)\varepsilon_{n,k-\frac{q}{2}}}}{Tr[e^{-\beta\hat{H}_0}]}\Big] \\ &\times \langle n,\mathbf{k}-\frac{\mathbf{q}}{2}|\hat{J}_a(\mathbf{k})|m,\mathbf{k}+\frac{\mathbf{q}}{2}\rangle\langle m,\mathbf{k}+\frac{\mathbf{q}}{2}|\hat{J}_b(\mathbf{k})|n,\mathbf{k}-\frac{\mathbf{q}}{2}\rangle;\end{aligned} \tag{2.19}$$

performing the τ integral turns this expression to the form

$$\begin{aligned}\Pi^{ant}_{ab}(\mathbf{q}) &= e^2\sum_{n,m,k}\frac{n_F(\varepsilon_{n,\mathbf{k}-\frac{\mathbf{q}}{2}}) - n_F(\varepsilon_{m,\mathbf{k}+\frac{\mathbf{q}}{2}})}{\varepsilon_{n,\mathbf{k}-\frac{\mathbf{q}}{2}} - \varepsilon_{m,\mathbf{k}+\frac{\mathbf{q}}{2}}} \\ &\times\langle n,\mathbf{k}-\frac{\mathbf{q}}{2}|\hat{J}_a(\mathbf{k})|m,\mathbf{k}+\frac{\mathbf{q}}{2}\rangle\langle m,\mathbf{k}+\frac{\mathbf{q}}{2}|\hat{J}_b(\mathbf{k})|n,\mathbf{k}-\frac{\mathbf{q}}{2}\rangle.\end{aligned} \tag{2.20}$$

This expression is identical to the result obtained for the dynamical linear response formalism in the limit $\omega \to 0$ or more precisely $\omega \ll q$.

Following the arguments of Refs. [25, 34] it is easy to show that the result of equation (3.6) and subsequently equation (2.20) has to vanish as $\omega \to 0$ i.e. as the

magnetic field is varied slowly compared to $\mathbf{q}$. Therefore, we conclude that

$$\Pi_{ab}^{ant}(\omega \ll q \to 0) = 0. \tag{2.21}$$

This result is in agreement with Ref [28] but in contrast to findings of Ref [26]. It should be noted that this result does not prohibit the usual diamagnetic response since it only restricts the anti-symmetric part of Π_{ab}, whereas the diamagnetic response is related to the diagonal part of the polarization tensor.

We remark that the validity Equation.(2.21) assumes the ability to analytically continue the CME response to real frequency from an imaginary formalism in the limit $\omega \to 0$. This is guaranteed only if the perturbative response has a finite DC ($\omega \ll q \to 0$) limit. This can break down, for example, in cases with a vanishing group velocity $\mathbf{v}_{n,k}$ in a band, in this case intra-band terms become divergent, and as a result, the vanishing of the CME would not be guaranteed.

2.3.2 Comparison with field theory results for Weyl semimetals

One of the questions raised by the previous subsection is how to reconcile field theory predictions of a nonzero chiral magnetic response with our vanishing results. To investigate this we explicitly calculate equation (2.20) for a generic two-band model and use the result to calculate σ_{ch} defined in equation (2.17) (details of this calculation are presented in the appendix).The final expression is given by

$$\sigma_{ch} = e\sum_{n=\pm}\int_{BZ}\frac{d\mathbf{k}}{(2\pi)^3}\nabla_{\mathbf{k}}\mathbf{m}_n(\mathbf{k})f(\varepsilon_n(\mathbf{k}),t) \tag{2.22}$$

$$+e^2\sum_{n=\pm}\int_{BZ}\frac{d\mathbf{k}}{(2\pi)^3}(\frac{\mathbf{v}_{-,\mathbf{k}}+\mathbf{v}_{+,\mathbf{k}}}{2}).\mathbf{\Omega}_{n,\mathbf{k}}f(\varepsilon_n(\mathbf{k}),t),$$

where

$$\mathbf{m}_n(\mathbf{k}) = -i\frac{e}{2}(\nabla_{\mathbf{k}}\langle n,\mathbf{k}|)\times[\hat{H}(\mathbf{k})-\varepsilon_n(\mathbf{k})](\nabla_{\mathbf{k}}|n,\mathbf{k}\rangle) \tag{2.23}$$

and

$$\mathbf{\Omega}_{n,\mathbf{k}} = i(\nabla_{\mathbf{k}}\langle n,\mathbf{k}|)\times(\nabla_{\mathbf{k}}|n,\mathbf{k}\rangle) \tag{2.24}$$

is the wave-packet orbital magnetization. Our result for σ_{ch} is in agreement with Ref. [28] but different from Refs. [26]. Using the periodicity of the lattice, the second term in equation (2.22) can be partially integrated to look like the first term with the opposite sign, therefore giving a vanishing σ_{ch} as expected. However, if we work within a low-energy effective hamiltonian description of the problem, as is usually done in field theory calculations , a non-vanishing result might have been achieved.To illustrate this point consider the simplest low energy effective Hamiltonian of a Weyl semimetal, that is two linearly dispersing well fermions (i.e. $H^{eff} = \pm v_F\sigma.\mathbf{k}$), in this case at each $\mathbf{k}$ is momentum space $\mathbf{v}_{+,\mathbf{k}} = -\mathbf{v}_{+,\mathbf{k}} = v_F\hat{k}$ and therefore the second term in equation (2.22) identically vanishes and we are left with

$$\sigma_{ch}^{eff} = e\sum_{n=\pm}\int_{BZ}\frac{d\mathbf{k}}{(2\pi)^3}\nabla_{\mathbf{k}}\mathbf{m}_n(\mathbf{k})f(\varepsilon_n(\mathbf{k}),t), \tag{2.25}$$

Partial integrating equation (2.25) in zero temperature gives

$$\sigma_{ch}^{eff} = e\int_{FS}\frac{d\mathbf{a}.\mathbf{m}_+(\mathbf{k})}{(2\pi)^3} \tag{2.26}$$

where + here corresponds to the conduction band. For a general two-band Bloch Hamiltonian $H(\mathbf{k}) = e(\mathbf{k}) + \mathbf{r}(\mathbf{k}) \cdot \sigma$ (where $\sigma_{x,y,z}$ are the Pauli matrices), the energy eigenvalues are given by

$$\varepsilon_{\pm} = e(\mathbf{k}) \pm |\mathbf{r}(\mathbf{k})| \tag{2.27}$$

Substituting the eigenvalues and eigenvectors into Eq. 2.23, the orbital magnetic moment is written as:

$$\mathbf{m}_{\pm}(\mathbf{k}) = \pm e|\mathbf{r}(\mathbf{k})|\mathbf{\Omega}(\pm, \mathbf{k}) \tag{2.28}$$

where $\mathbf{\Omega}(\pm, \mathbf{k})$ is the Berry curvature. Using this we can rewrite equation (2.26) as

$$\begin{aligned} \sigma_{ch}^{eff} =& e^2 \int_{FS} |\mathbf{r}(\mathbf{k})| \frac{d\mathbf{a} \cdot \mathbf{\Omega}(+, \mathbf{k})}{(2\pi)^3} \\ =& e^2 \int_{FS} (\varepsilon_F - e(\mathbf{k})) \frac{d\mathbf{a} \cdot \mathbf{\Omega}(+, \mathbf{k})}{(2\pi)^3} \\ =& - e^2 \int_{FS} e(\mathbf{k}) \frac{d\mathbf{a} \cdot \mathbf{\Omega}(+, \mathbf{k})}{(2\pi)^3}, \end{aligned} \tag{2.29}$$

where we used the fact that the total Chern number of the entire Fermi surface is zero to get from the first line to the second line. In the case of a two-node Weyl semimetal, we have two Fermi surfaces with $e_2 - e_1 = \delta k_0$ and opposite values of uniform Berry curvature $\mathbf{\Omega}(+, \mathbf{k})$; therefore, $\sigma_{ch}^{eff} = (\frac{e}{2\pi})^2 \delta k_0$ as expected from field theory [32, 37]. This argument can be easily generalized to include an arbitrary number of Weyl nodes. Note that even though we recovered the quantum field theory result, it is not applicable to a real material since it doesn't include the second term in equation (2.22). This term in a periodic system forces the chiral response $\sigma_{ch} = 0$.

As has been pointed out, this situation can be partially circumvented by the

chiral magnetic response at non-zero frequencies, where $\omega \gtrsim q$. While this limit can produce non-vanishing results even in lattice systems, it is difficult to disentangle the contribution of the electric field generated by the time-dependence of the magnetic field in this limit. The finite frequency generalization of the linear response calculation is given by [1]

$$\Pi_{ab}(\mathbf{q},\omega) = e^2 \sum_{n,m,k} \frac{f(\varepsilon_{n,\mathbf{k}-\frac{\mathbf{q}}{2}}) - f(\varepsilon_{m,\mathbf{k}+\frac{\mathbf{q}}{2}})}{\omega + \varepsilon_{n,\mathbf{k}-\frac{\mathbf{q}}{2}} - \varepsilon_{m,\mathbf{k}+\frac{\mathbf{q}}{2}}} \tag{2.30}$$
$$\times \langle n, \mathbf{k} - \frac{\mathbf{q}}{2} | \hat{J}_a(\mathbf{k}) | m, \mathbf{k} + \frac{\mathbf{q}}{2} \rangle \langle m, \mathbf{k} + \frac{\mathbf{q}}{2} | \hat{J}_b(\mathbf{k}) | n, \mathbf{k} - \frac{\mathbf{q}}{2} \rangle.$$

To investigate behavior of σ_{ch} as a function of frequency, we will numerically calculate equation (2.30) for a simple two-band model of Weyl semimetal with two Weyl nodes at zero temperature. In this calculation, the vanishing of the $\omega \ll q \to 0$ response comes to our aid, and we can use this fact to argue that the inter-band terms must cancel in the $\omega \to 0$ limit of the intra-band (i.e. Fermi surface) terms. Therefore, the finite-frequency response only Fermi surface properties contribute to equation (2.30) and therefore no further knowledge of the microscopic details of the Hamiltonian is necessary. Focusing on the intraband contribution to Eq. 2.30, we obtain

$$\Pi_{ab}^{intra}(\mathbf{q},\omega) = e^2 \sum_{n,k} \frac{\theta(\varepsilon_{n,\mathbf{k}-\frac{\mathbf{q}}{2}}) - \theta(\varepsilon_{n,\mathbf{k}+\frac{\mathbf{q}}{2}})}{\omega + \varepsilon_{n,\mathbf{k}-\frac{\mathbf{q}}{2}} - \varepsilon_{n,\mathbf{k}+\frac{\mathbf{q}}{2}}} \tag{2.31}$$
$$\times \langle n, \mathbf{k} - \frac{\mathbf{q}}{2} | \hat{J}_a(\mathbf{k}) | n, \mathbf{k} + \frac{\mathbf{q}}{2} \rangle \langle n, \mathbf{k} + \frac{\mathbf{q}}{2} | \hat{J}_b(\mathbf{k}) | n, \mathbf{k} - \frac{\mathbf{q}}{2} \rangle.$$

The results of this calculation are plotted in figure 2.1. It starts from zero at $\omega \ll q$ as expected from equilibrium theory, then peaks at some frequency and then approaches $\sigma_{ch} = \frac{2}{3}\sigma_{ch}^{eff}$ at $\omega \gg q$, however, that since $\mathbf{E} \propto \omega \mathbf{A}$ and $\mathbf{B} \propto q\mathbf{A}$ in

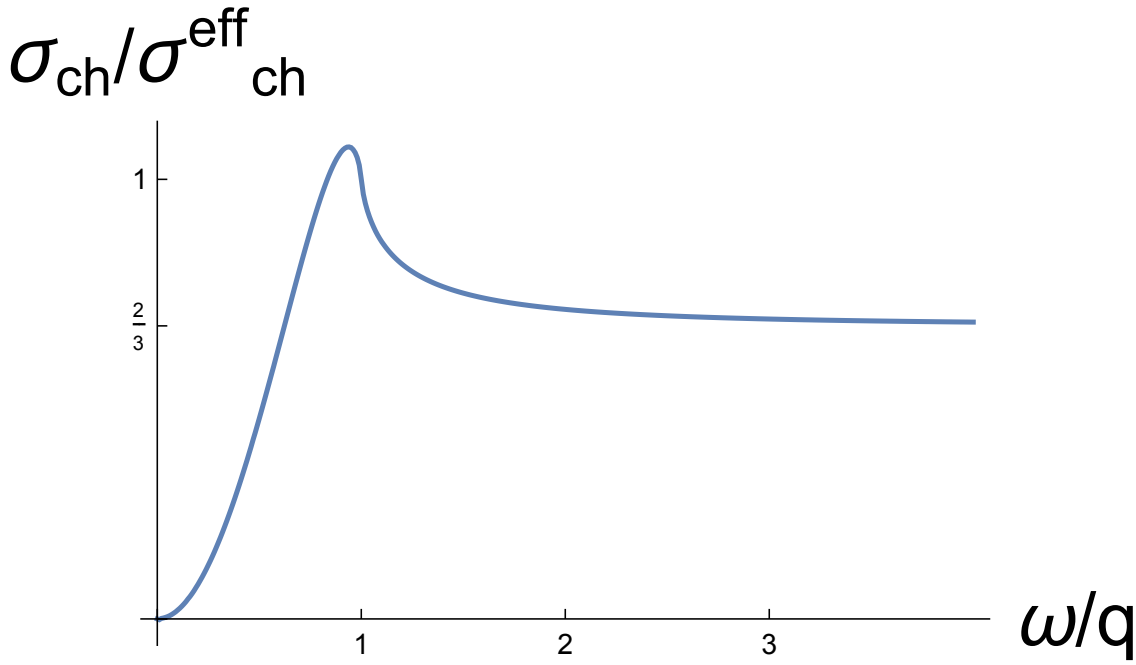

Figure 2.1: Frequency dependence of the Chiral Magnetic response $\sigma_{ch}(q,\omega)$ in a bulk Weyl semimetal in a two-band, two-nodes model. It vanishes in the DC (i.e. $\omega \to 0$) limit as expected from the equilibrium theory. We chose the parameter $q = 0.0001$

this limit $E \gg B$, and therefore nonzero σ_{ch} in this limit is more of an electric field effect rather than magnetic field one. It is worth mentioning that in the limiting case of $\omega = q \ll 1$, we get $\sigma_{ch} = \sigma_{ch}^{eff}$. We believe this feature is coincidental, since this limit does not correspond to $B \neq 0$ and $E = 0$ as required in the DC chiral magnetic effect.

Also note that the topology of a Weyl semimetal is not necessary to obtain a nonzero σ_{ch} [35, 36, 38]. One way to see this is to look at the limit $\omega \gg q$. Direct

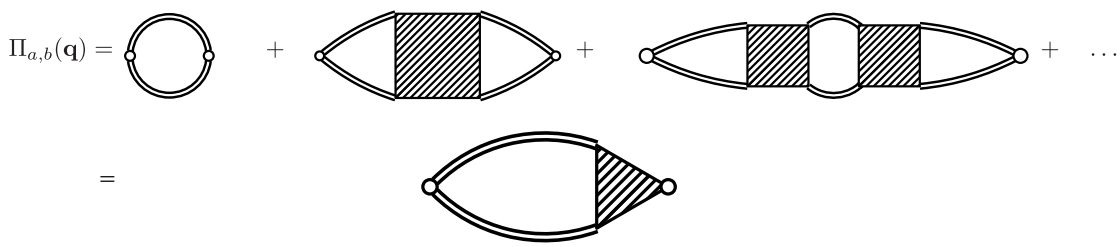

Figure 2.2: Feynman diagrams contributing to the correlator $\Pi_{a,b}$. Double lines correspond to $G(\widetilde{\mathbf{k}})$ (i.e. dressed propagator) and the shaded boxes correspond to two-particle irreducible diagrams [1]

calculation of equation (2.30) for an isotropic model in this limit gives

$$\sigma_{ch} = \frac{2}{3}\sigma_{ch}^{eff} = \frac{2}{3}e\sum_{n=\pm}\int_{BZ}\frac{d\mathbf{k}}{(2\pi)^3}\nabla_{\mathbf{k}}.\mathbf{m}_n(\mathbf{k})f(\varepsilon_n(\mathbf{k}),t); \tag{2.32}$$

all the steps from equation (2.25) to equation (2.29) go through here as well. Interestingly $e(\mathbf{k})$ and $\mathbf{\Omega}(\pm,\mathbf{k})$ in Eq.(2.29) are independent of each other since the Berry curvature only depends on eigenstates not eigenvalues. Therefore, as long as Berry curvature is not zero everywhere on Fermi surface, we can choose $e(\mathbf{k})$ arbitrarily such that σ_{ch} is non zero. Therefore, similar to the magneto-electric effect [39], topology, which is defined by Fermi surface components with non-vanishing Berry flux [21], is not necessary to a get nonzero σ_{ch}. Similar finite-frequency CME resulting from non-topological Berry curvature has been previously reported [35, 36, 38].

2.3.3 B-field response under open boundary conditions

The second issue raised by the vanishing DC limit of the dynamical response, which has not been resolved earlier, is the apparent contradiction between equation (2.21) and the example presented in Sec. 2.2. As we will show, the crux of this discrepancy

lies in the fundamental difference in the description of the magnetic field for systems with open and periodic boundary conditions.

Unlike in the case of periodic boundary conditions, where a magnetic field must be applied with a finite wave-vector $\mathbf{q}$, open systems can be subject to a strictly uniform magnetic field as in experiments. A uniform magnetic field $\mathbf{B}$ in an open system can be represented in the circular gauge by a vector potential $\mathbf{A}$ that is given by $\boldsymbol{A} = \frac{1}{2}\mathbf{B} \times \mathbf{r}$. In this case, the magnetic field perturbation δB affects the Hamiltonian as $H \to H - \mathbf{M}_z \delta B$, where $\hat{M}_b = \frac{1}{2}\int d\mathbf{r}(\mathbf{J}(\mathbf{r}) \times \mathbf{r})_b$ is the magnetic moment operator. Using this insight from Sec. 2.3.1 and noting that $\int d\mathbf{r}'\mathbf{J}(\mathbf{r}')\cdot\mathbf{A}(\mathbf{r}')$ transforms to $M_z B$ in the present notation, the response of the equilibrium current density to magnetic field is

$$\delta\langle j\rangle = \int d\tau \frac{Tr[je^{-(\beta-\tau)H_0}M_z e^{-\tau H_0}]}{Tr[e^{-\beta H_0}]}, \tag{2.33}$$

where $j \equiv j_z$ is the current operator in the z direction. Note that the $\mathbf{j}.\mathbf{A}$ term could have been written as $\mathbf{M}_z\delta B$ in the previous section as well. However, we find that the latter form is suited better for dealing with open boundary conditions, where the wave vector $\mathbf{q}$ is no longer a good quantum number, whereas for periodic boundaries using the former expression makes it easy to relate $\sigma_c h$ to the usual form of the current current correlation in Equation(2.37) . Expanding in the quasiparticle-operator eigenbasis $H_0 = \sum_p \epsilon_p c_p^\dagger c_p$ and the other operators as $j = \sum_{p,q} J_{p,q} c_p^\dagger c_q$ and $M = \sum_{r,s} m_{r,s} c_r^\dagger c_s$, the current response matrix element becomes

$$\delta\langle j\rangle = \sum_{p,q,r,s} J_{pq} m_{rs} \int d\tau \frac{Tr[c_p^\dagger c_q e^{-(\beta-\tau)H_0} c_r^\dagger c_s e^{-\tau H_0}]}{Tr[e^{-\beta H_0}]}. \tag{2.34}$$

Noting that $e^{\tau H_0} c_r^\dagger e^{-\tau H_0} = c_r^\dagger e^{-\epsilon_r \tau}$

$$\delta\langle j\rangle = \sum_{p,q,r,s} J_{pq} m_{rs} \frac{Tr[c_p^\dagger c_q e^{-\beta H_0} c_r^\dagger c_s]}{Tr[e^{-\beta H_0}]} \int_0^\beta d\tau e^{-\tau(\epsilon_r - \epsilon_s)}. \tag{2.35}$$

Separating the $r \neq s$ and $r = s$ contributions to the current response, $\delta\langle j\rangle = \delta\langle j\rangle_{r\neq s} + \delta\langle j\rangle_{r=s}$, the $r \neq s$ contribution is written as

$$\delta\langle j\rangle_{r\neq s} = e^2 \sum_{r\neq s} \frac{f(\varepsilon_r) - f(\varepsilon_s)}{\varepsilon_r - \varepsilon_s} \times \langle r|\hat{J}_z|s\rangle\langle s|\hat{M}_z|r\rangle. \tag{2.36}$$

This term is equivalent to the DC limit of the finite-frequency linear response. To compare this result to the dynamical linear response in Eq. 2.20, we notice that $k_{x,y}$ are no longer good quantum numbers in the open boundary condition case, and we can simply replace $\mathbf{k} \to k_z$ in the derivation in Sec. 2.3.1. Therefore, the open system limit is obtained from Eq. 2.20 by dropping the $\mathbf{k}, \mathbf{q}$ labels and is written as

$$\Pi_z = e^2 \sum_{n,m} \frac{f(\varepsilon_n) - f(\varepsilon_m)}{\varepsilon_n - \varepsilon_m - \omega} \times \langle n|\hat{J}_z|m\rangle\langle m|\hat{M}_z|n\rangle. \tag{2.37}$$

Now note that at any finite $\omega > 0$, the $m = n$ contribution to the above sum vanishes, so that the DC (i.e. $\omega \to 0$) limit of this expression is identical to that in Eq. 2.36.

In addition to the DC limit of the dynamic response, there is also a contribution to the equilibrium current response $\delta\langle j\rangle$, which is written as

$$\delta\langle j\rangle_{r=s} = \beta \sum_{p,r} J_{pp} m_{rr} [f(\epsilon_r) f(\epsilon_p)(1 - \delta_{pr}) + \delta_{rp} f(\epsilon_r)], \tag{2.38}$$

where we note that the $p = r$ and $p \neq r$ cases lead to different terms in the above expression and $f(\epsilon_p) = \langle c_p^\dagger c_p\rangle$ are Fermi functions. In contrast, the analogue of the $r = s$ term does not contribute to the finite-frequency response function. Finally,

we note that the explicit response of the current $\langle \frac{\delta j}{\delta B} \rangle$ is identical in both real and imaginary frequency cases. We have ignored this contribution for simplicity.

The $r = s$ term in Eq. 2.38 can lead to a substantial difference between the vanishing equilibrium response and the DC limit of the dynamical response. As a result, while the equilibrium linear response is required to vanish based on the argument in Sec. 2.3.1, the DC limit (i.e. $\omega \to 0$) of the dynamic response is not necessarily vanishing as suggested by Sec. 2.2. This is consistent with the non-vanishing CME obtained for certain open systems [40].

2.4 Chiral magnetic response in weakly disordered systems

The necessity of a finite but small wave-vector $\mathbf{q}$ for the magnetic field used in the linear-response derivation in Sec. 2.3.1 leads to some subtle difficulties in the order of limits. This is because that the vector potential scales as $A \approx \frac{B}{q}$, and therefore it diverges as $\mathbf{q} \to 0$, so that as $q \to 0$, the range of B over which the perturbation theory is valid shrinks to zero. This difficulty can be avoided by introducing another length scale into the problem so that the response function becomes independent of q at small enough q. One way to do this is to introduce the length $\frac{1}{\tau}$ given by the inverse of the scattering rate; in this case the wave vector q just needs to be much smaller than the mean free path $q \ll \frac{1}{\tau}$ rather than going to zero $q \to 0$. To address this problem we will consider the problem of static CME in a disordered metal in the last section.There we'll show that equation (2.21) remains valid in the presence of weak disorder.

As mentioned in the introduction, disorder introduces a length scale $\frac{1}{q}$ into the the system , that can help make the perturbation theory valid when the magnetic field is turned on. We introduce disorder into a lattice realization of a Weyl semi-metal through a potential term in the Hamiltonian, which is written as:

$$V = \sum_{\mathbf{r},a} u_a(\mathbf{r}) c_a(\mathbf{r})^\dagger c_a(\mathbf{r}) \tag{2.39}$$

where $\mathbf{r}$ labels unit cells and a labels atoms inside the unit cell. For our calculations, we use a Gaussian white-noise disorder model for the functions $u_a(\mathbf{r})$ with a correlation function $\langle u_a(\mathbf{r}) u_b(\mathbf{r}')\rangle = \nu_D \delta_{a,b} \delta_{\mathbf{r}-\mathbf{r}'}$, where ν_D characterizes the strength of the disorder. The potential perturbation V in Fourier space is written as

$$V = \sum_{\mathbf{k},\mathbf{q},a} u_a(\mathbf{q}) c_a(\mathbf{k}+\mathbf{q})^\dagger c_a(\mathbf{k}) \tag{2.40}$$

where $\langle u_a(\mathbf{q}) u_b^*(\mathbf{q}')\rangle = \nu_D \delta_{a,b} \delta_{\mathbf{q}-\mathbf{q}'}$. Starting with this perturbation, the disorder averaged Green function can be calculated within the Born approximation [1] as $G(\widetilde{\mathbf{k}})^{-1} = \omega - \hat{H}(\mathbf{k}) - \Sigma(\omega)$ where

$$\Sigma_{ab}(\omega) = \nu_D \delta_{ab} \int d\mathbf{q} d\omega G^{(0)}_{aa}(\mathbf{q}, \omega) \tag{2.41}$$

is the electron self-energy within the Born approximation and $G^{(0)}$ is the bare time-ordered Green function (i.e. $G^{(0)}(\mathbf{q}, \omega) = [\omega + i\text{sign}(\omega)\eta - H(\mathbf{k})]^{-1}$). Note that for compactness we have introduced the notation $\widetilde{k} := (\mathbf{k}, \omega)$.

To calculate the disorder averaged response σ_{ch}, we use the Kubo formula as in the clean case modified to include weak disorder. Following the standard diagrammatic theory for disorder [1], we do this by calculating the Feynman diagrams shown in Fig [2.2]. In these diagrams, the double lines correspond to disorder -averaged

Green functions $G(\widetilde{\mathbf{k}})$, and the shaded boxed correspond to disorder scattering by the fluctuations in the potential V. We can sum all of the contributing diagrams into a renormalized current vertex, Γ_a (shown in the second line Fig [2.2]), so that the response function is written as:

$$\Pi_{a,b}(\mathbf{q},\omega) = e^2 Tr\big[\int_{-\infty}^{\infty}\frac{d\omega}{2\pi}\int_{BZ}\frac{d^3k}{(2\pi)^3}\hat{J}_a(\mathbf{k}) \times G(\widetilde{\mathbf{k}}+\frac{\widetilde{\mathbf{q}}}{2})\mathbf{\Gamma}_b(\widetilde{\mathbf{k}}+\frac{\widetilde{\mathbf{q}}}{2},\widetilde{\mathbf{k}}-\frac{\widetilde{\mathbf{q}}}{2})G(\widetilde{\mathbf{k}}-\frac{\widetilde{\mathbf{q}}}{2})\big] \tag{2.42}$$

where

$$\mathbf{\Gamma}_b(\widetilde{\mathbf{k}}+\frac{\widetilde{\mathbf{q}}}{2},\widetilde{\mathbf{k}}-\frac{\widetilde{\mathbf{q}}}{2}) = \hat{J}_b(\mathbf{k}) + \nu_D\int\frac{d\widetilde{\mathbf{q}}'}{2\pi} \times G(\widetilde{\mathbf{k}}+\frac{\widetilde{\mathbf{q}}}{2}+\widetilde{q}')\mathbf{\Gamma}_b(\widetilde{\mathbf{k}}+\frac{\widetilde{\mathbf{q}}}{2}+\widetilde{q}',\widetilde{\mathbf{k}}-\frac{\widetilde{\mathbf{q}}}{2}-\widetilde{q}')G(\widetilde{\mathbf{k}}-\frac{\widetilde{\mathbf{q}}}{2}-\widetilde{q}') \tag{2.43}$$

We note that the validity of this approach requires being in the diffusive limit (i.e. mean-free path $\gg$ Fermi wave-length). We will avoid this regime by choosing a finite chemical potential with a Fermi energy much greater than the disorder scattering rate.

In principle, once Π is calculated using Eq. 2.42, one can substitute it back into Eq. 2.17 to calculate the chiral magnetic response σ_{ch}. We now argue that this necessarily vanishes for a disordered system. To do this, note that the Ward identity [41] gives:

$$\omega\Gamma_0(\widetilde{\mathbf{k}}+\frac{\widetilde{\mathbf{q}}}{2},\widetilde{\mathbf{k}}-\frac{\widetilde{\mathbf{q}}}{2}) - \mathbf{q}.\mathbf{\Gamma}(\widetilde{\mathbf{k}}+\frac{\widetilde{\mathbf{q}}}{2},\widetilde{\mathbf{k}}-\frac{\widetilde{\mathbf{q}}}{2}) = -G^{-1}(\widetilde{\mathbf{k}}+\frac{\widetilde{\mathbf{q}}}{2}) + G^{-1}(\widetilde{\mathbf{k}}-\frac{\widetilde{\mathbf{q}}}{2}), \tag{2.44}$$

which in turn guarantees that in the limit, $\frac{\omega}{q}\to 0$ that we are interested in:

$$\mathbf{\Gamma}_a(\widetilde{\mathbf{k}}+\frac{\widetilde{\mathbf{q}}}{2},\widetilde{\mathbf{k}}-\frac{\widetilde{\mathbf{q}}}{2}) = \partial_{k_a}G^{-1}(\widetilde{\mathbf{k}}) = \partial_{k_a}\hat{H}(\mathbf{k}) = \hat{J}_a(\mathbf{k}). \tag{2.45}$$

This implies that there are no vertex corrections, and we need to consider only the bubble diagram (the first diagram in the first line of Fig. 2.2). With this approximation, Π in Eq. 2.42 when expanded to first order in q becomes:

$$\Pi_{a,b}(\mathbf{q},\omega) = e^2 \frac{q}{6} \sum_{a,b,c} \varepsilon_{a,b,c} Tr\big[\int_{-\infty}^{\infty} \frac{d\omega}{2\pi} \int_{BZ} \frac{d^3k}{(2\pi)^3} \times \partial_{k_a} G^{-1}(\widetilde{\mathbf{k}}) \partial_{k_c} G(\widetilde{\mathbf{k}}) \partial_{k_b} G^{-1}(\widetilde{\mathbf{k}}) G(\widetilde{\mathbf{k}}) \big] \tag{2.46}$$

This has the form of a Hopf topological invariant [42] and vanishes since the Green function G has no real frequency poles (shown in the appendix). Therefore, using Eq. 2.17, we conclude that $\sigma_{ch} = 0$ universally for all disordered physical systems. This is consistent with the equilibrium results showing that the current must vanish in a magnetic field in a lattice system [25, 34].

On the other hand, for frequencies much larger than the scattering rate $\omega >> \frac{1}{\tau}$, we expect disorder not to play a role, and therefore finite-frequency chiral magnetic response σ_{ch} should return to the clean-limit value in such a range. In this case, we have to be careful to ensure that the wave-vector $\mathbf{q}$ is chosen to obey the limit $\omega/q \to 0$.

To understand how σ_{ch} crosses over from the vanishing DC value to the clean-limit value, we numerically calculate $\Pi_{y,z}(q\hat{x},\omega)$ for the model Hamiltonian of Weyl semimetal used in Ref. [26] :

$$\hat{H} = \sum_{\mathbf{k}} \Psi^{\dagger}_{\mathbf{k}} [N_{0,\mathbf{k}} \sigma_0 + \mathbf{N}_{\mathbf{k}}.\sigma] \Psi_{\mathbf{k}} \tag{2.47}$$

$$N_{0,\mathbf{k}} = 8t \prod_i \cos(k_i)$$

$$N_{j,\mathbf{k}} = \sin(k_j)$$

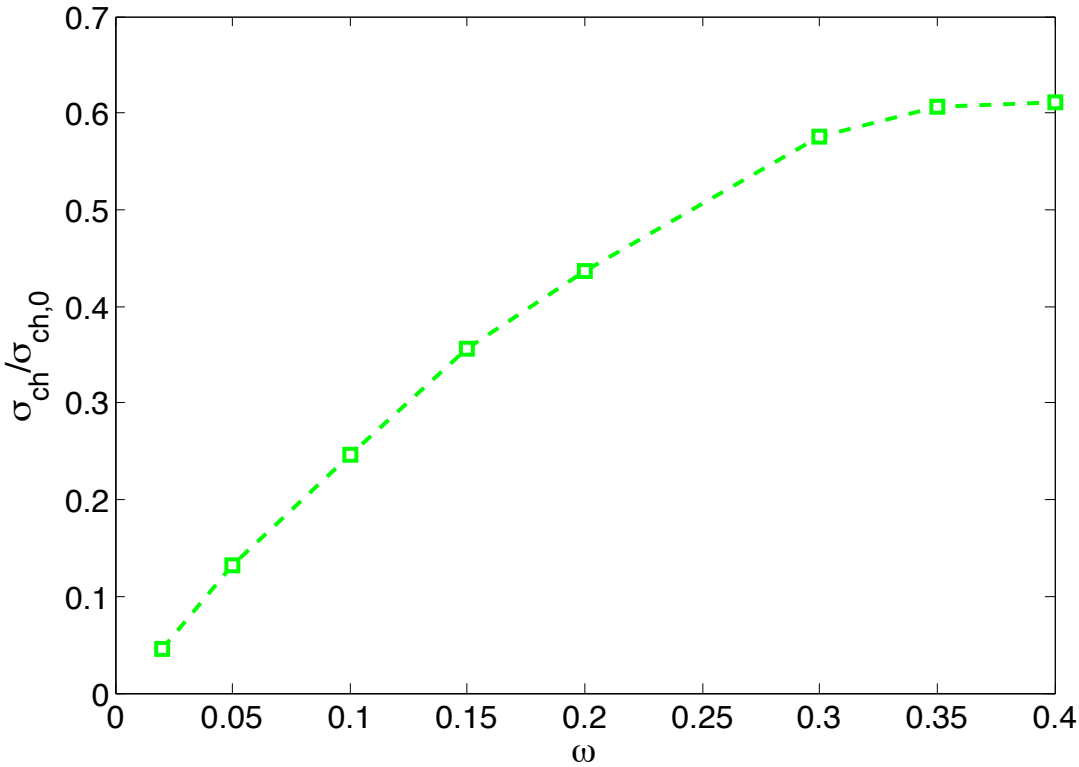

Figure 2.3: Frequency dependence of the Chiral Magnetic response $\sigma_{ch}(q,\omega)$ in a bulk Weyl semimetal. While σ_{ch} reaches a value close to the clean limit of $\approx 0.6\sigma_{ch,0} = 0.6t(e/2\pi)^2$ for frequencies exceeding the disorder scattering rate $\frac{1}{\tau} = 0.05 \propto \nu_D$, it vanishes in the DC (i.e. $\omega \to 0$) limit, as expected from the equilibrium theory. For the calculation, we chose the parameter $t = 0.15$ and the wave-vector $q = 0.4$

This model hosts four right handed Weyl Fermions located at high symmetry points $(0,0,0),(\pi,\pi,0),(\pi,0,\pi),(0,\pi,\pi)$ and four left handed ones at $(\pi,\pi,\pi),(0,0,\pi),(0,\pi,0),(\pi,0,0)$. We use the same disorder realization as in equation (2.39) and use Eq. 2.42 to calculate $\Pi_{y,z}(q\hat{x},\omega)$ so that we can calculate σ_{ch} using Eq. (2.45) (without taking the limits $\omega, q \to 0$). To reduce the numerical complexity, we assume that ω/q is still small enough so that we can use Eq. (2.45). Within this approximation, we then replace the self-energy by a uniform scattering rate $\Sigma(\omega) \approx i\tau^{-1} = i0.05$. The resulting $\sigma_{ch}(\omega)$ from our calculation, which is plotted in Fig. 2.3, shows that σ_{ch} vanishes in the DC limit and approaches $\approx 0.6\sigma_{ch,0} = 0.6t(e/2\pi)^2$, which is consistent with the clean limit for the chosen $q = 0.4$.

2.5 Conclusion

In summary, we have shown that a CME-like response, i.e. one where a current flows in response to a magnetic field, is in principle possible with or without Weyl nodes. This appears to contradict previous claims of the vanishing of the low frequency CME. We point out that the derivation of the vanishing CME is a consequence of periodic boundary conditions of the system. A more realistic system with open boundary conditions would not be subject to the same constraints and can have a non-vanishing CME. We also studied the finite-frequency CME with periodic boundary conditions and consistent with recent work, we found it to be non-vanishing in general when there was a non-vanishing Berry curvature on the Fermi surface. This

does not necessitate having a topological Berry flux as in the case of a Weyl node. Finally, we studied how the perturbation theory in magnetic field might be more stable in the presence of disorder. Using the standard diagrammatic treatment of disorder within the Born approximation, we have found that in a realistic disordered system, the chiral magnetic response is really a dynamical phenomenon and vanishes in the DC limit. For frequencies in excess of the scattering rate, the clean-limit predictions are recovered. Numerical evaluation of the associated integrals for a specific lattice model show how the cross-over occurs as the frequency is increased above the scattering rate.

Chapter 3: $\mathbb{Z}_3$ parafermionic zero modes without Andreev backscattering from the 2/3 fractional quantum Hall state

3.1 Introduction.

Theoretical understanding and experimental realization of non-Abelian anyons has attracted considerable attention in the past few decades. In addition to being of fundamental interest as a dramatic manifestation of a topological phase, non-Abelian anyons also have potential applications as building blocks for topological quantum computers [4]. Majorana zero modes (MZMs) [43–48] provide the simplest and experimentally the most promising example of non-Abelian anyons. So far, most of the effort in searching for non-Abelian anyons has focused on MZMs. Following a series of theoretical proposals [49–52], suggestive experimental evidence of MZMs has been observed in semiconductor/superconductor heterostructures [53–59]. Despite their fascinating properties, MZMs are non-Abelian anyons of the Ising ($\mathbb{Z}_2$) type. Universal quantum computation cannot be implemented using braiding of $\mathbb{Z}_2$ anyons alone. Therefore, searching for a computationally richer set of anyons is called for.

Parafermionic zero modes (PZMs) [60–62] (also known as fractional Majorana modes) provide an example of such computationally rich (still not universal) anyons.

They can be thought of as $\mathbb{Z}_n$ generalizations of MZMs. Similar to MZMs, $\mathbb{Z}_n$ PZMs are associated with n-fold degeneracy of the ground state that is robust to all local perturbations. Due to fundamental restrictions set on possible topological phases in strictly one-dimensional systems [63, 64], PZMs cannot exist in isolation in one dimension. However, recently it was realized that boundaries of two-dimensional systems can circumvent these restrictions. It was explicitly shown that PZMs emerge at the one-dimensional boundary of two counter-propagating fractional quantum Hall (FQH) edges coupled with superconducting contacts [65–68]. These setups greatly resemble one canonical proposal used to realize MZMs [69], with the role of topological insulator played by a pair of opposite-chirality FQH states. All of existing proposals (involving superconductors) require two main ingredients; induced superconductivity via coupling FQH edge state to a superconductor and crossed Andreev tunneling between two edges. The first requirement has already been achieved in experiments [70–72]. However, the second requirement is likely to be difficult to achieve experimentally due to disruption of FQHE states placed adjacent to a superconductor. This is because strong coupling to the superconductor is likely to change density in the surrounding 2D electron gas, pushing the FQHE away from the superconductor. The amplitude of quasiparticle tunneling between edges would then be reduced by the increased distance and the Fermi wave-vector in the intervening superconducting region. Experimental evidence [72] also seems to suggest that observable crossed Andreev tunneling amplitude is much too weak to generate a coherent gap. In addition, disorder in the superconductor would likely randomize the superconducting backscattering, which is likely to destabilize the topological

phase as in the case of Majorana modes [73].

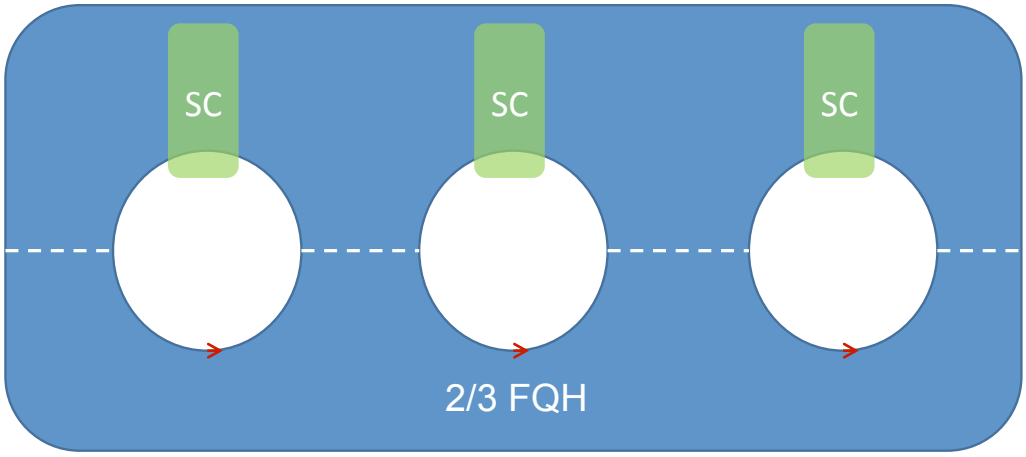

Figure 3.1: Top view of the system, comprised of a linear array of superconductors coupled to loops of FQH edge states. Different loops are connected via quasiparticle hopping.

In this chapter we propose a practical scheme to realize $\mathbb{Z}_3$ PZMs from the spin-unpolarized 2/3 fractional quantum Hall state using superconducting contacts without cross-Andreev tunneling, which can be realized in present experiments. Our system is comprised of a linear array of FQH edge loops; each one of these loops is coupled to a superconductor through proximity effect, and separate loops are connected via quasiparticle tunneling. Superconductors are separated from FQH bulk using a barrier. Different superconductors are connected using thin wires to ensure they have the same superconducting phase. The strength of quasiparticle tunneling can be controlled with a gate voltage. A top view of this setup is shown in Fig. 3.1. We use a combination of analytical and numerical methods to study this model and show that for realistic values of parameters, at relatively small chain

lengths (order ten loops) this system can be tuned to a topological phase hosting $\mathbb{Z}_3$ PZMs.

3.2 Model.

-We begin by studying a single loop coupled to a superconductor. Assuming $SU(2)$ symmetry, the effective Hamiltonian describing the charge part of the $\nu = 2/3$ FQH edge state is given by the following chiral boson theory [74, 75],

$$H_{edge} = \int_0^L dx \left[\frac{u}{4\pi\nu} (\partial_x \varphi(x))^2 - \frac{u m_\mu}{2L} \partial_x \varphi(x) \right] \tag{3.1}$$

where L is the length of the loop, u is the mode velocity, m_μ is the gate controlled dimensionless chemical potential (as opposed to actual chemical potential $\mu = \frac{u m_\mu}{2L}$) and $\varphi(x)$ is the chiral boson field that is defined in terms of the charge density operator as $\rho = \frac{1}{2\pi} \partial_x \varphi(x)$. The $\varphi(x)$ field obeys the usual commutation relation $[\varphi(x), \partial_y \varphi(y)] = 2i\pi\nu\delta(x-y)$ [74,75]. Using this relation we can write the charge 2/3 spinless quasiparticle creation operator as $e^{i\varphi(x)}$ and charge 2 Cooper pair creation operator as $e^{3i\varphi(x)}$. In Eq.(3.1), we have not in included the neutral mode, which does not couple to the SC and is expected to be non-degenerate and gapped, will be ignored in the rest of this work. Charge 1/3 excitations that involve the neutral mode are also gapped out. The edge Hamiltonian H_{edge} can be diagonalized [76] by mode expanding $\varphi(x)$ as

$$\begin{aligned} \varphi(x) = \frac{2\pi \hat{n} \nu x}{L} + \hat{\varphi}_0 + \\ \sum_{k=0}^{K_{max}} \left[-i\sqrt{\frac{\nu}{k}} a_k^\dagger e^{2\pi i k x/L} + i\sqrt{\frac{\nu}{k}} a_k e^{-2\pi i k x/L} \right] \end{aligned} \tag{3.2}$$

where $a_k, a_k^\dagger$ are the kth momentum boson creation and annihilation operator for $k \in \mathbb{N}$, $\hat{\varphi}_0$ and $\hat{n}$ are the zero mode phase and number operators, respectively, and K_{max} is the momentum cutoff.

Now we can rewrite Eq.(3.1) as,

$$H_{edge} = \frac{u\pi\nu}{L}\big(\hat{n}^2 - m_\mu \hat{n} + \frac{2}{\nu}\hat{P}\big) + const \tag{3.3}$$

where $\hat{P} = \sum_{k=0}^{K_{max}} k\hat{a}_k^\dagger \hat{a}_k$ is the total momentum operator. When the dimensionless chemical potential m_μ is tuned by gate voltage to integer values, the spectrum is invariant under changing $n = m$ to $n = -m + m_\mu$. For odd m_μ this translates into a two-fold ground state degeneracy. This degeneracy survives the addition of superconductivity and will play a crucial role later on.

The effect of a superconductor on a single loop can be modeled by the Hamiltonian

$$H_{sc} = \int_0^L dx \frac{\Delta(x)}{L} e^{-\frac{2\pi i x m_\mu}{L}} e^{3i\varphi(x)} + h.c \tag{3.4}$$

describing the tunneling of Cooper pairs to and from the superconductor. Here $\Delta(x)$ corresponds to the position-dependent Cooper-pair tunneling amplitude, and $e^{-\frac{2\pi i x m_\mu}{L}}$ is the phase factor taking into account the chemical potential mismatch between the FQH edge and the (grounded) superconductor. Fourier transforming $\Delta(x) = \sum_k \Delta(k) e^{\frac{2\pi i k x}{L}}$ and mode expanding $\varphi(x)$ (as in Eq. (3.2)) allows us to write the only nonzero matrix elements of H_{sc}:

$$\langle n_0 \pm 3, \{m_k\}|H_{sc}|n_0, \{n_k\}\rangle = \sum_k \Delta(k)\delta_{(\Delta E \pm 3k),0} \tag{3.5}$$

$$\times \langle n_0 \pm 3, \{m_k\}|e^{\pm 3i\varphi(0)}|n_0, \{n_k\}\rangle,$$

where $\Delta E = E(n_0 \pm 3, \{m_k\}) - E(n_0, \{n_k\})$ is the energy difference between the initial and the final state, and $E = \frac{u\pi\nu}{L}(n^2 - m_\mu n + 3P)$ is the bare edge energy of each state in accordance with Eq. (3.3). Equation (3.5) implies that the special case of uniform superconductivity $\Delta(x) = \Delta_0$ leads to the additional conserved quantity H_{edge}, because $[H_{sc}, H_{edge}] = 0$. Though convenient, this symmetry is not generic and is therefore not used in this chapter.

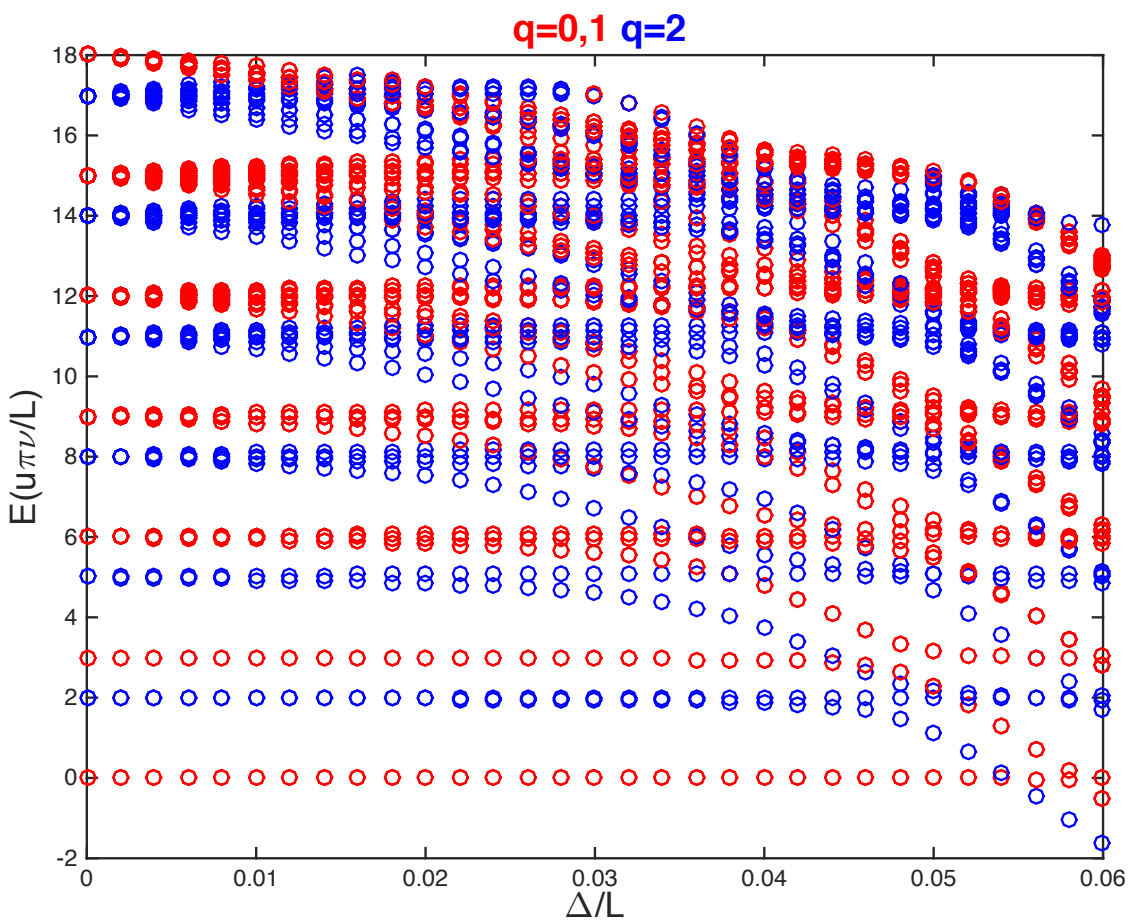

Figure 3.2: Low-lying spectrum for "pseudo-point-like" superconductivity as a function of $\frac{\Delta}{L}$. Here $m_\mu = 1$, $K_{max} = 4$ and q is the fractional charge modulo three, $q = \mathrm{mod}(n, 3)$. All red circles are two-fold degenerate; blue circles are non-degenerate.

The inclusion of H_{sc} reduces the conservation of fractional charge n to conservation of $q = \mathrm{mod}(n, 3)$, which only takes three values $q = 0, 1, 2$. Using this restriction we can divide the system into three independent charge sectors with $q = 0, 1, 2$. For integer m_μ, the $n = 3m$ to $n = -3m + m_\mu$ symmetry of the non-superconducting edge now translates into degeneracy of two of the charge sectors, for example at $m_\mu = 1$ the two sectors $q = 0, 1$ will become degenerate.

Using Eq.(3.5) we can numerically calculate the spectrum of a single loop $H = H_{edge} + H_{sc}$. We set $m_\mu = 1$ and assume a "pseudo-point-like" superconductivity such that $\Delta(k) = \Delta$ for $|k| \leqslant K$, where, for simplicity, we have chosen $K = K_{max}$ i.e. the momentum cutoff defined in Eq.(3.2) (note that K and K_{max} did not have to be equal). The low-lying part of the spectrum is plotted in Fig. 3.2. This plot shows that the ground state is separated from the rest of the spectrum by a gap for a finite range of Δ. However, the ground state degeneracy (between $q = 0, 1$) remains two-fold with $q = 2$ split.

3.3 Effective Hamiltonian.

-In the absence of superconductivity and for odd values of the dimensionless chemical potential ($m_\mu = 2n-1$), the ground-state energy of the system is twofold degenerate and is separated from the excited states by a gap for a range of Δ. The two ground states can be labeled by fractional charge $q = 0, 1$. Therefore, as long as we choose Δ in this range and restrict the ratio of hopping amplitude to the energy gap $t/\Delta E$ to be small, we can apply a Schrieffer-Wolff transformation to obtain an

effective Hamiltonian defined in the Hilbert space spanned by ground states of single loops [77]. This emergent Hilbert space has only two states per site ($q = 0, 1$) and therefore can be thought of as a chain of spin 1/2 particles, where the states with spin up/down correspond to the single loop ground states with $q = 1, 0$.

To calculate the low-energy effective Hamiltonian, we start with the Hamiltonian describing quasiparticle hopping between different loops,

$$H_{tunnel} = t \sum_i e^{i\varphi_i(L/2)} e^{-i\varphi_{i+1}(0)} + H.c. \tag{3.6}$$

Note that $e^{i\varphi_i(x)}$ is an anyonic operator and has nontrivial commutation relation with other anyonic operators. For different sites we can write,

$$e^{i\varphi_j(x)} e^{i\varphi_k(x')} = e^{i\varphi_k(x')} e^{i\varphi_j(x)} e^{i\pi\nu \mathrm{sgn}(k-j)}. \tag{3.7}$$

Using a generalized Jordan-Wigner string we can define the new field variables $\tilde{\varphi}(x)$,

$$e^{i\varphi_j(x)} = e^{i\pi\nu(\sum_{k<j} \tilde{n}_k)} e^{i\tilde{\varphi}_j(x)}. \tag{3.8}$$

The advantage of these new field variables is that they commute trivially between different sites $[e^{i\tilde{\varphi}_i(x)}, e^{i\tilde{\varphi}_j(x')}] \propto \delta_{i,j}$, and therefore act strictly on the local loop Hilbert space. Now we can rewrite H_{tunnel} as,

$$H_{tunnel} = t \sum_i e^{i\tilde{\varphi}_i(L/2)} e^{-i\pi\nu\tilde{n}_{0,i}} e^{-i\tilde{\varphi}_{i+1}(0)} + H.c.. \tag{3.9}$$

To second order in perturbation theory we can write the low-energy effective Hamiltonian as

$$\begin{aligned} H_{eff} =& P H_{tunnel} P - P H_{tunnel} \frac{(1-P)}{H_0} H_{tunnel} P \\ &+ O(t^3/\Delta E^2), \end{aligned} \tag{3.10}$$

where P is the single-loop ground-state projection operator defined as $P = \sum_i (|q = i\rangle\langle q = i|)$, and H_0 is the shifted single-loop Hamiltonian (shifting to set ground state energy to zero).

Putting everything together we get (Details of this calculation can be found in the Appendix, here we just quote the final results),

$$\begin{aligned} H_{eff} = \sum_i \Big[& (t\alpha_0 e^{i\pi/3} - t^2\alpha_1 e^{-2i\pi/3})\sigma_i^+\sigma_{i+1}^- \\ & - t^2 e^{2i\pi/3}\gamma\sigma_{i-1}^+\sigma_{i+1}^- - t^2\beta\sigma_i^z\sigma_{i+1}^z \\ & + t^2\lambda\sigma_{i-1}^+\sigma_i^+\sigma_{i+1}^+\Big] + H.c. + O(t^3/\Delta E^2) \end{aligned} \tag{3.11}$$

where σ's are the usual Pauli matrices and $\alpha, \beta, \gamma, \lambda$ are parameters calculated in the Appendix. Note that all terms in the Hamiltonian conserve fractional charge (spin) modulo three and are also $\mathbb{Z}_2$ symmetric under $\sigma^z \to -\sigma^z$. This $\mathbb{Z}_2$ symmetry can be associated with the $\varphi \to -\varphi + \frac{2\pi m_\mu \nu x}{L}$ symmetry of the original Hamiltonian (that we have already discussed). Note that presence of the term $t^2\lambda\sigma_{i-1}^+\sigma_i^+\sigma_{i+1}^+$ requires nonzero superconductivity, since without Δ, fractional charge (spin) has to be conserved. As seen in Fig. 3.3, this term, which arises at second order in tunneling, requires H_{sc} so that q=3 may be converted to q=0 by the removal of a Cooper pair.

Chain length	Ground state energy	1st excited state energy	2nd excited state energy	3rd excited state energy
10	-6.818	-6.696	-6.696	-6.149
40	-29.681	-29.677	-29.677	-29.384
100	-75.524	-75.524	-75.524	-75.267

Table 3.1: Numerical DMRG calculation results for "pseudo point-like" superconductivity(defined earlier) at $t = 1$, $\Delta/L = 0.046$ and momentum cutoff $K_{max} = 4$

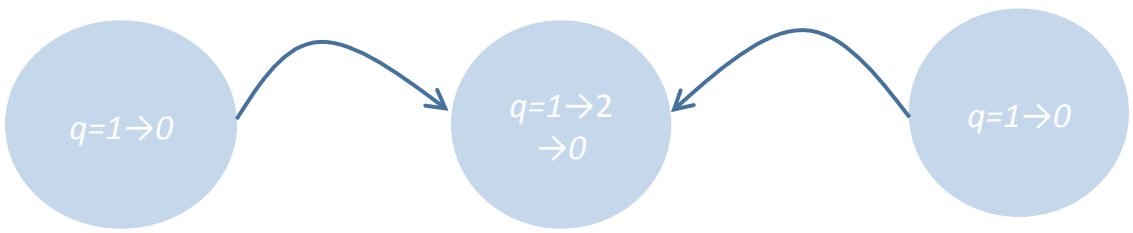

Figure 3.3: $\sigma^-_{i-1}\sigma^-_i\sigma^-_{i+1}$ term as a second-order process in perturbation theory. q is the fractional charge modulo three. Two fractional charges are tunneled to the middle site, one from each neighbor

3.4 Analysis.

-In the absence of the superconductivity (σ_z non-conserving terms), the conservation of σ_z ensures a gapless state with low-energy Luttinger liquid Hamiltonian where $\sigma_z \sim \nabla\phi$. In this Luttinger liquid description, the superconducting term $t^2\lambda\sigma^+_{i-1}\sigma^+_i\sigma^+_{i+1}$ is represented as $g\cos(3\theta)$, which converts the Luttinger liquid to a Sine-Gordon model. For the correct choice of parameters the superconductivity in-

duced term $g\cos(3\theta)$ becomes perturbatively relevant [78] and gaps out the system into a topological phase with a $\mathbb{Z}_3$ parafermionic degeneracy, where each ground state corresponds to the phase θ being locked at one of the three minima of the $\cos(3\theta)$ term [65–68]. To check whether this degeneracy occurs in our system (i.e., the Hamiltonian in Eq. (3.11)) with realistic values of the parameters, we numerically study the Hamiltonian in Eq.(3.11) using the DMRG method [78]. DMRG calculations were performed using the ITensor C++ library [79]. Sample results of this calculation are shown in Table. 3.1. These results confirm the existence of a three-fold degeneracy for reasonable parameters. The degeneracy is weakly split for small chain lengths $N \approx 10$ and is more pronounced at longer lengths, as expected from a true topological degeneracy [80]. These results are expected to be insensitive to temperature since the energy gap is of order of $u\pi\nu/L$, which for loop lengths of order of several quasiparticle radii (Each quasiparticle radius is of order of several magnetic lengths) would be of the order of the FQH gap, which is much larger than the temperature at which the FQH state is observed.

We have repeated this calculation with $K_{max} = 3, 4, 5$ (larger values are numerically hard to simulate) and found that the results are qualitatively insensitive to the exact value of K_{max}. Moreover, for a realistic system K_{max} can be approximated as inverse of loop length in units of quasiparticle radius, which assuming loops lengths of order of several quasiparticle radiuses, makes are our calculation to fall within the correct physical regime.

In a realistic setting the value of m_μ cannot be set exactly to an odd integer value. The effect of this imperfect tuning is described by $h\sum_i \sigma_i^z$, where h is the

energy offset between the two states caused by the chemical potential shift. In the Luttinger liquid description, this term can be represented by adding a $\nabla\phi$ term to the the Sine-Gordon model. Phase diagram of such a Sine-Gordon model in an external field is well studied [78] , basically showing that the gapped phase persists as long as h is smaller than the energy gap calculated without the chemical potential offset (in our case previously calculated using DMRG method).

For experimental purposes, it's also important to discuss the role of disorder. We emphasize that in principle all topological phases of matter are robust to local perturbations that are small compared to the system gap size. However, to be concrete we consider the effect of random fluctuations in loop lengths; this effect is likely to be significant in a real experiment. We have performed numerical calculations on this system (with details in the Appendix), and found that our results are robust to significant fluctuations in loops lengths at least of order of $\frac{\Delta L}{L} \approx 0.3$.

An alternative interesting limit is that of "true" point-like superconducting contacts, that is $\Delta(k) = \Delta\ \forall k$. This limit is particularly appealing, as in this case analytical results may be obtained for large values of Δ. Following the formalism developed in Ref. [81], we show (with details in the Appendix) that in the large Δ limit the system is described by a set of decoupled harmonic oscillators, and that in this limit all three fractional charge sectors become degenerate. Analogous to the previous case (small Δ), as long as $t/\Delta E$ is small, we can use Schrieffer-Wolff transformation to find an effective Hamiltonian. The effective Hilbert space of each site is three-dimensional (corresponding to three fractional charge sectors) and can be thought of as a three state clock model, or equivalently, a 3-state Potts model.

In this limit, it's useful to define,

$$\alpha_{2j-1} = \frac{e^{-i\varphi_j(0)}}{A(0)}; \alpha_{2j} = \frac{e^{-i\varphi_j(L/2)}}{A(L/2)} \tag{3.12}$$

where $A(x) = (\prod_i \langle q = i|e^{-i\varphi(x)}|q = i+1\rangle)^{1/3}$ is a normalization factor. Within the effective Hilbert space, these operators are the usual parafermionic operators, that is $\alpha_j^3 = 1$ and $\alpha_j\alpha_{j'} = \alpha_{j'}\alpha_j e^{i\frac{2\pi}{3}sgn(j'-j)}$. Using these variables and the Hamiltonians in Eqs.(3.6) and (3.10) we arrive at

$$H_{eff} = t\sum_i (A^*(L/2)A(0)\alpha_{2j}^\dagger\alpha_{2j+1} + H.c.) + O(t^2/\Delta E). \tag{3.13}$$

In this form presence of the parafermionic edge zero modes $(\alpha_1, \alpha_{2N+1})$ is already manifest [61]. Note that in contrast to Eq.(3.11), here the calculation has been done to first order in t. Using the usual clock model variables [82] we can write the Hamiltonian in a more familiar form,

$$H_{eff} = \sum_i (-J\sigma_j^\dagger\sigma_{j+1} + H.c.) + O(t^2/\Delta E) \tag{3.14}$$

where $J = tA^*(L/2)A(0)e^{i\pi/3}$ and

$$\sigma = \begin{pmatrix} 1 & & \\ & \omega & \\ & & \omega^2 \end{pmatrix}, \quad \omega = e^{2\pi i/3} \tag{3.15}$$

is the "clock" operator. In the large but finite Δ regime, the three-fold ground state degeneracy of single loops is not exact. We can take this energy difference into

account by adding a term $h(\tau_j + \tau_j^\dagger)$ to Eq.(3.14), where h is the energy difference of charge sectors $q = 0, 1$ with the charge sector $q = 2$. Estimates for the value of h can be found in the Appendix. Putting everything together we have,

$$H_{eff} = \sum_i (-J\sigma_j^\dagger \sigma_{j+1} + H.c.) + h(\tau_i + \tau_i^\dagger) + O(t^2/\Delta E) \tag{3.16}$$

Note that σ_i is a non-local operator in the physical system of interest. This is an important point as locality prevents the introduction of a Hamiltonian term proportional to σ_i. With this constraint and for small values of h (h can be made arbitrarily small by choosing large enough Δ), the Hamiltonian in Eq.(3.16) is known to be in a topological phase with three-fold degeneracy [60].

We point out that in principle it is possible to extend our proposal (array of quantum dots) to 1/3 bilayer quantum Hall systems without superconductivity, where electron tunneling between quantum dots in different layers replaces the role of superconductivity. In the small-tunneling limit, similar to the superconducting case, the system is effectively described by a pair of "Ising spin chains". To first nonzero order in perturbation theory, the tunneling between the chains is described by $H_t = t\sum_j \prod_i \sigma_{j-1}^i \sigma_j^i \sigma_{j+1}^i + H.c.$, where j, i are the site/layer index. The bosonized form of this system is identical to the previously discussed superconducting system in the small Δ regime plus a decoupled gapless mode [83]. Equivalently in this case when the interlayer tunneling becomes relevant, the system is tuned to a phase with three-fold ground-state degeneracy. This scenario is similar to the idea of topological "genons" [84].

Finally, we remark that the Luttinger liquid description of the quantum Hall

edge might be inaccurate for loops that are only several quasiparticle radiuses in size. However, the effective model in Eq.(3.10) also applies to a chain of superconducting quantum dots in a FQH system that can be gate tuned to have an almost two fold degeneracy between different fractional charges. In this sense, the Luttinger liquid edges might be considered to be a model for quantum dots in an FQH system, and we do not expect the details of the model of the edge to affect our conclusions qualitatively

3.5 Conclusion.

- In this work we have considered a linear array of superconducting "quantum dot"-like holes on a spin singlet 2/3 fractional quantum Hall sample and showed that for both large and small values of induced superconductivity Δ, this system can be tuned to a topological phase hosting $\mathbb{Z}_3$ PZMs. Unlike earlier proposals used to realize PZMs, our approach does not rely on Andreev back-scattering between two fractional quantum Hall edges. In addition, this system appears surprisingly robust to disorder in a way similar to quantum-dot-based proposals for Majorana modes discussed in Refs. [85, 86]. We believe this feature makes our proposal suitable for realization in experiments using ingredients that have already been demonstrated.

Chapter 4: Chiral supercurrent through a quantum Hall weak link

4.1 Introduction

Recently it has been recognized that proximity-induced coupling between an edge state of a quantum Hall (QH) system and a superconductor (SC) provides a rich playground to observe novel and exotic phenomena. In particular, these systems were theoretically demonstrated to support Majorana and parafermionic zero modes [65–68, 87]. Additionally, SC/QH/SC Josephson junctions can allow for a new type of supercurrent carried by the chiral edge states [88–92]. This "chiral" supercurrent is qualitatively distinct from the usual Josephson supercurrent in that it cannot be mediated by a single edge alone, i.e., both right and left moving edges need to be involved. Such chiral supercurrents obey an unusual current-phase relation with the period $2\phi_0 = h/e$, which is twice as large as the period of conventional Josephson junctions [89]. Josephson currents in related systems have also been studied in Refs. [93–98].

Interestingly, in the past few years several different experiments have succeeded in creating a QH/SC interface [71,99–102]. In particular, Amet *et al.* [99] found convincing evidence of chiral supercurrents carried by the quantum Hall edge states. In the semiclassical limit, the chiral supercurrents are propagated by quasiparticles

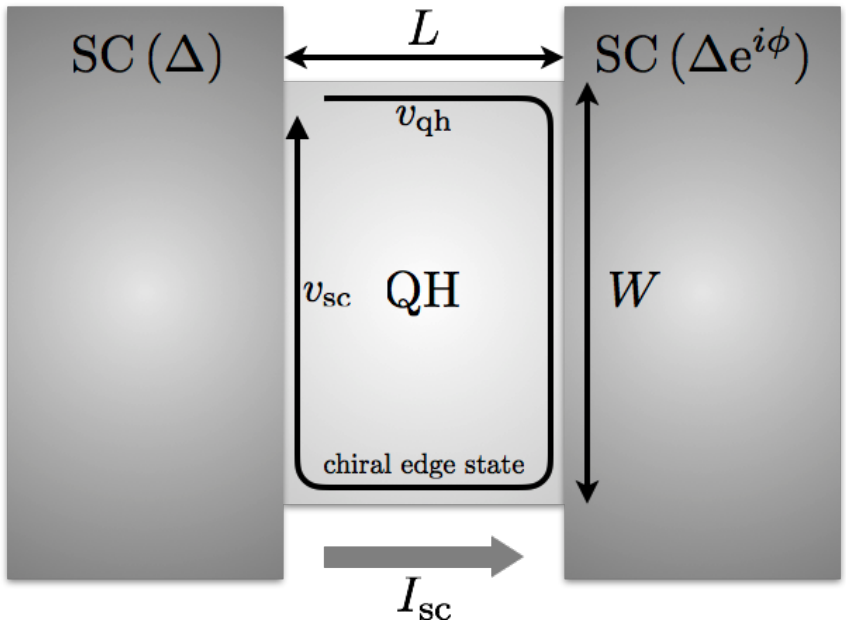

Figure 4.1: Top view of the system, comprised of a quantum Hall weak link attached to a pair of s-wave superconductors with a phase difference ϕ. The edge velocity $v_{\rm qh}$ is renormalized to $v_{\rm sc}$ along the superconducting contacts. $I_{\rm sc}$ is the chiral suppercurrent through the weak link.

bound in skipping orbits that are undergoing Andreev reflection at the SC interface. Such quasiparticles are expected to be slow such that this supercurrent might be too weak to be observed; however, a theoretical understanding of the magnitude of the chiral supercurrent is lacking. Additionally, in apparent contradiction with theory [89, 103, 104] (which suggests anomalous $2\phi_0 = h/e$ periodicity), the experiment observed usual $\phi_0 = h/2e$ periodicity for the current-phase relation, which would arise from tunneling through a conventional (non-chiral) insulator.

In this chapter, we use an effective model to calculate the supercurrent carried by chiral edge states of a spin-degenerate quantum Hall weak link in a geometry

that is similar to the experiments of Ref. [99] (see Fig. 4.1). We find that the obtained supercurrent, calculated for experimentally reasonable parameters, is quantitatively consistent with the measurement in Ref. [99]. In particular, we show that proximity-induced edge velocity renormalization along the SC contacts and surface transparency (which is constrained by normal state conductance) play a crucial role in controlling the magnitude of the supercurrent. We then show that an ideal chiral quantum Hall edge state, even when interactions are included to all orders in perturbation theory, carries only chiral supercurrent, and claim that this can be used as a sharp definition for "chiral" supercurrents. We are unable to explain the $\phi_0 = h/2e$ periodicity observed in the experiment.

4.2 Model

We work within the geometrical setup depicted in Fig. 4.1. We use x as a one-dimensional coordinate for the QH boundary, which is in contact with the SC at $L < x < L + W$ and $2L + W < x < 2(L + W)$. Note that $x = 0$ is identified with $x = 2(L + W)$. Without the SCs, the continuum Hamiltonian describing the spin degenerate chiral quantum Hall edge is given by $H_{\mathrm{QH}} = -i\hbar v_{\mathrm{qh}} \int dx \Psi^\dagger(x)\partial_x \Psi(x)$. Here $\Psi^\dagger(x) = (\psi^\dagger_\downarrow(x),\ \psi_\uparrow(x))$ is a two component spinor, $\psi^\dagger_{\downarrow/\uparrow}(x)$ is the pseudo-spin down/up Fermionic creation operator, and v_{qh} is the QH edge velocity.

We now include the SCs and their couplings with the QH edge to H_{QH}. The full Hamiltonian describing the SC/QH/SC junction is $H_{\mathrm{tot}} = H_{\mathrm{QH}} + H_{\mathrm{SC}} + H_{\mathrm{t}}$. H_{SC} is the BCS mean field Hamiltonian describing the SCs; we assume the SCs to

be s-wave. $H_{\rm t}$ is the Hamiltonian describing normal electron hopping between the SC and the QH edge along the superconducting interface. Note that we have not included the QH bulk states in $H_{\rm tot}$ since they are gapped.

Coupling with the SC induces a gap to the QH boundary spectrum at the interface. In the experimentally relevant limit where the superconducting gap $|\Delta_0|$ is much smaller than the cyclotron frequency $\hbar\omega_c$, this effect can be accounted for by including a self-energy $\Sigma(\omega)$ to the QH edge [105]. Following the results of Ref. [105], we can write the self-energy as:

$$\Sigma(\omega) \approx -\lambda \frac{\omega\tau_0 + \Delta_0\tau_x}{\sqrt{|\Delta_0|^2 - \omega^2}}. \tag{4.1}$$

Here τ is the Pauli matrix in the $\Psi(x)$ spinor space (τ_0 is the 2×2 identity matrix) and λ is a constant characterizing the SC/QH interface which increases as the coupling (hopping) between the SC and QH becomes larger. λ is also related to the broadening of edge state's single particle spectral function caused by the coupling to the SC.

The effective Hamiltonian of the QH edge proximate to the SC ($H^{\rm eff}_{\rm QH/SC}$) can be defined by $(\omega - H_{\rm QH} - \Sigma(\omega))^{-1} = (\omega - H^{\rm eff}_{\rm QH/SC})^{-1}$. In the low-energy limit, $\omega \ll |\Delta_0|$, the self energy (Eq. (4.1)) can be expanded to first order in ω. The effective Hamiltonian then becomes:

$$H^{\rm eff}_{\rm QH/SC} = \int dx \Psi^\dagger(x) \left[\frac{-i\hbar v_{\rm qh}}{1+\lambda/|\Delta_0|}\tau_0\partial_x + \frac{\lambda\Delta_0}{\lambda+|\Delta_0|}\tau_x \right] \Psi(x). \tag{4.2}$$

The first term shows that the edge velocity $v_{\rm qh}$ is strongly renormalized to $v_{\rm sc} = v_{\rm qh}/(1+\lambda/|\Delta_0|)$ in proximity to the SC. Within the semiclassical skipping orbit picture, this velocity renormalization can be attributed to the time delay associated

with Andreev reflection from the SC surface. In each period, a skipping electron spends an additional time of order $\hbar/\Delta_0$ in the SC, which changes the period from $T_{\rm qh} = \pi/\omega_c$ to $T_{\rm sc} \approx \pi(1/\omega_c + \hbar/\Delta_0)$. The finite (imperfect) transparency of the interface, $|t|$, can be considered as the probability of Andreev reflection and can be taken into account by modifying $T_{\rm sc} \approx \pi\,(1/\omega_c + |t|\hbar/\Delta_0)$. This leads to a renormalized edge velocity,

$$v_{\rm sc} = v_{\rm qh}\left[1 + \frac{|t|\hbar\omega_c}{\Delta_0}\right]^{-1}. \tag{4.3}$$

We will use this semiclassical result to estimate the value of λ. Our subsequent calculation shows that the velocity renormalization plays a crucial role in controlling the magnitude of the chiral supercurrent.

The second term of Eq. (4.2) describes the typical proximity-induced superconductivity of a one-dimensional system. Note that the induced superconducting order parameter is also renormalized from its bare value by a factor of $1/(1+|\Delta_0|/\lambda)$. However, $\lambda \gg |\Delta_0|$ in our parameter regime which is relevant to the experiment, and the effect of Δ_0 renomarlization is not significant as that of the velocity.

The final aspect to consider in our model is the phase difference between the two SCs. The superconducting phase difference ϕ shown in Fig. 4.1 can be eliminated by a gauge transformation that introduces a vector potential $a(x)$ given by:

$$a(x) = \begin{cases} -\phi/2L & \text{for } 0 < x < L \\ \phi/2L & \text{for } L+W < x < 2L+W \\ 0 & L \le x \le L+W \end{cases}. \tag{4.4}$$

Combining $H_{\rm QH}$ and $H^{\rm eff}_{\rm QH/SC}$ with the vector potential $a(x)$, we obtain the

effective Hamiltonian describing the entire edge of the QH junction:

$$H = \int dx \Psi^\dagger(x) \Big[\hbar v(x)(-i\tau_0 \partial_x - a(x)\tau_z) + \Delta(x)\tau_x \Big] \Psi(x). \tag{4.5}$$

Here $v(x)$ and $\Delta(x)$ are the position-dependent edge velocity and superconducting order parameter satisfying $v(x) = v_{\rm qh}$ and $\Delta(x) = 0$ for $0 < x < L$ and $L + W < x < 2L + W$; $v(x) = v_{\rm sc}$ and $\Delta(x) = \Delta$ elsewhere, where Δ is the induced superconducting order parameter $\Delta = \frac{\lambda}{\lambda + |\Delta_0|}\Delta_0$.

4.3 Josephson supercurrent

The supercurrent in the SC/QH/SC junction is given by the phase derivative of the free energy: $I_{\rm sc} = -\frac{2e}{\hbar}\frac{\partial F}{\partial \phi}$. By expanding the free energy in imaginary time and accounting for our gauge choice (Eq. (4.4)), the expression for the supercurrent can be written in terms of single particle Green's functions [82],

$$\begin{aligned} I_{\rm sc} = -\frac{e v_{\rm qh}}{\beta L} \sum_m \Bigg[\int_0^L dx \, {\rm Tr}\Big[G(x,x;i\omega_m)\tau_z \Big] \\ - \int_{L+W}^{2L+W} dx \, {\rm Tr}\Big[G(x,x;i\omega_m)\tau_z \Big] \Bigg] . \end{aligned} \tag{4.6}$$

Here $G(x,x;i\omega_m)$ is the single-particle Green's function, $\omega_m = (2m+1)\pi/\beta$ is the Fermonic Matsubara frequency, and $\beta = 1/k_B T$ is the inverse temperature. Note that $G(x,x;i\omega_m)$ is singular for Hamiltonians which are first order in derivative (such as Eq. (4.5)). We regularize this singularity as $G(x,x;i\omega_m) = \lim_{\varepsilon\to 0}[G(x+\varepsilon,x;i\omega_m) + G(x-\varepsilon,x;i\omega_m)]/2$; however, our results are independent of the regularization scheme we choose.

To calculate the Green's function, we solve the defining differential equation

$(i\omega_m - H)\, G(x, x'; i\omega_m) = \delta(x - x')$. Assuming $0 < x < L$, integrating this equation around the QH edge $\delta(x - x')$ gives:

$$\lim_{\varepsilon \to 0^+} G(x - \varepsilon, x; i\omega_m) = M \left[\lim_{\varepsilon \to 0^+} G(x + \varepsilon, x; i\omega_m) \right]. \tag{4.7}$$

M is an x independent 2×2 matrix given by (explicit expression given in the Appendix),

$$M = e^{-\frac{2\omega_m}{\hbar}\left(\frac{L}{v_{\rm qh}} + \frac{W}{v_{\rm sc}}\right)} e^{i\mathbf{n}\cdot\boldsymbol{\tau}}, \tag{4.8}$$

where $\mathbf{n}$ is a three-component vector depending on the parameters of the system. Integrating the differential equation through the delta function from $x - \varepsilon$ to $x + \varepsilon$ gives the second equation:

$$\lim_{\varepsilon \to 0^+} \left[G(x + \varepsilon, x; i\omega_m) - G(x - \varepsilon, x; i\omega_m) \right] = -i/\hbar v_{\rm qh}. \tag{4.9}$$

Eqs. (4.7), (4.9) give a complete solution for the Green's function $G(x, x; i\omega_m)$ in our regularization scheme. Together with the straightforward extention of $G(x, x; i\omega_m)$ for $L + W < x < 2L + W$, we can calculate $I_{\rm sc}$ using Eq. (4.6).

4.3.1 Chiral nature of supercurrent and its interaction robustness

The chiral nature of the supercurrent is clear in Eq. (4.6). To see this consider the case where only one of the left/right going edges exist, i.e., the other edge is either obstructed or equivalently its length goes to infinity. In this limit for $\omega_m > 0$, $M \to 0$ which in turn shows $\lim_{\varepsilon \to 0^+} G(x - \varepsilon, x; i\omega_m) = 0$. Plugging this result back into Eqs. (4.6), (4.9), together with the straightforward extention to $\omega_m < 0$, gives vanishing supercurrent $I_{\rm sc} = 0$. Note that the crucial condition leading to this result

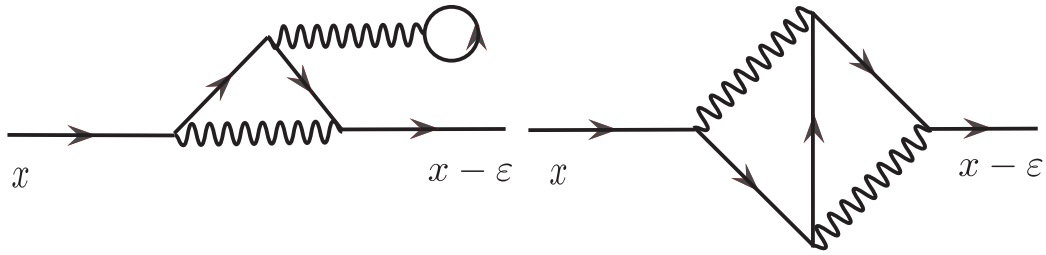

Figure 4.2: Typical Feynman diagrams used to calculate backward-propagating interacting Green's fucntion, $\lim_{\varepsilon\to 0^+} G(x-\varepsilon, x; i\omega_m)$. The solid lines are bare Fermionic propagators and the wiggly lines are propagators for the interaction. Note that our Feynman rule only allows a single connected string of bare Fermionic Green's function: this ensures that every diagram contributing to the backward propagating 'interacting' Green's fucntion contains at least one backward propagating 'bare' Green's fucntion, which leads to $\lim_{\varepsilon\to 0^+} G(x-\varepsilon, x; i\omega_m) = 0$.

is $G(x-\varepsilon, x; i\omega_m) = 0$, that is, absence of backward propagation in a chiral edge. This property is the key feature distinguishing chiral and non-chiral supercurrents (e.g. in quantum spin Hall edge states [106]).

One might wonder whether the introduction of interactions allows chiral quantum Hall edge states to carry non-chiral or conventional supercurrents through Cooper pair transport on the edge. Such a non-chiral supercurrent could potentially explain the conventional supercurrent periodicity observed in the experiment [99]. However, a non-zero non-chiral supercurrent turns out to be impossible and as we show below, a chiral quantum Hall edge state can only carry a chiral supercurrent.

To see this, we first note that Eq. (4.6) still holds in the presence of interactions (since extra interaction terms are not flux dependent). The defining equation of

the Green's function will be modified to $(i\omega_m - H - \Sigma)\, G(x, x'; i\omega_m) = \delta(x - x')$, where Σ is the interaction-induced self-energy (not to be confused with the self-energy in Eq. (4.1)). As long as Σ is finite, we can still integrate this equation to re-obtain Eq. (4.9). It is then easy to see that in the absence of backwards propagation, $\lim_{\varepsilon\to 0^+} G(x-\varepsilon, x; i\omega_m) = 0$, supercurrent still vanishes, $I_{\rm sc} = 0$. The limit $\lim_{\varepsilon\to 0^+} G(x-\varepsilon, x; i\omega_m)$ can be calculated using Feynman diagrams of the type shown in Fig. 4.2. However, the presence of at least one backward-propagating bare Fermionic Green's function in each diagram forces all terms to vanish identically, which in turn guarantees $\lim_{\varepsilon\to 0^+} G(x-\varepsilon, x; i\omega_m) = 0$ and $I_{\rm sc} = 0$ to infinite order in perturbation theory.

4.3.2 Explicit form of the supercurrent

We now return to the explicit calculation of $I_{\rm sc}$. Directly solving Eqs. (4.7), (4.9) to obtain the Green's function and using the results in Eq. (4.6) gives,

$$I_{\rm sc} = -\sum_{\omega_m} \frac{4e}{\beta\hbar} \sin\phi\, \sin^2\left(\frac{\Delta W}{\hbar v_{\rm sc}}\right) \left[(1+\cos\phi)\cos\left(\frac{2\Delta W}{\hbar v_{\rm sc}}\right) \right.$$
$$\left. +1 - \cos\phi - 2\cosh\left(\frac{2\omega_m}{\hbar}\left(\frac{L}{v_{\rm qh}} + \frac{W}{v_{\rm sc}}\right)\right)\right]^{-1}. \tag{4.10}$$

This equation gives the complete expression for the chiral supercurrent carried by the chiral edge states for the geometry in Fig. 4.1, and is consistent with the result of Ref. [88] in the limit of $L \gg W$. In the high-temperature limit, $\beta\hbar \ll (L/v_{\rm qh} + W/v_{\rm sc})$, this equation can be approximated as,

$$I_{\rm sc} \approx \frac{8e}{\beta\hbar} \sin\phi\, \sin^2\left(\frac{\Delta W}{\hbar v_{\rm sc}}\right) \exp\left[-\frac{2\pi}{\beta\hbar}\left(\frac{L}{v_{\rm qh}} + \frac{W}{v_{\rm sc}}\right)\right]. \tag{4.11}$$

4.4 Fraunhoffer periodicity

The current-phase relation can be obtained by including an external flux through the QH region. This can be incorporated by changing the gauge field $a(x)$ (Eq. (4.4)) to,

$$a(x) = \begin{cases} -\phi/2L + \phi_e/2L & \text{for } 0 < x < L \\ \phi/2L + \phi_e/2L & \text{for } L + W < x < 2L + W \\ 0 & \text{elsewhere} \end{cases}, \tag{4.12}$$

where ϕ_e is the dimensionless external flux related to the actual flux ϕ_{ext} as $\phi_{\text{ext}} = \phi_e \frac{\phi_0}{\pi}$; $\phi_0 = h/2e$, is the superconducting flux quantum.

Including the flux ϕ_e in our calculation changes the supercurrent in Eq. (4.10) to

$$\begin{aligned} I_{\text{sc}}(\phi_e) = &-\sum_{\omega_m} \frac{4e}{\beta\hbar} \sin\phi \, \sin^2\left(\frac{\Delta W}{\hbar v_{\text{sc}}}\right) \\ &\times \left[(\cos\phi_e + \cos\phi)\cos\left(\frac{2\Delta W}{\hbar v_{\text{sc}}}\right) + \cos\phi_e - \cos\phi \right. \\ &\left. -2\cosh\left(\frac{2\omega_m}{\hbar}\left(\frac{L}{v_{\text{qh}}} + \frac{W}{v_{\text{sc}}}\right)\right)\right]^{-1}. \end{aligned} \tag{4.13}$$

We remark that in the parameter regime probed in the experiment, the $\cosh\left(\frac{2\omega_m}{\hbar}\left(\frac{L}{v_{\text{qh}}} + \frac{W}{v_{\text{sc}}}\right)\right)$ term is by far the largest term of the denominator in the expression above. Moreover, the $m = 0, -1$ terms in the Matsubara frequency dominate. We can then approximate I_{sc} as (after Taylor expanding the denominator),

$$I_{\text{sc}}(\phi, \phi_e) \approx \left(I_{\text{ch0}} + I_{\text{ch1}} \cos\phi_e\right) \sin\phi. \tag{4.14}$$

4.5 Comparison with the experimental results

Using the experimental parameters of Ref. [99] ($\Delta = 1.2meV = 13.9K$, $W = 2.4\mu m$, $L = 0.3\mu m$, $T = 40mK$, $B = 1T$, cyclotron radius $r_c = 25nm$, and surface transparency $|t| \approx 0.7$), we can estimate edge velocities semi-classically (see Eq. (4.3)) as $v_{\rm qh} \approx 7.0 \times 10^5 m/s$ and $v_{\rm sc} \approx 3.9 \times 10^4 m/s$. Substituting these values into Eq. (4.10) gives the magnitude of the supercurrent $I_{\rm sc} \approx 0.9nA$, which is remarkably close to the experimental value of $I_{\rm sc} = 0.5nA$. One should note that the agreement is reached in spite of the fact that $I_{\rm sc}$ has exponential dependence on, and is thus very sensitive to, the edge velocities ($v_{\rm qh}$ and $v_{\rm sc}$). This demonstrates that quantitative agreement in the chiral supercurrent can be attained by making reasonable and critical assumptions about the SC/QH interface. Crucially, the exponential form of Eq. (4.11) shows that the velocity renormalization and the surface transparency along the SC/QH interface play the main role in controlling the magnitude of supercurrent.

The supercurrent (Eq. (4.11)) depends exponentially on both the width of the superconducting contact (W) and the length of the QH sample (L). However, their coefficient in the exponent is very different in magnitude since the edge velocity renormalization (Eq. (4.3)) results in an order of magnitude difference between $v_{\rm qh}$ and $v_{\rm sc}$. Therefore, W plays a crucial role in controlling the value of $I_{\rm sc}$, varying L does not significantly change its magnitude. This is consistent with Ref. [99], where they observe such a tendency while measuring the supercurrents for devices with different dimensions. Moreover, and perhaps counter-intuitively, we find that

decreasing the surface transparency of the SC/QH interface $|t|$ can lead to an increase in the magnitude of $I_{\rm sc}$. Eq. (4.3) suggests that a smaller value of $|t|$ leads to larger $v_{\rm sc}$, which also results in a larger $I_{\rm sc}$; this agrees with the experiment in Ref. [99], as they observe larger value of $I_{\rm sc}$ in the p-doped devices. The p-doped regime manifestly has lower surface transparency due to the pn junctions that are formed close to the contacts.

Let us now discuss the periodicity of the current-phase relation. The *critical* chiral supercurrent $I_{\rm sc}$ dependence on the external flux ϕ_e can be approximated as (from Eq. (4.14)),

$$I_{\rm sc}^{\rm c}(\phi_e) \equiv \max_{\phi} I_{\rm sc}(\phi, \phi_e) \approx |I_{\rm ch0} + I_{\rm ch1} \cos \phi_e|, \tag{4.15}$$

where, for the parameters we use, the ϕ_e independent term is $I_{\rm ch0} = 0.9 \times 10^{-9} A$, and the ϕ_e dependent term has $I_{\rm ch1} = 1.0 \times 10^{-11} A$. In apparent contradiction with the experiment (which is $\phi_0 = h/2e$ periodic), this expression suggests the supercurrent has a $2\phi_0 = h/e$ periodicity. However, it is notable that in our parameter regime (which is also that of Ref. [99]), the external flux dependence of $I_{\rm sc}$ is strongly suppressed in the sense that $I_{\rm ch1}$ is two orders of magnitude smaller than $I_{\rm ch0}$. Also note that the Fraunhoffer pattern of the chiral supercurrents do not form nodes as in conventional supercurrents [1].

Given the strongly suppressed oscillations from the chiral supercurrent, one might wonder whether the experimentally observed period can be attributed to residual non-chiral supercurrent propagating through the system. Such non-chiral contributions can arise from, e.g., inhomogeneities in the confining potential near

the edge. However, including such contributions (assuming they are smaller than I_{ch0}) does not change the periodicity. This chapter focuses on the magnitude of the supercurrent. While we are able to show that the measured magnitude of the critical current is consistent with our theory, the periodicity is still off by a factor of two. This might still be taken as evidence against interpreting the experiment as a chiral supercurrent. However, it is also possible that non-perturbative interaction effects not accounted for in our model lead to a shorter-period modulation of the critical current.

4.6 Discussion and conclusion

In this chapter we have studied the chiral supercurrent in a SC/QH/SC system for various system parameters. We have found that the finite junction transparency (consistent with normal state transport) and velocity renormalization along the SC contacts are crucial to obtain the correct order of magnitude of the supercurrent. In addition, we have found that in the high-temperature limit, $\beta\hbar \ll (L/v_{\mathrm{qh}} + W/v_{\mathrm{sc}})$, both the flux-averaged and flux-dependent (giving $2\phi_0 = h/e$ periodic Fraunhoffer pattern) chiral supercurrents go to zero exponentially with junction width with exponents $W\left[\frac{2\pi}{\beta\hbar}\left(\frac{L}{Wv_{\mathrm{qh}}} + \frac{1}{v_{\mathrm{sc}}}\right)\right]$ and $2W\left[\frac{2\pi}{\beta\hbar}\left(\frac{L}{Wv_{\mathrm{qh}}} + \frac{1}{v_{\mathrm{sc}}}\right)\right]$, respectively.

We discussed the chiral nature of the supercurrent and showed that this "chiral nature" can be used as a sharp definition for chiral supercurrents even in presence of the electron-electron interactions.

Chapter 5: Ferromagnetism and its stability from the one-magnon spectrum in twisted bilayer graphene

5.1 Overview

Ferromagnetism is the most familiar form of magnetic order. Despite the long history of ferromagnetism, most of our current understanding is based on simple Hartree-Fock (mean-field) calculations [1]. These calculations are known to greatly overestimate the ferromagnetic tendency of electronic systems. Several improvements over the Hartree-Fock method have been proposed [107, 108]. Nonetheless, the overall progress in this direction, has not led to a theory that provides reliable diagnostics for which systems would be ferromagnetic.

A practical, useful guide is provided by the Hund's rule, that predicts ferromagnetic spin-polarization in partially filled degenerate sets of energy states (orbitals). Specifically, the exchange term in the Coulomb interaction reduces the Coulomb repulsion between electrons of similar spin, favoring spins to align with each other. Interestingly, the same general principle appears to apply to quantum Hall ferromagnetism. In both of these cases, the degeneracy of the non-interacting energy eigenstates seems essential to enhance the effect of the ferromagnetic exchange.

While a faithful treatment of magnetism in electronic systems is complicated, the limit of strong on-site Coulomb interaction U, the so-called Hubbard interaction [109], has been demonstrated to lead to anti-ferromagnetic Neél order on an energy-scale proportional to Heisenberg super-exchange [1]. The magnetic order has been shown to flip to ferromagnetism in the limit of exactly one hole and infinite onsite repulsion U [110, 111]. These results were extended by Lieb to the half-filled Hubbard model with an imbalance in the number of sub lattices [112], establishing the possibility of itinerant ferromagnetism. These ideas of enhancement of magnetism by local interaction and of ferromagnetism by degeneracy of non-interacting states were later shown to reinforce each other through the demonstration of ferromagnetism in half-filled lattice models with Hubbard interactions that have a degenerate manifold of states in the form of a flat band [113–125]. The latter class of results constitute what is usually called "flat band ferromagnetism".

Despite the large variety of theoretical models demonstrating spontaneous ferromagnetism as well as competing magnetic and itinerant phases, physical realizations of such models are lacking. Recent experimental breakthroughs in the area of multi-layer graphene both in the quantum Hall regime and without magnetic fields provide hope for the realization of such systems. In the quantum Hall regime, graphene provides the opportunity to break the flatness of a Landau level by introducing a lattice potential on the scale of a magnetic length that has been shown to create a Hofstadter spectrum [126]. Based on arguments in the previous paragraphs, one expects such a broadening of the Landau levels to compete with quantum Hall ferromagnetism in an interesting way. The latter case of multi-layer graphene with-

out a magnetic field is a more unexpected direction and appears to show evidence of ferromagnetism. More specifically, large peaks in density of states associated with nearly- flat bands and the concomitant appearance of correlated phenomena have recently been observed in twisted bilayer, twisted double-bilayer, and ABC trilayer graphene [127–141]. Some of these systems have also shown evidence for ferromagnetism [132, 134–137, 140, 141] near the "flat-band" limit. Additionally, the possibility of tuning these systems out of the "flat-band" regime suggests the fascinating possibility of studying multiple phases and transitions between them is insulating and itinerant magnetic systems.

In this chapter, we consider the particular example of twisted-bilayer graphene (TBLG). We start by focusing on the so-called "chiral" limit of the realistic models for TBLG, where the spectrum supports a band that is exactly flat [142–144]. We work with a particular form of Hubbard interaction that we argue can emerge from Thomas-Fermi screening of the Coulomb interaction. We then show that in this limit and at filling fractions $\pm 3/4$, the saturated spin and valley polarized states are ideal candidates for ground states of the system. By assuming a large enough substrate (hBN) induced sub-lattice potential, the same argument can be shown to hold for filling fractions $\pm 1/4$. The topology of the TBLG band structure guarantees that all the ferromagnetic states discussed above are also associated with a quantized anomalous Hall response [145, 146]. We study the local stability of the ferromagnetic phase around the chiral limit by studying the *exactly* calculated spectrum of one-magnon excitations. The instability of the ferromagnetic state is signaled by a negative magnon excitation energy. This approach allows us to de-

form the results from the idealized chiral model (by increasing the bandwidth and/or modified interactions) towards results for more realistic systems. We use the low energy part of the exact one-magnon spectrum to predict the spin stiffness of the Goldstone modes in the ferromagnetic phase as the realistic system is approached. The effect of spin stiffness can be potentially determined from skyrmion-induced transport phenomena.

5.2 Band structure of TBLG

TBLG corresponds to two layers of graphene stacked on top of each other with a relative twist angle θ. For small twist angles θ, and within the leading harmonic approximation, this system forms a periodic pattern called a Moiré pattern. In this limit, the noninteracting physics can be well approximated by the Bistritzer and Macdonald continuum model [147, 148]. Following the notation of Ref. [149], the dimensionless single-valley ($\zeta = \pm 1$ is the valley index) Bistritzer and MacDonald Hamiltonian can be written in the layer $(1, 2)$ and sub-lattice (A, B) basis (A_1, B_1, A_2, B_2) as,

$$H_{\mathrm{BM}}^{\zeta} = \begin{pmatrix} H_1 & U^{\dagger}(\mathbf{r}) \\ U(\mathbf{r}) & H_2 \end{pmatrix}, \tag{5.1}$$

where

$$H_l = -R(\pm\theta/2)(k - K_{\zeta}^{l}).(\zeta\sigma_x, \sigma_y) + \Delta_l \sigma_z \tag{5.2}$$

and,

$$U(\mathbf{r}) = \begin{pmatrix} \alpha_0 & \alpha_1 \\ \alpha_1 & \alpha_0 \end{pmatrix} + \begin{pmatrix} \alpha_0 & \alpha_1 e^{-2\pi i\zeta/3} \\ \alpha_1 e^{2\pi i\zeta/3} & \alpha_0 \end{pmatrix} e^{i\zeta G_1.r} \tag{5.3}$$
$$+ \begin{pmatrix} \alpha_0 & \alpha_1 e^{2\pi i\zeta/3} \\ \alpha_1 e^{-2\pi i\zeta/3} & \alpha_0 \end{pmatrix} e^{i\zeta(G_1+G_2).r}.$$

Here, G's are the reciprocal lattice vectors of the Moiré lattice, and K_ζ^l's are the location of monolayer Dirac points in the Brillouin zone. Δ_l's are the (hBN) induced sub-lattice potentials. In monolayer graphene Δ is known to be able to reach around $\Delta \approx 0.1 - 0.2$ (in the dimensionless units used here or, equivalently, $15 - 30$ meV) [150–152].

The dimensionless parameters α_0, α_1 are given by,

$$\alpha_0 = \frac{3w_{AB}a_0}{8\pi v_0 \sin(\theta/2)} \ ; \ \alpha_1 = \alpha_0 \frac{w_{AA}}{w_{AB}}. \tag{5.4}$$

a_0 and v_0, are respectively, the monolayer graphene's lattice spacing and the Fermi velocity. w_{AB} and w_{AA} are roughly, the hopping amplitudes in the AA and AB/BA stacking regions respectively. In the realistic system α_0 is expected to be around $\alpha_0 \approx 0.586(1)$ and $\frac{w_{AA}}{w_{AB}}$ is expected to be around $\frac{w_{AA}}{w_{AB}} \approx 0.8$ [149]. Many interesting features related to this non-interacting model has been extensively studied in the past year [153–163].

5.3 Interaction model for TBLG

In this chapter, we mostly work with a simple yet reasonable model for interactions in TBLG. The effect of more general interactions is discussed later.

We start by considering the RPA screened Coulomb interaction $V(q)$. The exact $V(q)$ has been found to be rather complicated [164]. An approximation for the small-q behavior of $V(q)$ can be obtained from simple Thomas-Fermi screening arguments. A rough estimate for the Thomas-Fermi screening wave-vector q_{TF} can be obtained from the monolayer-graphene results of Ref. [165] (by using a renormalized Fermi velocity). This results suggest that $G_{Moiré} \ll q_{\mathrm{TF}} \ll G_{\mathrm{graphene}}$. Since $q_{\mathrm{TF}} \ll G_{\mathrm{graphene}}$, in this regime the interaction is independent of layer and sub-lattice separation (these distances are much smaller than $1/q_{\mathrm{TF}}$). Also the rotation angle θ is small; therefore its effect on inter-particle distance can be dropped (interaction becomes layer independent). Note that the low-energy states included in the continuum model of Bistritzer and MacDonald are only the states close to Dirac points $|k - K| < \mathcal{O}(1)G_{Moiré}$. Since $G_{Moiré} \ll q_{\mathrm{TF}}$, in this regime $V(q)$ is effectively constant. Similarly, because $q_{\mathrm{TF}} \ll G_{\mathrm{graphene}}$, the inter-valley scattering terms are strongly suppressed, and the valley index becomes an effective good quantum number (approximate $U(1)_v$ symmetry). Putting everything together leads to the following simplified form of the interaction:

$$V = U \sum_{q} \sum_{(\sigma',v',s',l') \neq (\sigma,v,s,l)} \rho_{\sigma,v,s,l}(q) \rho_{\sigma',v',s',l'}(-q). \tag{5.5}$$

Here $\rho_{\sigma,v,s,l}(q) = \sum_k c^{\dagger}_{\sigma,v,s,l,k+q} c_{\sigma,v,s,l,k}$ is the density wave operator. σ, v, s, l are the spin, valley, sub-lattice, and layer indices, respectively. The term with all the indices equal is dropped since it only renormalizes the chemical potential (which is irrelevant at a fixed filling).

5.4 Ferromagnetism in the perfectly flat band limit of TBLG

Let us now consider the effect of the interaction Eq. 5.5 on TBLG in the chiral limit ($\alpha_0 = 0.586$ and $\alpha_1 = 0$ in Eq. (5.3)). In this limit, the flat-band wave-functions can be taken to be sub-lattice polarized [142] so that the sub-lattice index s is a good quantum number in addition to σ, v. We now have 8 degenerate flat bands that can be labeled by spin, valley and sub-lattice indices σ, v, s.

Assuming the interaction parameter U is small compared to the band gap W, we can consider an effective Hamiltonian,

$$H_t = U \sum_{q,l,l',f\neq f'} P_0 \rho_{f,l}(q) P_0 \rho_{f',l'}(-q) P_0, \tag{5.6}$$

where P_0 is the projection operator onto the flat bands and f refers to the collective σ, v, s, l. This Hamiltonian (that we focus on here) differs from Eq.(5.5) by "intra-flavor inter-layer" terms ($l \neq l'$ and $f = f'$). Later, we will show numerically that these terms do not have a significant effect on the ground state. The projected density operators $P_0 \rho_{f,l}(q) P_0$ in H_t commute with the kinetic energy term in the flat-band limit, so that we can ignore the kinetic energy. A spin, valley and sub-lattice polarized state corresponding to fully filling one of these bands labeled by $|f = f_0\rangle = \prod_{k\in \mathrm{MBZ}} c^\dagger_{f_0,k}|0\rangle$ is a null state (i.e. zero-energy eigenstate) of H_t. To see this note that

$$P_0 \rho_{f,l}(q) P_0 |f = f_0\rangle = \sum_{G_{\text{Moiré}}} \Lambda_l(G_{\text{Moiré}}) \delta_{f,f_0} \delta_{q,G_{\text{Moiré}}} |f = f_0\rangle, \tag{5.7}$$

which implies that

$$H_t|f = f_0\rangle = U \sum_{G_{\text{Moiré}}, G'_{\text{Moiré}}, l, l', f \neq f'}$$

$$\Lambda_l(G_{\text{Moiré}})\Lambda_{l'}(G'_{\text{Moiré}})\delta_{f,f_0}\delta_{f',f_0}|f = f_0\rangle = 0. \tag{5.8}$$

Note that the Hamiltonian in H_t in Eq. 5.6 is non-negative i.e. $\langle H_t \rangle \geq 0$. This becomes manifest if we Fourier transform back into "real" space,

$$H_t = U \int d^2\boldsymbol{r} \sum_{l,l',f \neq f'} (P_0 n_{f,l}(\boldsymbol{r}) P_0)(P_0 n_{f',l'}(\boldsymbol{r}) P_0), \tag{5.9}$$

where $n_{f,l}(\boldsymbol{r})$ is the real-space density operator. The two parts of each product term commute as they are associated with different values of f. They are also both non-negative as they are projected non-negative operators.

Therefore, the null state $|f = f_0\rangle$ is an exact ground state of H_t at filling of $-3/4$ (one electron per unit cell) of the flat-band manifold. Since the chiral limit Hamiltonian is particle-hole symmetric, the same results also hold for the opposite filling fraction $+3/4$. That is, the fully polarized state is an exact ground state at fillings $\pm 3/4$. By assuming large enough (substrate induced) sub-lattice potential $\Delta_t = \Delta_b > U$, the same result can be easily generalized for filling fractions $\pm 1/4$. Note that the band structure properties of TBLG guarantees that all of the ferromagnetic states discussed here are also associated with a quantized anomalous Hall response [145, 146, 166]. Within our formalism, we cannot find a justification for considering ferromagnetic states at $\pm 1/2$ or 0(charge-neutrality) fillings. In fact, we believe it is likely that the true ground state of the model at these fillings is not ferromagnetic. However, the mean-field studies of Refs. [167–170], find that the

spin/valley polarized states are good ground state candidates even at $\pm 1/2, 0$ filling.

5.5 spin stiffness and the stability of ferromagnetism in TBLG.

We now turn to discussing the stability of this ferromagnetic state using the one-magnon spectrum. This is a crucial step as it provides a non-trivial consistency check and allows us to generalize the results of the idealized model (Eq. 5.6) to more realistic systems. If the system is truly ferromagnetic, it is necessary but not sufficient for the $q = 0$ state to have the minimum energy (since it is related to the fully polarized state by a $SU(2)$ rotation). This establishes the ferromagnetic state as the local energy minimum. We note that even though in principle the local stability of ferromagnetic state is not enough to guarantee global stability, application of our method to a few known examples (in the appendix) suggests that in practice the ferromagnetic region of the phase diagram can be identified effectively. We can further use the one-magnon band spectrum of the system to obtain useful information like spin stiffness.

A combination translation invariance and flavor conservation ensures that the one-magnon (single-spin or valley flip) Hilbert space is small enough to be accessible using exact diagonalization. We use the *exactly* calculated one-magnon spectrum to study the stability of the ferromagnetic state. The exactly calculated band-structure of the one-magnon excitations using the interaction V (Eq. 5.5) is shown in Fig.5.1. The blue curve corresponds to the single-spin flip branch of excitations associated with the $SU(2)$-breaking Goldstone mode. The red curve corresponds to the single-

valley flip branch of excitations associated with breaking of time-reversal symmetry. Importantly, note that since time-reversal symmetry is discrete, the single-valley flip excitations are gapped. As shown in Fig. 5.1 the ferromagnetic state is stable in this case.

The numerical stability of the ferromagnetic state shows that the "intra-flavor inter-layer" terms

$$\Delta H_t = 2U \sum_q \sum_f P_0 \rho_{f,l=1}(q) P_0 \rho_{f,l=2}(-q) P_0. \tag{5.10}$$

that were ignored in the analytic arguments based on Eq. 5.6 do not significantly affect the ferromagnetism (we have checked that this term only causes small corrections to the one-magnon spectrum). This term favors layer polarization. However, even approximately layer polarized states do not exist in the flat band subspace (layer polarization is largely fixed by the non-interacting flat-band wave functions). Additionally, such terms constitute a combinatorially small fraction 1/28 of the total terms of Eq.(5.5). Adding this term to Eq.(5.6) can be thought of as deviating the ideal interaction form of Eq.(5.6) towards the more realistic interaction in Eq.(5.5).

We now deviate from the chiral limit and proceed to study the stability of the ferromagnetic state as the realistic system is approached. For simplicity, here we assume a substrate-induced sub-lattice potential $\Delta_t = \Delta_b = 0.1 \approx 18meV$. This assumption gaps one of the flat bands and helps with the computational complexity. We numerically calculate the one-magnon (single spin-flip) spectrum as we approach the realistic parameters $w_{AA}/w_{AB} = 0.8$ [149]. The instability of the ferromagnetic state is identified by a sign-change of the spin stiffness, or more precisely by looking

for one-magnon states whose energies are lower than the ferromagnetic state. Sample results are shown in Fig. 5.2. In Fig. 5.2 we have set $U = 0.005 \approx 1meV$. As shown in the figure, as the realistic parameters are approached, the ferromagnetic state becomes unstable. To study this transition more carefully, we have plotted the calculated value of spin stiffness ρ_s as a function of w_{AA}/w_{AB} for three different values of U in Fig.5.3. ρ_s is extracted assuming $E = \rho_s|k|^2$. Note that as the instability is approached, the spectrum sometimes does not admit a good quadratic fit. Still, the extracted value can be used to see the general trend. As shown in Fig. 5.3, depending on the value of U, the realistic system can be either ferromagnetic or not. That is, for large enough U, in the realistic parameter regime, the ferromagnetic state is stable. Within the parameter regime used here, we estimate the critical value of U_c to be around $U_c \approx 2meV$.

Before ending this section, we emphasize that our formalism can be applied to *arbitrary* interaction models, and that the model considered here only provides an example that can be generalized to more complicated models in future work.

5.6 Discussion and Conclusion

In this chapter, we have shown that a simple variant of the ideas related to flat band ferromagnetism can be used to study the in TBLG. In particular, we discussed ferromagnetism in the perfectly flat band "chiral" limit, and used the exactly calculated one magnon spectrum to study the stability of the ferromagnetic state as the realistic system is approached. The same one-magnon spectrum is also used to extract the

spin stiffness of the ferromagnetic Goldstone modes. Note that our formalism can be used to study ferromagnetism in other recently discovered ferromagnetic phases in Moiré superlattices. In particular, the same exact method can be readily applied to twisted double bilayer graphene, where an analogous chiral flat limit exists [144].

A particularly intriguing feature of the results presented here is that (as opposed to mean-field approach [167–169]) they manifestly predict ferromagnetism *only* at odd filling fractions $\pm 3/4, 1/4$. Given that the experimentally observed half-filled state seems to be spin-unpolarized [127–129], it would be interesting to study the fate of the model presented here at half-filling and to see if it also hosts a spin-unpolarized ground state.

The exactly calculated one-magnon spectrum studied here can be used to extract other interesting information about the ferromagnetic state. In particular, the Chern insulating nature of the ferromagnetic states means that the spin stiffness can be used to calculate the energy of charged skyrmions [171–176]. The skyrmion energy in combination with the Hartree-Fock particle-hole excitation energy can then be used to determine whether skyrmions are the lowest lying charged excitations (note that even in Landau levels, this is not always the case). These results can be compared with experimentally measured charge gaps of Ref. [141]. We further remark that the one-magnon spectrum can also be used to identify natural candidates for the neighboring magnetic phases. Specifically, when the ferromagnetic state becomes unstable, that is when the minimum of the one-magnon spectrum has finite momentum $q_0 \neq 0$, the location of this new minimum in the Brillouin zone can be used to identify natural candidates for alternate types of magnetic order (e.g.

anti-ferromagnetism) that might replace ferromagnetism in neighboring phases.

We finally mention that the formalism developed here provides an intuitive picture of how ferromagnets are favored over competing Mott insulators in topologically non-trivial bands. Traditionally, when short-range Hubbard interactions are considered, Mott insulating states are as considered as candidate ground states. The idea is to restrict the electrons to sharply localized non-overlapping Wannier wave-functions to minimize the interaction energy. However, note that for non-isolated or isolated and topologically non-trivial bands, Wannier wave-functions are not even approximately localized. Therefore, in these cases (overlapping or topologically non-trivial band), Mott insulating states are not good ground-state candidates. However, the ferromagnetic states discussed above are good candidates independent of the (topological-)nature of the underlying band. In continuation of these ideas, we mention here that the recent experimental finding of Ref. [137] in ABC trilayer graphene, where the Chern number of the band can be electrically tuned, seems to suggest that the topology of the underlying band might in fact play a role in favoring ferromagnetism. Studying this case with the same formalism provides another interesting line of future work.

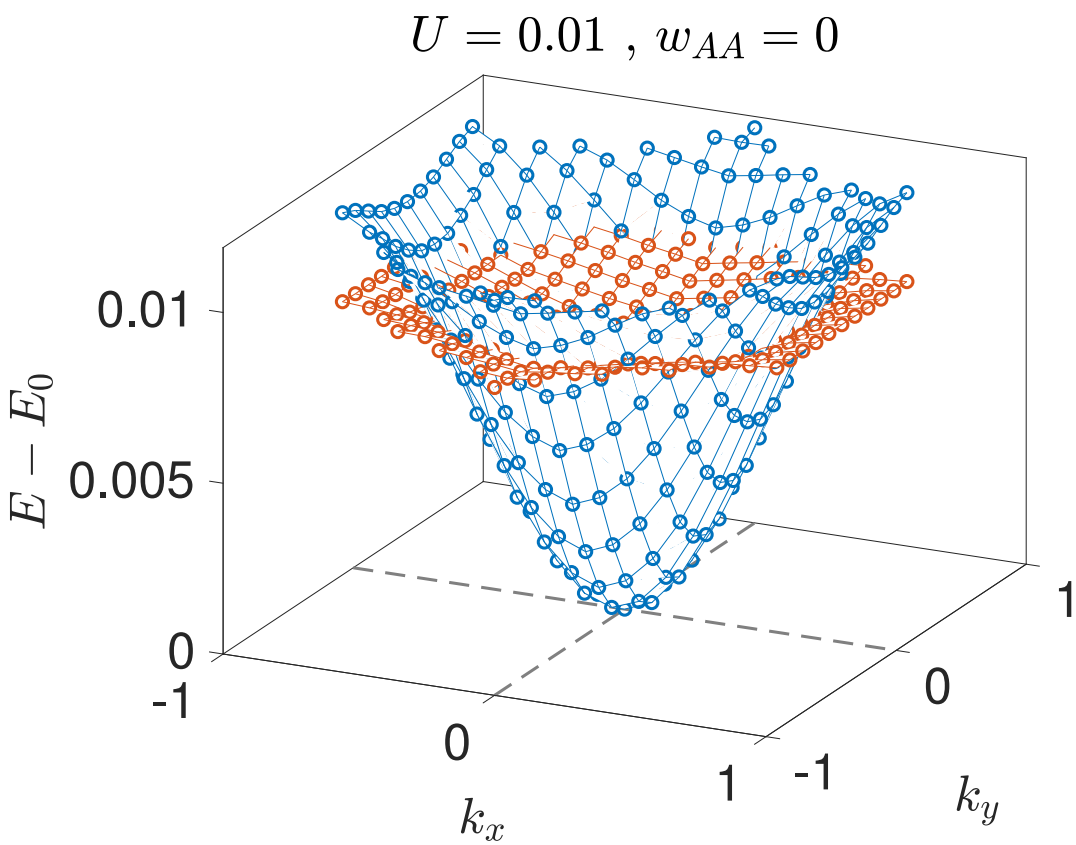

Figure 5.1: Lowest one-magnon band spectrum of the TBLG in the chiral limit. Energies are measured with respect to the fully polarized state. The gapless blue curve corresponds to the single-spin flip branch associated with the $SU(2)$ breaking Goldstone mode. The gapped red curve corresponds to the single-valley flip branch associated with breaking the discrete time-reversal symmetry. Energies are in units of $\frac{8\pi v_0 \sin(\theta/2)}{3a_0} \approx 0.19$eV. k_x and k_y are in units of $\frac{8\pi \sin(\theta/2)}{3a_0}$. We have used the interaction form V (Eq.(5.5)).

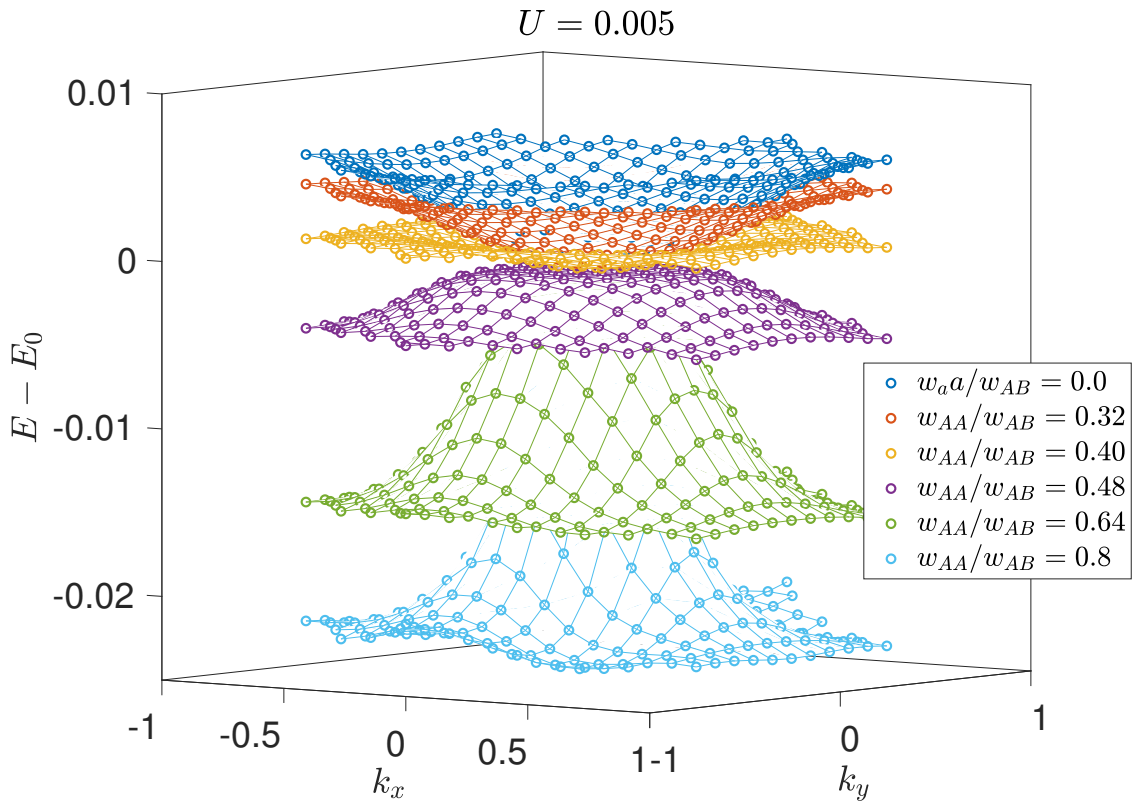

Figure 5.2: Lowest one-magnon (single spin-flip) band spectrum of the TBLG as the realistic system is approached. Energies are measured with respect to the fully polarized state in the chiral limit. Energies are in units of $\frac{8\pi v_0 \sin(\theta/2)}{3a_0} \approx 0.19$eV. Here $\Delta_t = \Delta_b = 0.1 \approx 18meV$. k_x and k_y are in units of $\frac{8\pi \sin(\theta/2)}{3a_0}$.We have used the interaction form V (Eq.(5.5)).

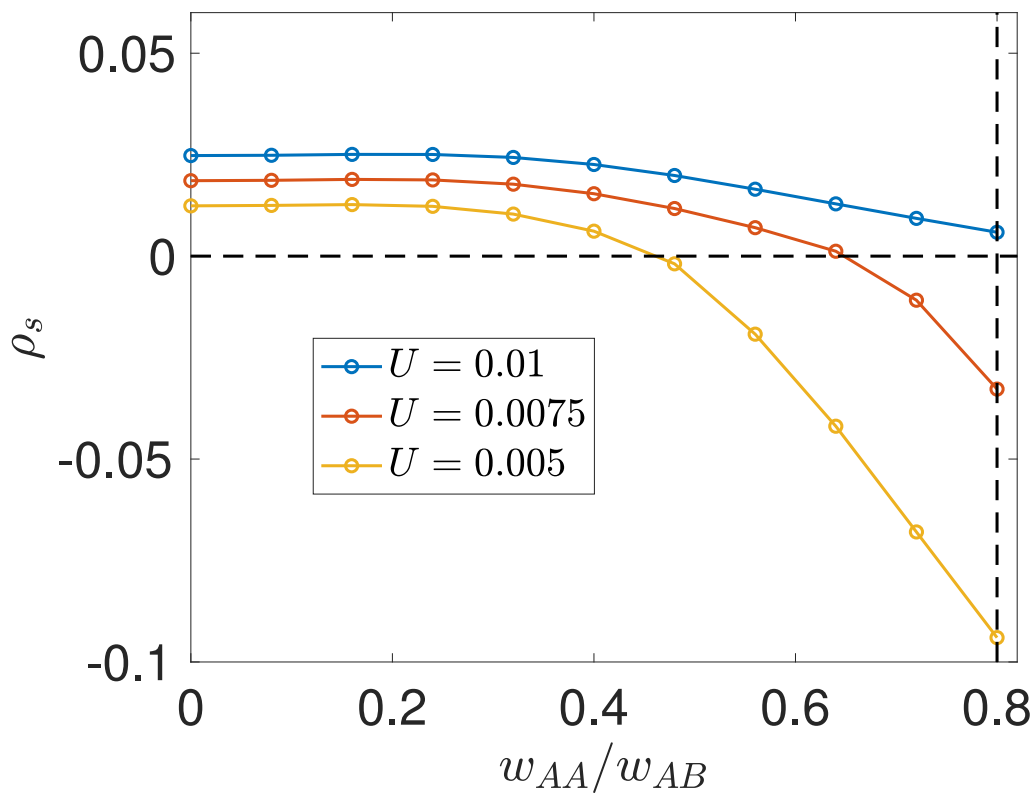

Figure 5.3: spin stiffness associated with the one-magnon band spectrum of the TBLG. A negative spin stiffness signals the instability of the ferromagnetic state. We have used a fit tos the form $E = \rho_s|k|^2$. We have used the interaction form V (Eq.(5.5)).

Chapter 6: Summary and Conclusion

Topological quantum materials provide a rich playground in which we can observe a wide array of fascinating phenomena, e.g. quantized Hall conductance, zero bias conductance peaks, and protected gapless edge modes. In the past few decades, it has been realized that unique properties of topological quantum materials can potentially have enormous technological applications, specifically, in topological quantum computation. However, as discussed extensively throughout this thesis, in practice identifying unambiguous signatures of topology and using them for real-world applications is extremely difficult. In this work, we tried to understand such difficulties by studying a number of specific examples and to find ways to overcome these problems. In the following, we conclude by providing a brief summary of the findings of each chapter.

In Chapter 1, we gave a short introduction to the major classes of topological quantum materials and listed problems associated with real-world realizations and applications of such material.

In Chapter 2, we studied the chiral magnetic effect in Weyl semimetals. In particular, we showed that despite common belief, a chiral magnetic effect like response, that is a transient flow of a current parallel to an applied external magnetic field,

is in principle possible with or without Weyl nodes. Furthermore, we showed that finite-frequency CME can be non-vanishing in general when there is a non-vanishing Berry curvature on the Fermi surface. However, existence of Berry monopoles are not necessary. We demonstrated that our analysis holds even in presence of disorder.

In Chapter 3, we provided an experimental proposal to realize $\mathbb{Z}_3$ parafermionic zero modes in a realistic experiment. We showed that a linear array of superconducting quantum-dot-like holes on top of a quantum spin singlet 2/3 fractional quantum Hall states can be used to realize $\mathbb{Z}_3$ parafermions without using Andreev back-scattering. We argued that the latter feature makes our proposal ideal for experimental realization, using only ingredients that have been already experimentally obtained.

In Chapter 4, we studied the experimentally fascinating phenomenon of chiral supercurrent through a quantum Hall weak link. We provided a detailed calculation of supercurrent in SC/AH/SC junctions and found that the obtained supercurrent, calculated for experimentally reasonable parameters, is quantitatively consistent with existing experiments. We then showed that an ideal chiral quantum Hall edge state, even when interactions are included to all orders in perturbation theory, only carries chiral supercurrent, and claimed that this can be used as a sharp definition for chiral supercurrents, even in presence of the interactions and disorder.

In Chapter 5, we turned our attention to the problem of the quantum anomalous Hall effect and flavor ferromagnetism in twisted bilayer graphene. We demonstrated that a generalization of the "flat band ferromagnetism" can be used to study the quantum anomalous Hall effect in twisted bilayer graphene. We argued

that the numerically calculable one-magnon spectrum can be used as a tool to study the stability of the ferromagnetic state in this system, which provides a novel and nontrivial improvement over the widely used mean-field approximations. The one-magnon spectrum can be also used to extract experimentally relevant quantities like the spin-stiffness of the ferromagnetic Goldstone modes and the energy of charged topological skyrmions.

Appendix A: Appendix to Chapter 2

A.1 Details of the clean linear response calculation

Here we explicitly show how to get from equations (2.17) and (2.20) to equation (2.22). In the limit we are interested in (i.e. $\lim_{q\to 0}\lim_{\omega\to 0}$) we can re write equation (2.20) as :

$$e^2 \sum_{n,m\neq n,k} \frac{f(\varepsilon_{n,\mathbf{k}-\frac{\mathbf{q}}{2}}) - f(\varepsilon_{m,\mathbf{k}+\frac{\mathbf{q}}{2}})}{\varepsilon_{n,\mathbf{k}-\frac{\mathbf{q}}{2}} - \varepsilon_{m,\mathbf{k}+\frac{\mathbf{q}}{2}}} \langle n,\mathbf{k}-\frac{\mathbf{q}}{2}|\hat{J}_a(\mathbf{k})|m,\mathbf{k}+\frac{\mathbf{q}}{2}\rangle\langle m,\mathbf{k}+\frac{\mathbf{q}}{2}|\hat{J}_b(\mathbf{k})|n,\mathbf{k}-\frac{\mathbf{q}}{2}\rangle \tag{A.1}$$

$$+e^2 \sum_{n,k} f'(\varepsilon_{n,\mathbf{k}})\langle n,\mathbf{k}-\frac{\mathbf{q}}{2}|\hat{J}_a(\mathbf{k})|m,\mathbf{k}+\frac{\mathbf{q}}{2}\rangle\langle m,\mathbf{k}+\frac{\mathbf{q}}{2}|\hat{J}_b(\mathbf{k})|n,\mathbf{k}-\frac{\mathbf{q}}{2}\rangle$$

We now expand to first order in $\mathbf{q}$ and keep only the anti-symmetric part, for simplicity we divide the expression to four terms each corresponding to the expansion of :

1.the numerator of the first term.(Π_1)

2.the denominator of the first term.(Π_2)

3.the matrix element in the first term.(Π_3)

4.the matrix element in the second term.(Π_4)

Now we calculate each one as follows ($\mathbf{v}_{n,\mathbf{k}} = \nabla_{\mathbf{k}}\varepsilon_{n,\mathbf{k}}$ everywhere below):

$$(\Pi_1)^{ant} = -e^2 \sum_{n,m\neq n,k} f'(\varepsilon_{n,\mathbf{k}})(\mathbf{v}_{n,\mathbf{k}}.\frac{\mathbf{q}}{2})\frac{\langle n,\mathbf{k}|\hat{J}_a(\mathbf{k})|m,\mathbf{k}\rangle\langle m,\mathbf{k}|\hat{J}_b(\mathbf{k})|n,\mathbf{k}\rangle}{\varepsilon_{n,\mathbf{k}}-\varepsilon_{m,\mathbf{k}}} \tag{A.2}$$

$$= ie^2 \sum_{n,m\neq n,k} f'(\varepsilon_{n,\mathbf{k}})(\mathbf{v}_{n,\mathbf{k}}.\mathbf{q})(\mathbf{m}_n(\mathbf{k}))_c$$

after shifting $\mathbf{k}$ to $\mathbf{k}-\frac{\mathbf{q}}{2}$, for Π_2 we have:

$$(\Pi_2)^{ant} = ie^2 \sum_{n,m\neq n,k} f(\varepsilon_{n,\mathbf{k}})\frac{(\mathbf{v}_{n,\mathbf{k}}+\mathbf{v}_{m,\mathbf{k}}).\mathbf{q}}{2}\frac{\langle n,\mathbf{k}|\hat{J}_a(\mathbf{k})|m,\mathbf{k}\rangle\langle m,\mathbf{k}|\hat{J}_b(\mathbf{k})|n,\mathbf{k}\rangle}{(\varepsilon_{n,\mathbf{k}}-\varepsilon_{m,\mathbf{k}})^2}$$

$$= ie^2 \sum_{n,k} f(\varepsilon_{n,\mathbf{k}})\frac{(\mathbf{v}_{n,\mathbf{k}}+\mathbf{v}_{m,\mathbf{k}}).\mathbf{q}}{2}(\mathbf{\Omega}_n(\mathbf{k}))_c \tag{A.3}$$

Calculation of Π_3 is rather complicated, and in order to get a closed form, we assume that the model has only two bands. After a rather lengthy calculation we get :

$$(\Pi_3)^{ant} = ie^2 \sum_{n,k} f(\varepsilon_{n,\mathbf{k}})|\mathbf{q}|\Big[(\mathbf{v}_{+,\mathbf{k}}+\mathbf{v}_{-,\mathbf{k}})_a(\mathbf{\Omega}_n(\mathbf{k}))_a + (\mathbf{v}_{+,\mathbf{k}}+\mathbf{v}_{-,\mathbf{k}})_b(\mathbf{\Omega}_n(\mathbf{k}))_b\Big] \tag{A.4}$$

Finally for Π_4 we have (after expanding the matrix elements and simplifying):

$$(\Pi_4)^{ant} = ie^2 \sum_{n,k} f'(\varepsilon_{n,\mathbf{k}})|\mathbf{q}|\Big[(\mathbf{v}_{n,\mathbf{k}})_a(\mathbf{m}_n(\mathbf{k}))_a + (\mathbf{v}_{n,\mathbf{k}})_b(\mathbf{m}_n(\mathbf{k}))_b\Big] \tag{A.5}$$

After putting everything together and changing the sum into an integral we get :

$$\sigma_{ch} = \lim_{q\to 0} \epsilon_{abc} \frac{1}{2iq} \lim_{\omega\to 0} (\Pi^R_{ab}(\mathbf{q},\omega))^{ant} = -e \sum_n \int_{BZ} \frac{d\mathbf{k}}{(2\pi)^3} (\mathbf{v}_{n,\mathbf{k}}.\mathbf{m}_n(\mathbf{k})) f'(\varepsilon_n(\mathbf{k}),t)$$

$$+ e^2 \sum_{n=\pm} \int_{BZ} \frac{d\mathbf{k}}{(2\pi)^3} (\frac{\mathbf{v}_{-,\mathbf{k}} + \mathbf{v}_{+,\mathbf{k}}}{2}).\mathbf{\Omega}_{n,\mathbf{k}} f(\varepsilon_n(\mathbf{k}),t). \tag{A.6}$$

After partial integrating becomes Equation(2.22). Note that because of the assumptions made in calculating Π_2 and Π_3 this result is only valid for a two-band model.

A.2 Universal vanishing of the Hopf term

To prove that Equation (2.46) is really a topological invariant we consider the effect of changing the Hamiltonian from $\hat{H}(\mathbf{k})$ to $\hat{H}(\mathbf{k})+\delta\hat{h}$. For small enough $\delta\hat{h}$ we have:

$$G^{-1}(\widetilde{\mathbf{k}}) \to G^{-1}(\widetilde{\mathbf{k}}) + \delta\hat{h} \tag{A.7}$$

$$G(\widetilde{\mathbf{k}}) \to G(\widetilde{\mathbf{k}}) - G(\widetilde{\mathbf{k}})\delta\hat{h}G(\widetilde{\mathbf{k}})$$

From here on for simplicity we drop $\widetilde{\mathbf{k}}$ from our expressions. Applying the identities above we find the change in $\Pi_{a,b}(\mathbf{q},\omega)$:

$$\delta\Pi_{a,b}(\mathbf{q},\omega) = e^2\frac{q}{6}\sum_{a,b,c}\varepsilon_{a,b,c}\int_{-\infty}^{\infty}\frac{d\omega}{2\pi}\int_{BZ}\frac{d^3k}{(2\pi)^3}Tr\Big\{\big[\delta\hat{h}G\partial_{k_a}G^{-1}G\partial_{k_b}G^{-1}G\partial_{k_c}G^{-1}G\big]+ \tag{A.8}$$

$$\big[\delta\hat{h}\partial_{k_a}(G\partial_{k_b}G^{-1}G\partial_{k_c}G^{-1}G)\big]\Big\} = e^2\frac{q}{6}\sum_{a,b,c}\varepsilon_{a,b,c}\int_{-\infty}^{\infty}\frac{d\omega}{2\pi}\int_{BZ}\frac{d^3k}{(2\pi)^3}$$

$$Tr\Big\{\big[\delta\hat{h}\partial_{k_a}G\partial_{k_b}G^{-1}\partial_{k_c}G\big] - \big[\delta\hat{h}\partial_{k_a}(\partial_{k_b}G\partial_{k_c}G^{-1}G)\big]\Big\}$$

$$= e^2\frac{q}{6}\sum_{a,b,c}\varepsilon_{a,b,c}\int_{-\infty}^{\infty}\frac{d\omega}{2\pi}\int_{BZ}\frac{d^3k}{(2\pi)^3}Tr\Big\{\big[\delta\hat{h}\partial_{k_a}G\partial_{k_b}G^{-1}\partial_{k_c}G\big] - \big[\delta\hat{h}\partial_{k_b}G\partial_{k_c}G^{-1}\partial_{k_a}G\big]\Big\}$$

$$= e^2\frac{q}{6}\sum_{a,b,c}\varepsilon_{a,b,c}\int_{-\infty}^{\infty}\frac{d\omega}{2\pi}\int_{BZ}\frac{d^3k}{(2\pi)^3}Tr\Big\{\big[\delta\hat{h}\partial_{k_a}G\partial_{k_b}G^{-1}\partial_{k_c}G\big] - \big[\delta\hat{h}\partial_{k_a}G\partial_{k_b}G^{-1}\partial_{k_c}G\big]\Big\}$$

$$= 0,$$

where we have used cyclic properties of the trace, partial integrating and also the fact that any symmetric term inside the trace vanishes since the total answer is antisymmetric. Having established that $\Pi_{a,b}(\mathbf{q},\omega)$ is a constant, we show that its zero. Note that, if all Greens function's have finite imaginary parts in their poles (as they do in the disordered case) , then the momentum integral includes no singularities and is therefore analytic. This means that we can continuously deform our Hamiltonian, into a constant and force $\Pi_{a,b}(\mathbf{q},\omega)$ to vanish but since we already proved that $\Pi_{a,b}(\mathbf{q},\omega)$ is a constant under continuous deformations of the hamiltonian it follows that $\Pi_{a,b}(\mathbf{q},\omega)$ has to be zero everywhere (as long as there are no real poles). Note that in the clean case this proof doesn't go through since the Green function's poles are therefore real and the integrals are not analytic.

Appendix B: Appendix to Chapter 3

B.1 Effective spin model parameters

We start by calculating the first term in Eq.(10), we can graphically represent this term as,

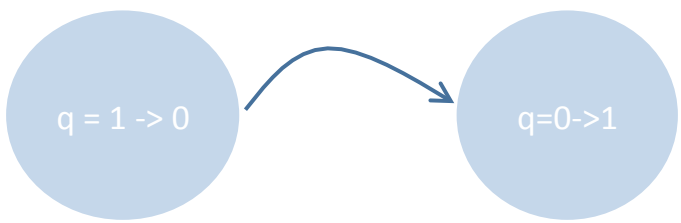

Figure B.1: $\sigma_i^- \sigma_{i+1}^+$ term as a first order process in the perturbation theory. q is the fractional charge modulo three.

Algebraically we can write,

$$\alpha_0 = \langle 1|e^{i\tilde{\varphi}(L/2)}|0\rangle\langle 0|e^{-i\tilde{\varphi}(0)}|1\rangle e^{-i\pi/3}. \tag{B.1}$$

The second term in Eq.(10) can be represented with four different diagrams corresponding to parameters $\alpha_1, \beta, \gamma, \lambda$. For α_1 we have the following Figure,

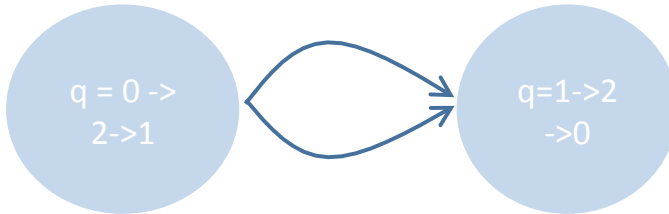

Figure B.2: $\sigma_i^+\sigma_{i+1}^-$ term as a second order process in perturbation theory. q is the fractional charge modulo three.

Note that this term also breaks conservation of fractional charge and therefore is only allowed at nonzero Δ. In algebraic form we have,

$$\alpha_1 = e^{2i\pi/3}\sum_{j,j'}\frac{\langle 1|e^{-i\tilde{\varphi}(L/2)}|2^{(j)}\rangle\langle 2^{(j)}|e^{-i\tilde{\varphi}(L/2)}|0\rangle}{E(2^{(j)})+E(2^{(j')})} \tag{B.2}$$
$$\times\langle 0|e^{i\tilde{\varphi}(0)}|2^{(j')}\rangle\langle 2^{(j')}|e^{i\tilde{\varphi}(0)}|1\rangle$$

where $|2^{(j)}\rangle$ corresponds to the j'th state (arbitrary ordering) with $q = 2$, and the energy E is the bare $\Delta = 0$ energy of the state with respect to the ground state energy. For β we have one of the diagrams shown below.

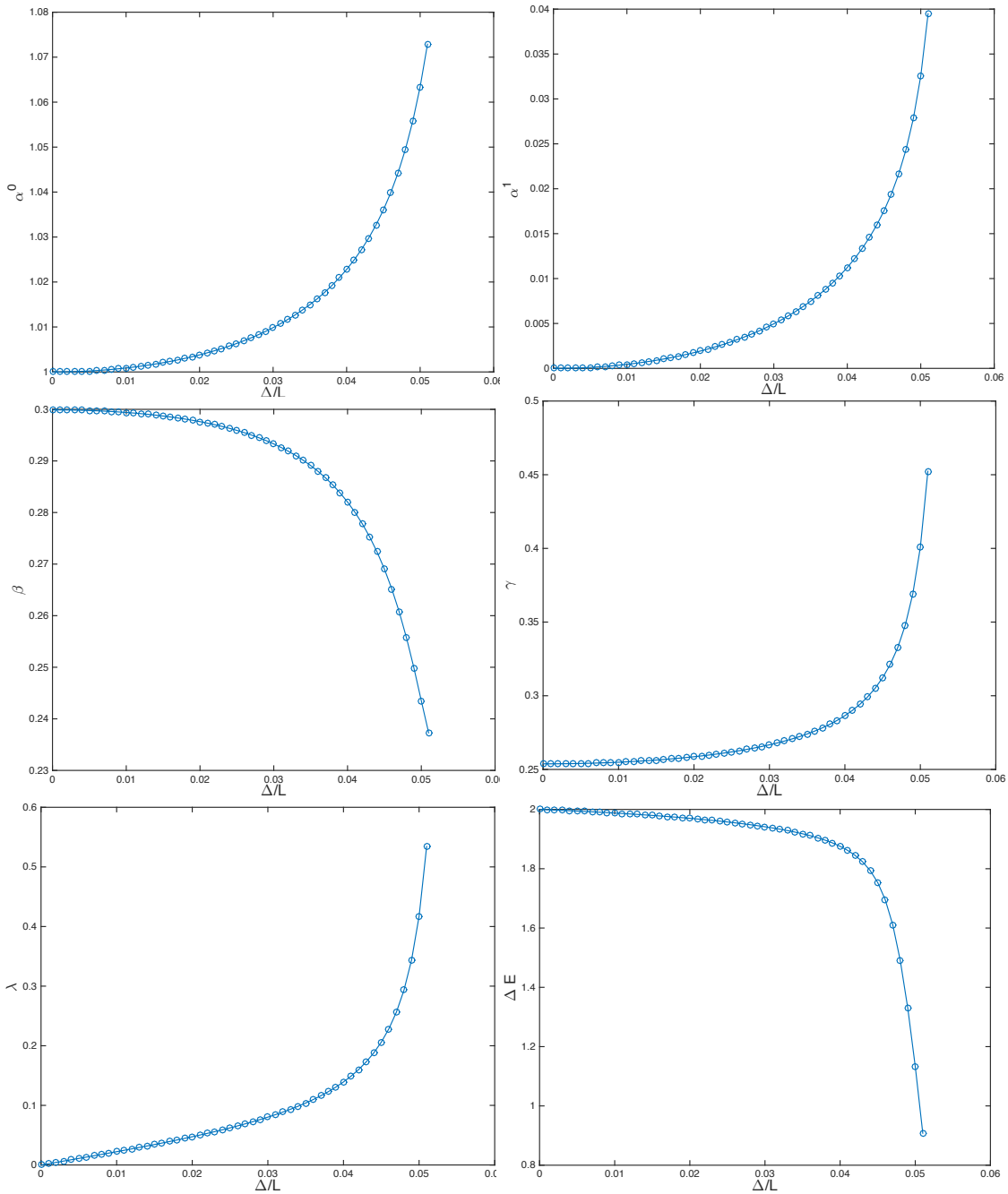

Figure B.3: Parameters $\alpha_0, \alpha_1, \beta, \gamma, \lambda, \Delta E$, as functions of Δ. We assume "pseudo point-like" superconductivity with $K_{max} = 4$ and $m_\mu = \frac{u\pi\nu}{L} = 1$.

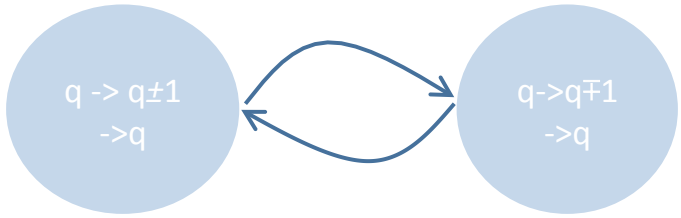

Figure B.4: $\sigma_i^z \sigma_{i+1}^z$ term as a second order process in perturbation theory. q is the fractional charge modulo three.

Using $\mathbb{Z}_2$ symmetry we can write

$$\beta = \sum_{j,j'} \frac{\langle 1|e^{-i\tilde{\varphi}(L/2)}|2^{(j)}\rangle\langle 2^{(j)}|e^{i\tilde{\varphi}(L/2)}|1\rangle}{E(2^{(j)}) + E(0^{(j')})} \tag{B.3}$$

$$\times \langle 1|e^{i\tilde{\varphi}(0)}|0^{(j')}\rangle\langle 0^{(j')}|e^{-i\tilde{\varphi}(0)}|1\rangle + \langle 1|e^{-i\tilde{\varphi}(0)}|2^{(j')}\rangle\langle 2^{(j')}|e^{i\tilde{\varphi}(0)}|1\rangle$$

$$\times \frac{\langle 1|e^{i\tilde{\varphi}(L/2)}|0^{(j)}\rangle\langle 0^{(j)}|e^{-i\tilde{\varphi}(L/2)}|1\rangle}{E(2^{(j')}) + E(0^{(j)})},$$

where $|2^{(j)}\rangle, |0^{(j)}\rangle$ correspond to all excited states with $q = 0, 2$. The diagram corresponding to γ term is shown below.

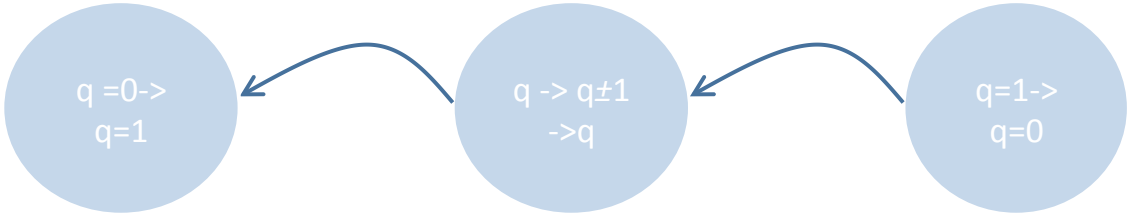

Figure B.5: $\sigma_{i-1}^+ \sigma_{i+1}^-$ term as a second-order process in perturbation theory. q is the fractional charge modulo three.

We have

$$\gamma = 2\alpha_0 e^{-i\pi/3} \sum_j \Big(\frac{\langle 0|e^{-i\tilde{\varphi}(0)}|1^{(j)}\rangle\langle 1^{(j)}|e^{i\tilde{\varphi}(L/2)}|0\rangle}{E(1^{(j)})} - \frac{e^{-i\pi/3}\langle 0|e^{i\tilde{\varphi}(L/2)}|2^{(j)}\rangle\langle 2^{(j)}|e^{-i\tilde{\varphi}(0)}|0\rangle}{E(2^{(j)})} \Big). \tag{B.4}$$

For the λ term, corresponding diagram is given in Fig.3. The algebraic form of λ is,

$$\lambda = \langle 0|e^{-i\tilde{\varphi}(L/2)}|1\rangle\langle 0|e^{-i\tilde{\varphi}(0)}|1\rangle \sum_j \Big(\frac{e^{-4i\pi/3}}{E(2^{(j)})} \times \langle 0|e^{i\tilde{\varphi}(L/2)}|2^{(j)}\rangle\langle 2^{(j)}|e^{i\tilde{\varphi}(0)}|1\rangle + \frac{e^{-2i\pi/3}}{E(2^{(j)})} \times \langle 0|e^{i\tilde{\varphi}(0)}|2^{(j)}\rangle\langle 2^{(j)}|e^{i\tilde{\varphi}(L/2)}|1\rangle \Big). \tag{B.5}$$

In Fig B.3 we provide a plot of parameters $\alpha_0, \alpha_1, \beta, \gamma, \lambda, \Delta E$ (ΔE is the energy gap) as function of Δ. We work with "pseudo point-like" superconductivity with $K_{max} = 4$ and $m_\mu = \frac{u\pi\nu}{L} = 1$.

B.2 Numerical results for the disordered system

In this section we discuss how random fluctuations in different loop lengths change our results.

Changing the loop length changes the effective model parameters $\alpha_1, \beta, \gamma, \lambda$ by changing the energy denominator used in their perturbative expansion. Since the energy of a single loop depends on length as $1/L$, the effect of random fluctuations in loop length for small length fluctuations $\Delta L/L$ can be loosely incorporated by multiplying each one of the parameters $\alpha_1, \beta, \gamma, \lambda$ at each site by $1 + \frac{\Delta L}{L}$ where ΔL is a site and parameter dependent random number chosen from a uniform distribution

in the range $-rL \leq \Delta L \leq rL$, where is r a dimensionless number characterizing disorder strength. We call r the "relative error size" in this section.

In the following Table we have provided sample numerical results for our system at different chain lengths and also with different relative error sizes. Throughout this section we have set $t = 1$, $\Delta/L = 0.046$ and momentum cutoff $K_{max} = 4$. This results clearly show that our results (existence of a topological three fold degeneracy) are robust to signficant disorder strength $r \approx 0.3$.

Table B.1: DMRG calculation results for "pseudo point-like" superconductivity(defined earlier) at $t = 1$, $\Delta/L = 0.046$ and momentum cutoff $K_{max} = 4$

Chain length	Relative error size	Ground state energy	1st excited energy state	2nd excited energy state	3rd excited energy state
10	0	-6.818	-6.696	-6.696	-6.149
10	0.1	-6.840	-6.725	-6.725	-6.183
10	0.2	-6.876	-6.731	-6.731	-6.193
10	0.3	-6.838	-6.709	-6.709	-6.152
40	0	-29.681	-29.677	-29.677	-29.384
40	0.1	-29.629	-29.625	-29.625	-29.331
40	0.2	-29.480	-29.476	-29.476	-29.194
40	0.3	-29.942	-29.937	-29.937	-29.656
100	0	-75.524	-75.524	-75.524	-75.267
100	0.1	-75.472	-75.472	-75.472	-75.212
100	0.2	-75.506	-75.506	-75.506	-75.255
100	0.3	-76.387	-76.387	-76.387	-76.123

B.3 Three-fold degeneracy in the arge Δ regime for point-like superconductivity

B.3.1 I. Diagonalizing the Hamiltonian in the limit $\Delta \to \infty$

We study the Hamiltonian $H = H_{edge} + H_{sc}$ in the limit of strong and point-like superconductivity. Note that the Hamiltonian commutes with the operator $T = e^{-i\pi\nu\hat{n}}$, $[H, T] = 0$. Eigenvalues of T can be shifted by a unitary transformation $e^{i\hat{\varphi}_0}$ as can be seen from the commutation relation $Te^{iq\hat{\varphi}_0} = e^{iq\hat{\varphi}_0}Te^{-iq\pi\nu}$, i.e. if we define $H_{q=0}$ as the Hamiltonian H in the charge sector $q = 0$, other charge eigenvalues q can be generated from the transformed Hamiltonian,

$$H_q(m_\mu) = e^{-iq\hat{\varphi}_0} H_{q=0}(m_\mu + q) e^{iq\hat{\varphi}_0}. \tag{B.6}$$

We emphasize that $H_{q=0}$ is defined in the Hilbert space where the wavefunctions are eigenstates of T with eigenvalue 1 which in turn implies that the wavefunctions are periodic under the translation $\varphi_0 \to \varphi_0 + \pi\nu$ (i.e. allowed charges are multiples of three).

In the range of periodicity of the wave-functions, the potential H_{sc} has a single minimum. In the limit of large Δ, H_{sc} we can expand around this minimum to obtain the harmonic approximation of H_{sc},

$$H_{sc} \sim \Delta(1 - \frac{9}{2}\varphi^2(0)). \tag{B.7}$$

Note that the continuous nature of the harmonic approximation means that wave-functions would in general violate the periodicity condition as we change $\varphi_0 \to$

$\varphi_0+\pi\nu$. However, this boundary condition is expected to be irrelevant for calculating ground state energies in the large delta regime, where φ_0 becomes strongly localized around zero. In the next section, we'll use an instanton approximation to see how enforcing periodic boundary conditions modifies our results.

Within the harmonic approximation $H_{q=0}$ can be turned into a set of decoupled harmonic oscillators with trivial spectrum. A particularly nice feature of this transformation is that the spectrum of H_q will not depend on q (i.e. the spectrum of $H_{q=0}$ will not depend on m_μ). Degeneracy of the three charge sectors in the large Δ regime follows from this. We'll now show this by explicitly diagonalizing the Hamiltonian.

To diagonalize the Hamiltonian, it is useful to define the following generalized "position" and "momentum" operators,

$$\hat{\beta}_k \equiv i\sqrt{\frac{L}{2u\pi k}}\left(\hat{a}_k - \hat{a}_k^\dagger\right) \quad ; \quad \hat{\alpha}_k \equiv \sqrt{\frac{u\pi k}{2L}}\left(\hat{a}_k + \hat{a}_k^\dagger\right) \tag{B.8}$$

These operators satisfy,

$$[\hat{\beta}_k, \hat{\alpha}_{k'}] = i\delta_{kk'} \quad ; \quad [\hat{\beta}_k, \hat{\beta}_{k'}] = [\hat{\alpha}_k, \hat{\alpha}_{k'}] = 0. \tag{B.9}$$

In these variables and within harmonic approximation $H_{q=0}$ becomes (ignoring the constants),

$$H_{q=0,h} = \hat{\mathrm{X}}^{\mathrm{T}} H_{\mathrm{X}} \hat{\mathrm{X}} + \hat{\mathrm{P}}^{\mathrm{T}}\hat{\mathrm{P}} \qquad \text{with,}$$
$$\hat{\mathrm{X}} \equiv \left(\sqrt{\frac{L}{u\pi\nu}}\hat{\varphi}_0, \hat{\beta}\right); \hat{\mathrm{P}} \equiv \left(\sqrt{\frac{u\pi\nu}{L}}(\hat{n} - m_\mu), \hat{\alpha}\right), \tag{B.10}$$

where(setting $m_\mu = 1$),

$$H_{\mathrm{X}} = \frac{9u\Delta\pi\nu}{2L}\begin{pmatrix} 1 & 1/\sqrt{2} \\ 1/\sqrt{2} & 1+\frac{2u\pi k^2}{9L\Delta\nu}\delta_{k,k'} \end{pmatrix} \tag{B.11}$$

Note that since the commutator $[\hat{\varphi}_0, \hat{n} - m_\mu] = i$ is independent of m_μ, the spectrum of $H_{q=0,h}$ does not depend on m_μ. In turn this implies that the spectrum of H_q does not depend on q.

In its diagonal form this Hamiltonian describes a set of decoupled harmonic oscillators with different frequencies. In Fig. B.6 we have plotted the energy gap δ_0 as a function of Δ.

This completes our discussion of the spectrum within harmonic approximation.

As a measure of validity for our approximation, we calculate the expectation value of $\langle\varphi^2(0)\rangle_0$. As shown in Fig. B.7, we find that the fluctuations are monotonically decreasing function of the coupling strength Δ. In other words, one can always choose the value of Δ to be large enough to get phase fluctuations in $\varphi(0)$ to be much smaller than 2π which justifies the use of harmonic approximation.

B.3.2 II. Finite Δ corrections to ground state energies

As mentioned earlier the wave functions found within harmonic approximation violate the periodicity condition as we change $\varphi_0 \to \varphi_0 + \pi\nu$. In this section we use an instanton approximation to see how this periodicity changes our previous results.

We'll enforce periodicity by externally projecting the states into the physical

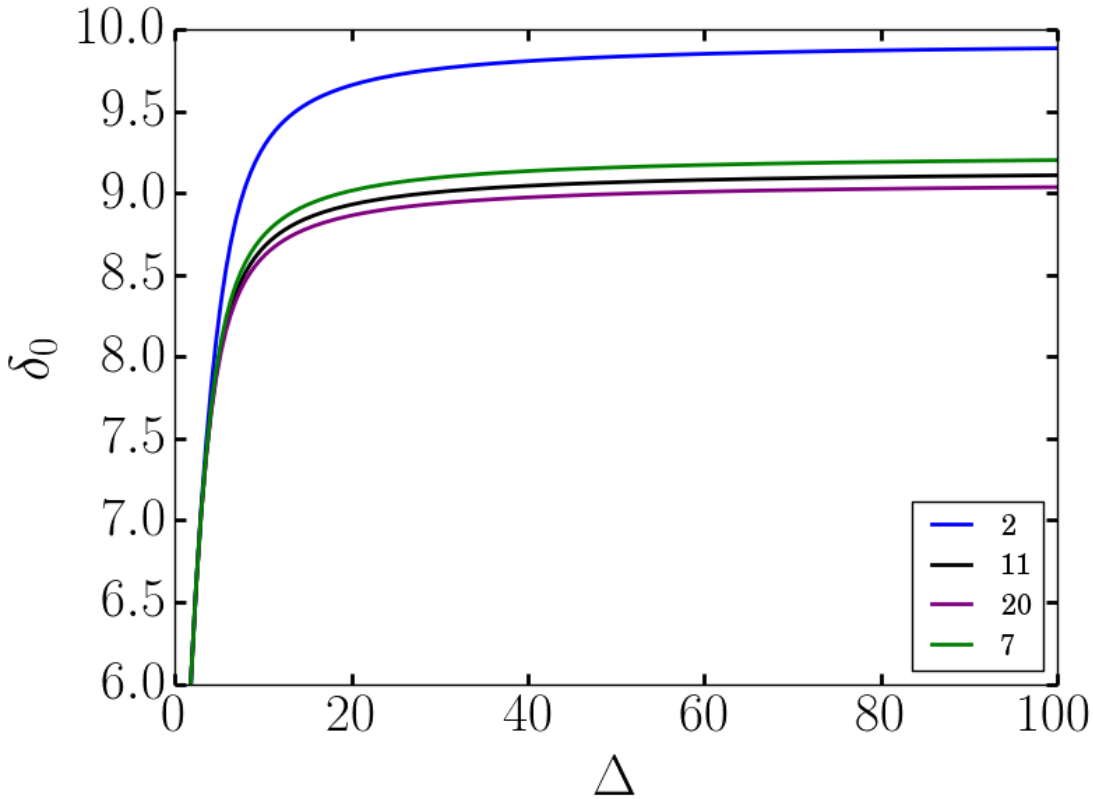

Figure B.6: Plot of the energy gap δ_0 as a function of Δ for various total number of modes K_{max} shown in the legend. Here numerical values of m_μ, u and L are set to one.

Hilbert space,

$$|q=0\rangle = \mathcal{P}|q=0\rangle_h, \tag{B.12}$$

where $|q=0\rangle_h$ is the $q=0$ eigenstate within the harmonic approximation and $\mathcal{P}$ is an operator that projects into the sector that obeys the periodicity condition as $\varphi_0 \to \varphi_0 + \pi\nu$. We then calculate the q and Δ dependence of ground-state energy

using,

$$
\begin{aligned}
E_q &= \langle q|H|q\rangle / \langle q|q\rangle \\
&= \frac{\sum_{m\in\mathbb{Z}} e^{-i\pi\nu q m} N(m)}{\sum_{m\in\mathbb{Z}} e^{-i\pi\nu q m} D(m)},
\end{aligned}
\tag{B.13}
$$

where $N(m) = N_1(m) + N_2(m) + N_3(m) + N_4(m)$ with the definitions,

$$
\begin{aligned}
N_1(m) &= \left(\sum_p (\lambda_+^{0n})^2 - \left(\pi\nu m \sum_p (\lambda_+^{0n})^2 \right)^2 \right) \prod_n e^{-(\frac{1}{2}h_{nm})^2} \\
N_2(m) &= -\prod_n e^{-(\frac{1}{2}h_{nm})^2} \left(\sum_k \frac{2\pi u k}{L} \left(\sum_n (\lambda_-^{kn})^2 \right.\right. \\
&\quad \left.\left. + \ (\pi\nu m)^2 \left(\sum_p \lambda_+^{kp} \lambda_+^{0p} \right) \left(\sum_q \lambda_-^{kq} \lambda_+^{0q} \right) \right) \right) \\
N_3(m) &= \left(\sum_k \frac{u\pi k}{L} \right) \prod_n e^{-(\frac{1}{2}h_{nm})^2} \\
N_4(m) &= \frac{9\Delta}{2} \left(\prod_n e^{-\frac{1}{2}\left(h_{nm}^2 - f_n^2\right) - h_{nm} f_n} \right. \\
&\quad \left. + \prod_n e^{-\frac{1}{2}\left(h_{nm}^2 - f_n^2\right) + h_{nm} f_n} \right) \\
D(m) &= \prod_n e^{-(\frac{1}{2}h_{nm})^2},
\end{aligned}
\tag{B.14}
$$

with,

$$
\begin{aligned}
f_n &= \frac{2}{\nu} \left(\sum_k \sqrt{\frac{\nu}{k}} (\lambda_-^{kn} + \lambda_+^{kn}) + \lambda_-^{0n} \right) \\
h_{nm} &= \pi\nu m \lambda_+^{0n} \\
\lambda_+^{0n} &= \frac{1}{2} \sqrt{\frac{L}{u\pi\nu}} U_{0n}^\dagger \sqrt{\omega_n} \\
\lambda_-^{0n} &= i \sqrt{\frac{u\pi\nu}{L}} U_{0n} \frac{1}{\sqrt{\omega_n}} \\
\lambda_+^{kn} &= \frac{i}{2} \sqrt{\frac{L}{2\pi u k}} U_{kn}^\dagger \sqrt{\omega_n} + \frac{i}{2} \sqrt{\frac{2\pi u k}{L}} U_{kn} \frac{1}{\sqrt{\omega_n}} \\
\lambda_-^{kn} &= -\frac{i}{2} \sqrt{\frac{L}{2\pi u k}} U_{kn}^\dagger \sqrt{\omega_n} + \frac{i}{2} \sqrt{\frac{2\pi u k}{L}} U_{kn} \frac{1}{\sqrt{\omega_n}}
\end{aligned}
\tag{B.15}
$$

where, U_{mn} and ω_n are the matrix element of unitary matrix U, diagonalizing H_X and the nth eigenvalue of H_h, respectively (see Eq. (B.10)).

Sample results of this calculation are shown in Fig. B.8. This results can be used as an estimate for the value of the parameter h in the clock model Hamiltonian.

B.3.3 III. Quasiparticle matrix elements

Let us consider quasiparticle tunneling elements between the ground states ,

$$M^q(x) = \langle q+1|e^{i\varphi(x)}|q\rangle. \tag{B.16}$$

In terms of states in the harmonic approximation,

$$M^q(x) = \langle q+1|_h \mathcal{P}^\dagger e^{-i(q+1)\hat{\varphi}_0} e^{i\varphi(x)} e^{iq\hat{\varphi}_0} \mathcal{P}|q\rangle_h. \tag{B.17}$$

Setting $m_\mu = 1$ and substituting $\mathcal{P} = \mathcal{N}\sum_m e^{i\pi\nu m\hat{n}}$ ($\mathcal{N}$ being the normalization constant) in the harmonic approximation for $|q\rangle = e^{-iq\hat{\varphi}_0}|0\rangle$, we get,

$$\begin{aligned} M^q &= \mathcal{N}^2 \sum_{p,m\in\mathbb{Z}} e^{i\pi\nu(p-m)(q+1)} \langle 0|e^{i\pi\nu\hat{n}(m-p)} e^{i\varphi(x)}|0\rangle \\ &\equiv \sum_{m\in\mathbb{Z}} M^q_m \end{aligned} \tag{B.18}$$

with,

$$\begin{aligned} M^q_m &= e^{i\pi\nu m(q+1)} \langle 0|e^{-i\pi\nu m\hat{n}} e^{i\varphi(x)}|0\rangle = e^{i\pi\nu m(q+1/2)} \\ &\times \langle 0|e^{i(\hat{\varphi}_0 + \pi\nu(2x/L-m)\hat{n} + i\sum_k \sqrt{\frac{\nu}{k}}(\hat{a}_k e^{i\frac{2\pi kx}{L}} - \hat{a}^\dagger_k e^{-i\frac{2\pi kx}{L}})}|0\rangle \end{aligned} \tag{B.19}$$

This explicit form makes clear the following identity,

$$\begin{aligned} M^q_{m+2}(x+L) &= e^{i\pi\nu m(2q+1)} M^q_m(x) \\ \implies M^q(x+L) &= e^{i\pi\nu m(2q+1)} M^q(x) \end{aligned} \tag{B.20}$$

Using the expressions,

$$\hat{a}_k^\dagger = \sum_n (\lambda_+^{kn} A_n^\dagger + \lambda_-^{kn} A_n)$$

$$\hat{a}_k = -\sum_n (\lambda_-^{kn} A_n^\dagger + \lambda_+^{kn} A_n)$$

$$\hat{\tilde{n}}_{q=0} = \sqrt{\frac{L}{\pi\nu u}} \frac{-i}{2} \sum_n U_{0n}^\dagger \sqrt{\omega_n} (A_n - A_n^\dagger)$$

$$\hat{\varphi}_0 = \sqrt{\frac{\pi\nu u}{L}} \sum_n U_{0n} \frac{1}{\sqrt{\omega_n}} (A_n + A_n^\dagger), \tag{B.21}$$

where A_n is the nth component of the operator valued vector $A \equiv \frac{1}{\sqrt{2}} \left(\hat{\mathrm{X}} + i\hat{\mathrm{P}}\right)$, M_m^q can be expressed as,

$$M_m^q = e^{i\pi\nu m q} \prod_n e^{-\frac{1}{2}|\eta_n^m(x)|^2} \langle 0| e^{-\eta_n^{m*} A_n^\dagger} e^{\eta_n^m A_n} |0\rangle \tag{B.22}$$

with,

$$\eta_n^m(x) = \left(2\pi\nu \frac{x}{L} - \pi\nu m\right) \frac{1}{2} \sqrt{\frac{L}{\pi\nu u}} U_{0n}^\dagger \sqrt{\omega_n}$$
$$+ i\sqrt{\frac{\pi\nu u}{L}} U_{0n} \sqrt{\frac{1}{\omega_n}} + \sum_k \sqrt{\frac{\nu}{k}} (\lambda_+^{kn} e^{-i2\pi kx/L} + \lambda_-^{kn} e^{i2\pi kx/L}). \tag{B.23}$$

We use this expression to calculate $|M^q|$ as a function of number of modes and coupling strength, Δ. Since $|M^{q=1}| = |M^{q=2}|$, we plot the results for $|M^{q=0}|$ and $|M^{q=1}|$. The results are shown in Figs. B.9 and B.10.

These results can be used to calculate the parameter $A(x)$ in Eq.(13).

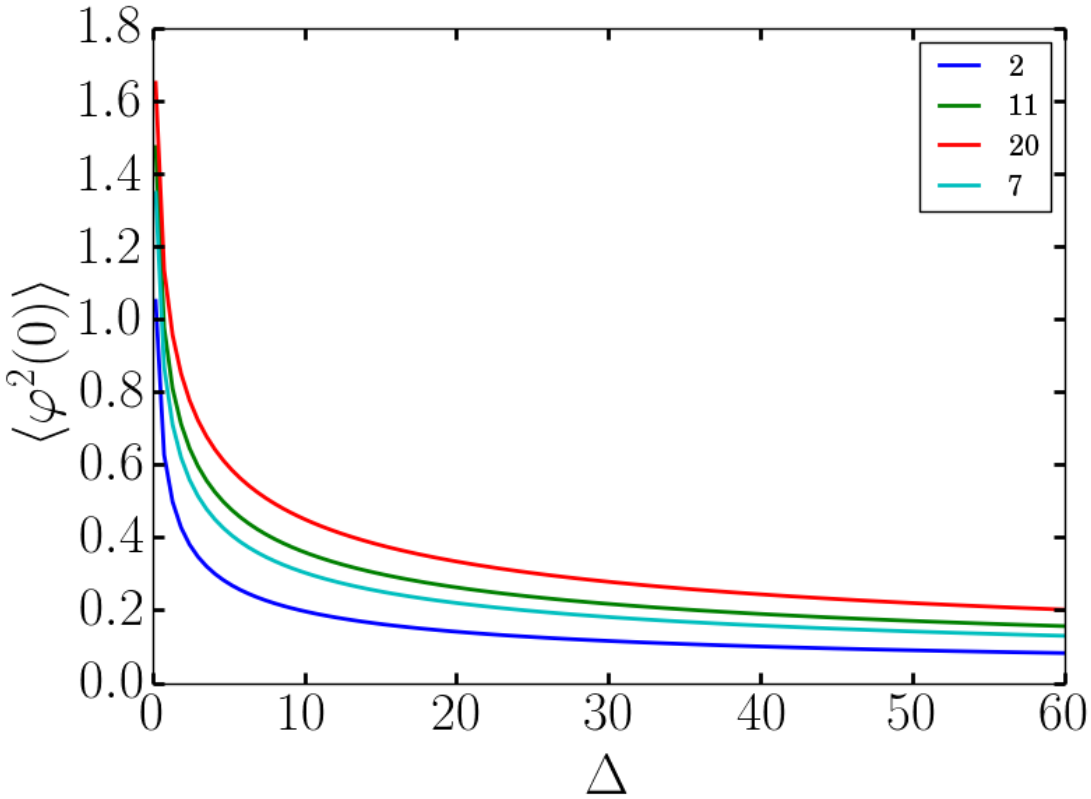

Figure B.7: $\langle\varphi^2(0)\rangle$ as a function of Δ for various total number of modes K_{max} shown in caption. We find $\varphi(0)$ is localized for large values of Δ. Therefore, for large enough value of Δ, harmonic approximation is justified. Here numerical values of m_μ, u and L are set to one for convenience.

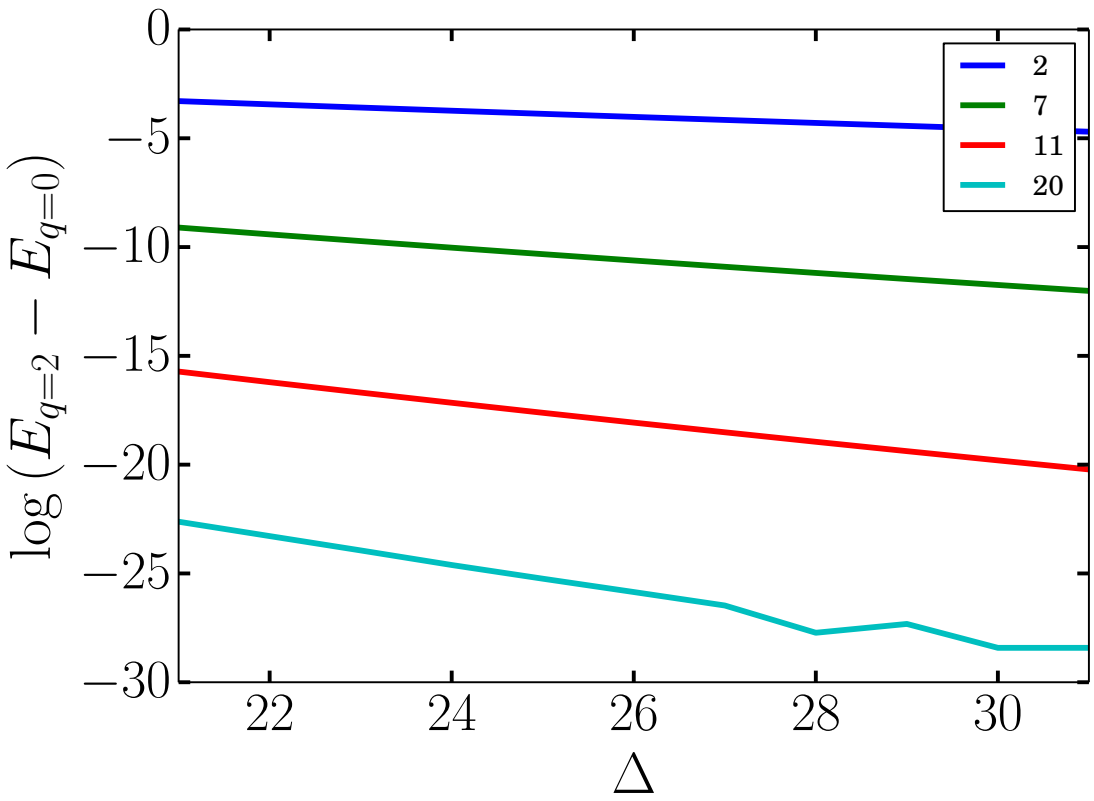

Figure B.8: Logarithm of ground-state energy splitting between charge sectors $q = 2$ and $q = 0, 1$ (they're degenerate) as a function of coupling strength Δ, for different total number of modes K_{max} shown in the inset. Notice that the energy splitting goes to zero at large Δ. Here numerical values of m_μ, u and L are set to one.

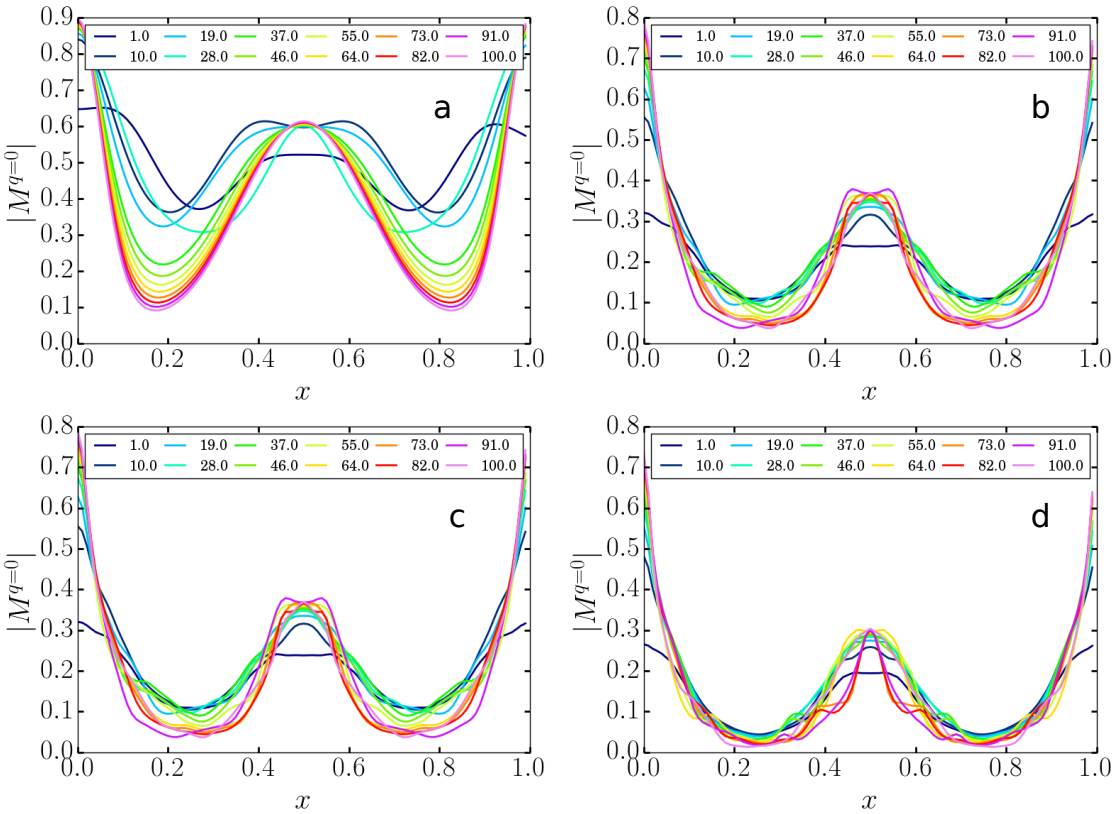

Figure B.9: Plot of absolute value of quasi-particle matrix element, $|M^{q=0}|$ as a function x (in the units of length L) for various coupling strength parameters, $\frac{4}{\nu^2}\Delta$, given in the legend. The total number of modes K_{max} are varied in (a-d) as 2,7,11 and 20, respectively. Here numerical values of m_μ, u and L are set to one.

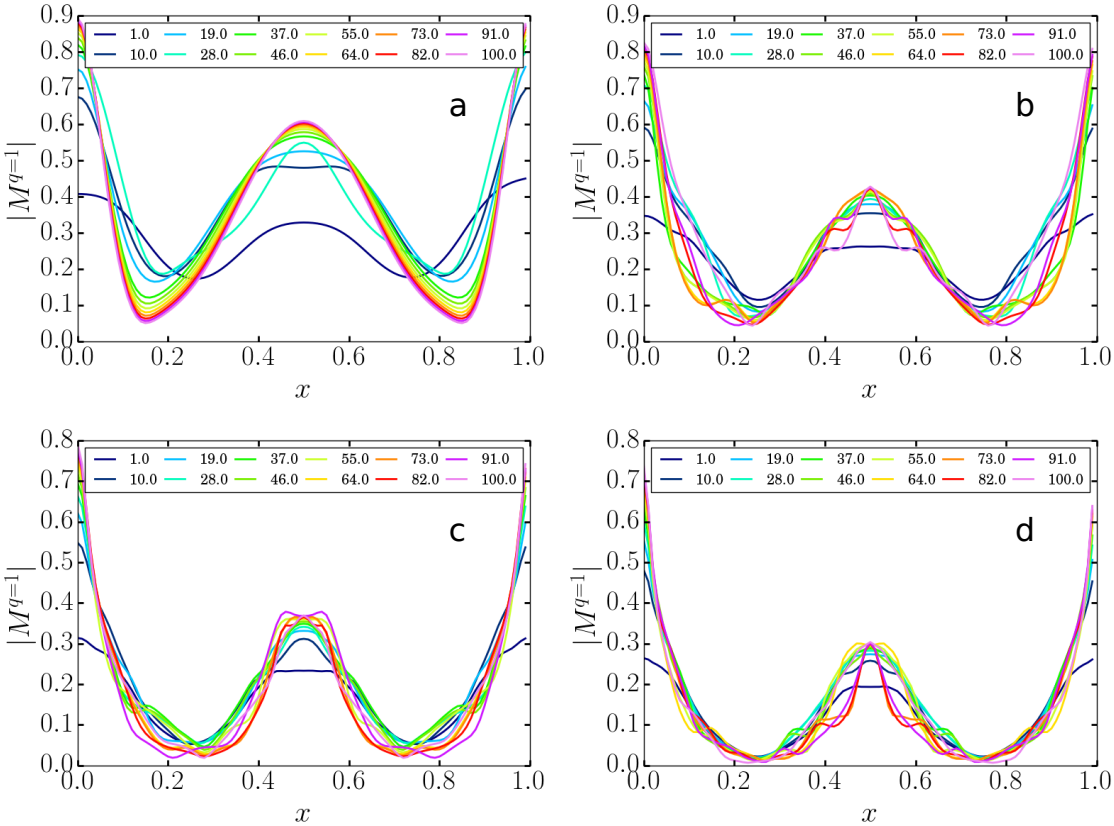

Figure B.10: Plot of absolute value of quasi-particle matrix element, $|M^{q=1}| = |M^{q=2}|$ as a function x (in the units of length L) for various coupling strength parameters, $\frac{4}{\nu^2}\Delta$, given in the legend. The total number of modes K_{max} are varied in (a-d) as 2,7,11 and 20, respectively. Here numerical values of m_μ, u and L are set to one.

Appendix C: Appendix to Chapter 4

C.1 Details on deriving I_{sc}

To calculate Eq. (4.6), we start with the defining differential equation $(i\omega_m - H)\, G(x, x'; i\omega_m) = \delta(x - x')$. We can explicitly re-write this as (assuming $0 < x < L$),

$$\Big(i\omega_m - \Big[\hbar v(x)(-i\tau_0\partial_x - a(x)\tau_z) + \Delta(x)\tau_x\Big]\Big)\, G(x, x'; i\omega_m) = \delta(x - x') \tag{C.1}$$

Where $v(x), a(x)$ and $\Delta(x)$ are as defined in Eq. (4.5). This equation can then be integrated around the QH edge but the delta function $\delta(x - x')$ to give,

$$\lim_{\varepsilon\to 0^+} G(x - \varepsilon, x; i\omega_m) = M(x)\left[\lim_{\varepsilon\to 0^+} G(x + \varepsilon, x; i\omega_m)\right]. \tag{C.2}$$

The explicit form of $M(x)$ is calculated by integrating Eq. (C.1) piecewise:

$$M(x) = e^{-2\frac{\omega_m}{\hbar}(\frac{L}{v_{\rm qh}} + \frac{W}{v_{\rm sc}})} e^{-i\phi\frac{x}{2L}\tau_z} e^{-i\frac{\Delta W}{\hbar v_{\rm sc}}\tau_x} e^{i\frac{\phi}{2}\tau_z} e^{-i\frac{\Delta W}{\hbar v_{\rm sc}}\tau_x} e^{-i\phi\frac{L-x}{2L}\tau_z}. \tag{C.3}$$

Note that using the properties of the $SU(2)$ group, $M(x)$ can be written as in Eq. (4.8) and becomes independent of x. Now, integrating the differential equation through the delta function from $x - \varepsilon$ to $x + \varepsilon$ gives Eq. (4.9),

$$\lim_{\varepsilon\to 0^+} \big[G(x + \varepsilon, x; i\omega_m) - G(x - \varepsilon, x; i\omega_m)\big] = -i/\hbar v_{\rm qh}. \tag{C.4}$$

Solving Eqs. (C.2), (C.4):

$$\lim_{\varepsilon\to 0^+} G(x+\varepsilon, x; i\omega_m) = -(1-M)^{-1}\frac{i}{\hbar v_{\rm qh}},$$
$$\lim_{\varepsilon\to 0^+} G(x-\varepsilon, x; i\omega_m) = -M(1-M)^{-1}\frac{i}{\hbar v_{\rm qh}}. \tag{C.5}$$

With our regularization scheme, we obtain the Green's function $G(x, x; i\omega_m)$:

$$G(x, x; i\omega_m) = \lim_{\varepsilon\to 0^+} \frac{G(x+\varepsilon, x; i\omega_n) + G(x-\varepsilon, x; i\omega_n)}{2} = -(1+M)(1-M)^{-1}\frac{i}{\hbar v_{\rm qh}}. \tag{C.6}$$

Now Eq. (4.6) can be calculated using Eq. (C.6).

$$\begin{aligned} I_{\rm sc} &= -\frac{e v_{\rm qh}}{\beta L}\sum_m \left[\int_0^L dx\, \mathrm{Tr}\Big[G(x,x;i\omega_m)\tau_z\Big] - \int_{L+W}^{2L+W} dx\, \mathrm{Tr}\Big[G(x,x;i\omega_m)\tau_z\Big]\right] \\ &= \frac{2e}{\beta\hbar}\sum_m \mathrm{ImTr}\Big[(1+M)(1-M)^{-1}\tau_z\Big] \\ &= \frac{4e}{\beta\hbar}\sum_m \mathrm{ImTr}\Big[(1-M)^{-1}\tau_z\Big] \end{aligned} \tag{C.7}$$

Using our expression for M in Eq. (C.3), and explicitly calculating the trace gives Eq.(4.10).

Appendix D: Appendix to Chapter 5

D.1 Formalism and Methods

Here, we introduce a simple formulation of the general idea of "flat-band ferromagnetism". We start with a heuristic discussion of ferromagnetism in the perfectly flat band limit. We then proceed to discuss the one-magnon excitation spectrum.

D.1.1 Ferromagnetism in the perfectly flat band limit

Consider a generic band system where the lowest occupied band is perfectly flat. We assume this band has an exact spin degeneracy. The flat band is spanned by a set of wave-functions, e.g. Bloch or Wannier wave-functions $\psi_m(x)$. We take the (N_e) particles in the lowest band to interact with a strictly contact, i.e. Hubbard, interaction,

$$H_{\text{int}} = U \sum_{i<j=1}^{N_e} \delta(r_i - r_j). \tag{D.1}$$

Note that since the band is flat, the kinetic energy term is irrelevant, i.e. constant. Therefore, to find the ground state of the system, we only need to consider the interaction term written above. Furthermore, note that the interaction term is non-negative $\langle H_{\text{int}} \rangle \geq 0$.

Consider now a generic flat band wave function,

$$\psi(x_1, x_2, ..., x_{N_e}) \times |\psi_{\text{spin}}\rangle, \tag{D.2}$$

where the two parts represent spatial and spin (flavor) part of the the total wave-function. To minimize the energy and find the ground state, we need to ensure that $\psi(x_1, x_2, ..., x_{N_e})$ vanishes when any two of coordinates are identical $x_i = x_j$. An easy (and perhaps the only generic) way to do this is to take the spatial wave wave-function $\psi(x_1, x_2, ..., x_{N_e})$ to be totally anti-symmetric. However, since the entire wave-function also has to be anti-symmetric. The spin part of the wave function $|\psi_{\text{spin}}\rangle$ has to be totally *symmetric*. It is then straightforward to show that all such wave-functions exhibit saturated ferromagnetism[1]. We emphasize that all this discussion also applies to lattice systems and is not restricted to the continuum.

An important theorem due to Mielke [116], shows that if the one-particle density matrix associated with the (Slater determinant) state discussed above is irreducible in real space, the saturated ferromagnetic states are the *unique* ground states (up to trivial spin degeneracy). Conversely, if the density matrix is reducible, there are additional ground states corresponding to different $SU(2)$ rotations of different blocks of the density matrix. It is straightforward to show that in this case, the lowest energy states in the one-magnon (single spin flip) spectrum would be at least twofold degenerate. Throughout this work, and by direct calculation, we have always ensured that the one-magnon spectrum is not degenerate. This puts additional context around the usefulness of the one-magnon spectrum as used in

[1]To see this, note that the permutation operator $\mathcal{P}_{ij}$ is related to the Heisenberg exchange operator.

this paper. The generality and the simplicity of this results makes it a powerful tool for studying nearly flat band ferromagnetism.

Traditionally, when short-range Hubbard interactions are considered, Mott insulating states are considered as candidate ground states. The idea is to restrict the electrons to sharply localized non-overlapping Wannier wave-functions to minimize the interaction energy. However, note that for non-isolated or isolated and topologically non-trivial bands, Wannier wave-functions are not even approximately localized. Therefore, in these cases (overlapping or topologically non-trivial band), Mott insulating states are not good ground state candidates, whereas the ferromagnetic states discussed above, are good candidates independent of the (topological-)nature of the underlying band.

We note that the argument above does not directly apply to the experimentally interesting case of TBLG. This is so because in that case there are additional subtleties caused by the extra degrees of freedom (valley, layer and sub-lattice) and the discrete symmetries associated with them (discussed in the main text).

D.1.2 The one-magnon spectrum and spin stiffness

For all $SU(2)$ invariant systems, eigenstates can be classified with total spin S_z. The ferromagnetic manifold is constrained by the total spin. For the flat band limit discussed above, the ferromagnetic states are also the lowest energy states. A low energy set of excitations above the ferromagnetic states would be the states with slightly lower spin-polarization are obtained by flipping a single spin, i.e. creating

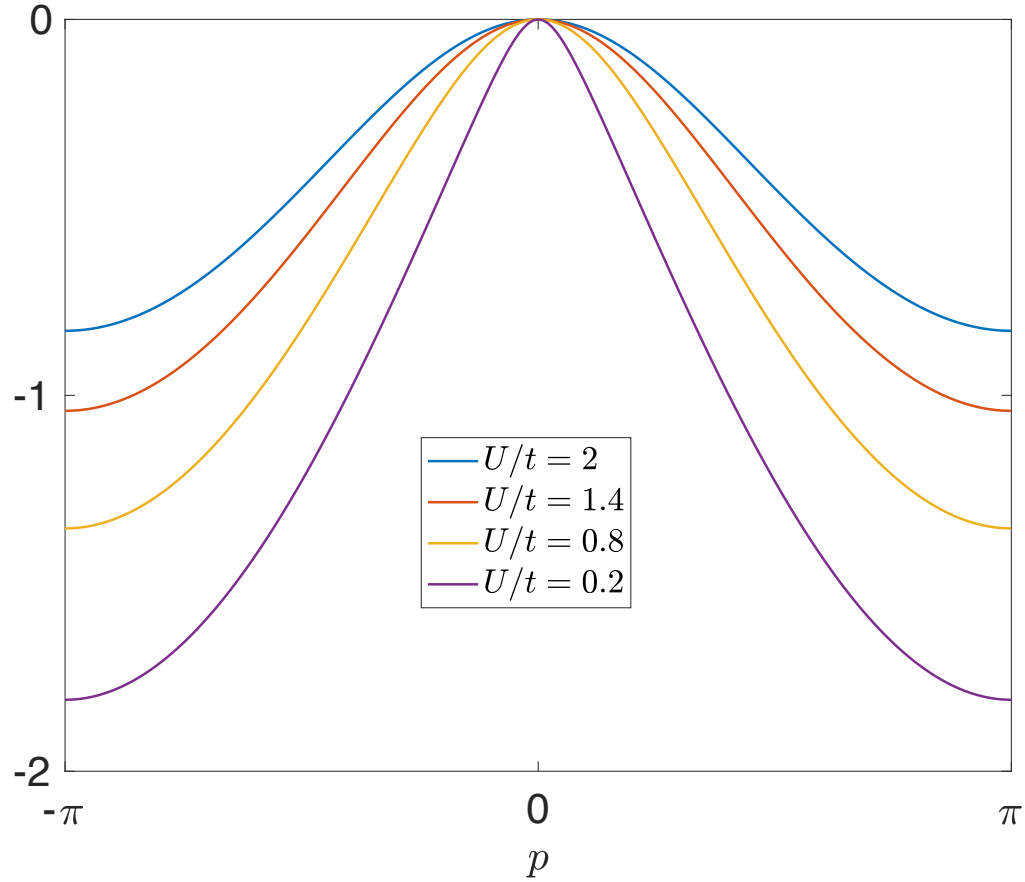

Figure D.1: Lowest one-magnon band energy for the one dimensional Hubbard model in Eq.(D.4).

one magnon. The wave-functions in this manifold can be constrained to be of the form,

$$|\psi^q\rangle = \sum_{p\in \mathrm{BZ}} \phi^q_p c^\dagger_{p+q,\downarrow} c_{p,\uparrow} |\uparrow \text{polarized}\rangle. \tag{D.3}$$

An identical relation also holds by changing $\uparrow\rightarrow\downarrow$ or by considering more general flavor degrees of freedom.

As the ferromagnetic state becomes unstable, the one-magnon band minimum shifts from $q = 0$ to a finite momentum state $q \neq 0$. It is then natural to consider a

scenario where magnons condense at the location of the new minima, giving rise to a new type of magnetic order at finite momenta (e.g. anti-ferromagnetism). Therefore, in addition identifying the ferromagnetic region of the the phase diagram, we can use the one-magnon spectrum to identify promising candidates for the neighboring phases. Note that the calculated one-magnon spectrum is not applicable to states with more than one magnon, and therefore, strictly speaking talking about magnon condensation is not meaningful in this picture. However, at least close to the ferromagnetic state, the same one-magnon spectrum is in principle calculable using the Holstein-Primakoff approximation [1]. Within the Holstein-Primakoff approximation, the one-magnon spectrum is naturally extended to the entire many-body spectrum. Therefore, it is natural to justify magnon condensation scenarios from this point of view.

D.2 Ferromagnetism and its stability in the one dimensional Hubbard model

In this section we apply the machinery described so far the simple example of half-filled one dimensional Hubbard model,

$$H = t(\sum_{i,\sigma} c^{\dagger}_{i,\sigma} c_{i+1,\sigma} + h.c.) + U \sum_{i} n_{i,\uparrow} n_{i,\downarrow}. \tag{D.4}$$

The perfectly flat band limit in this case corresponds to the somewhat pathological case of $t = 0$. In this case, the system has a large 2^N dimensional grounsntate subspace (including the fully saturated ferromagnetic state) corresponding to filling only one electron per-site. In addition, we know that as the bandwidth t is increased,

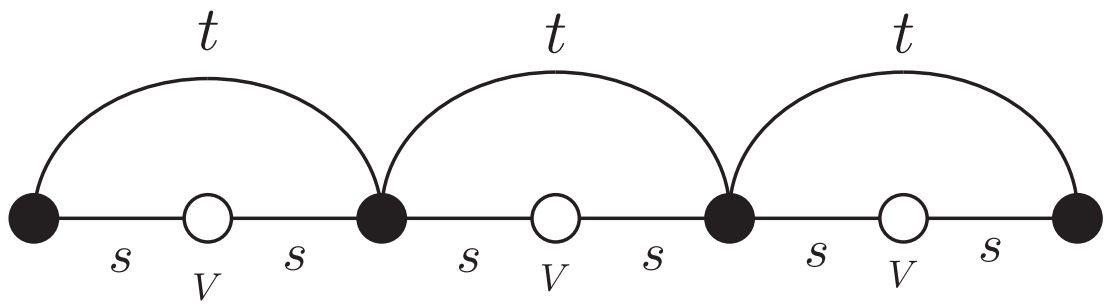

Figure D.2: Hopping parameters in the Tasaki model Eq.(D.6).

the ground state becomes anti-ferromagnetic. In fact this system does not exhibit ferromagnetism anywhere in its phase diagram.

To demonstrate validity of our formalism, it is important to show that we can get the same results with our approach. As described earlier, we do so by calculating the one-magnon spectrum of this model. That is, we consider states of the form,

$$|\psi^q\rangle = \sum_p \phi_p^q c_{p+q,\downarrow}^\dagger c_{p,\uparrow}^\dagger | \uparrow\uparrow \ldots \uparrow\rangle, \tag{D.5}$$

and calculate the lowest-band of energies associated with such excitations. Results of this calculation are shown in Fig.D.1. As shown in Fig.D.1, the ferromagnetic state $q = 0$, is in fact a local maximum for all values of U/t. That is, ferromagnetism is always unstable (spin-stiffness is negative), and therefore, the true ground-state of the system is never ferromagnetic. This results shows the effectiveness of our method in ruling out ferromagnetism in the one dimensional Hubbard model.

D.3 Ferromagnetism and its stability in the one-dimensional Tasaki model

We now consider the application of our formalism to the one dimensional model of Tasaki [113],

$$H = t\sum_{i,\sigma}(c^{\dagger}_{2i,\sigma}c_{2i+2,\sigma} + h.c.) + s\sum_{i,\sigma}(c^{\dagger}_{i,\sigma}c_{i+1,\sigma} + h.c.) \tag{D.6}$$
$$+ V\sum_{i,\sigma} n_{2i+1,\sigma} + U\sum_{i} n_{i,\uparrow}n_{i,\downarrow}$$

This model provides the simplest example of stable flat band ferromagnetism in one-dimension. A pictorial representation of the model and model and hopping parameters is shown in Fig.D.2 . Note that since the unit cell is composed of two-sites, this model has two bands.

It is convenient to introduce auxiliary parameters λ and ρ,

$$s = \lambda t \;\; ; \;\; V = (\lambda^2 - 2 + \rho)t. \tag{D.7}$$

If we set $\rho = 0$, the lowest band becomes perfectly flat. Roughly speaking, the parameters $|\rho|t$ and $\lambda^2 t$ set the band width and the band gap of the spectrum. In the flat band limit $\rho = 0$ and at half filling, the ground state is a saturated ferromagnet. As the bandwidth is increased, the (saturated) ferromagnetic phase persists for a finite region. In the opposite limit where the the interaction strength U is smaller than the bandwidth, the ground state is know to be a total spin singlet [113]. Therefore, as the bandwidth is increased from zero, the system goes from a ferromagnet to a singlet state.

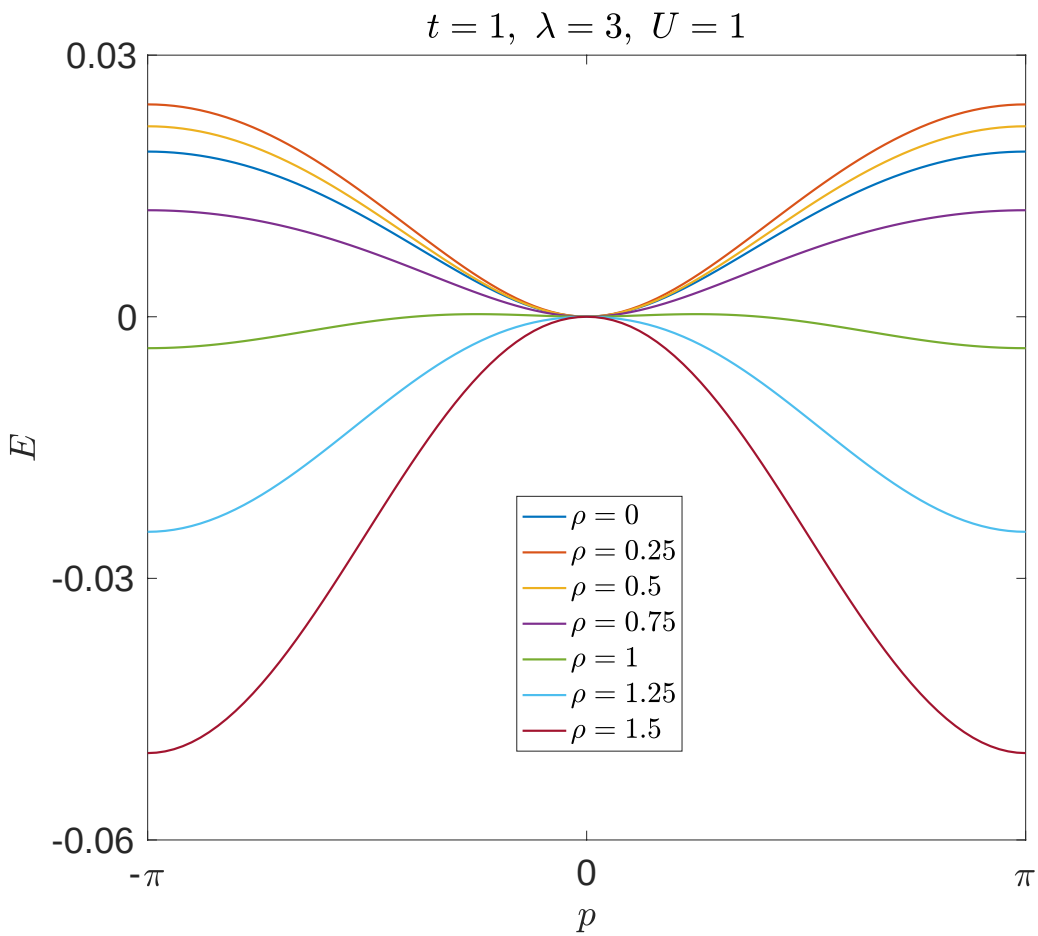

Figure D.3: Lowest one-magnon band energy for the one dimensional Tasaki model in Eq.(D.6).

Similar to the Hubbard model, we calculate the one magnon spectrum as the band-width is increased. The calculated one-magnon spectrum is plotted is Fig.D.3. As shown in the figure, the ferromagnetic states goes from a local minima (stable ferromagnetism) to a local maxima (unstable ferromagnetism) as the bandwidth is increased. Our results match the known analytic expression of spin-stiffness in the large band gap ($\lambda^2 t$) limit [113].

List of Publications

Publications this thesis is based on:

1. Ferromagnetism and its stability from the one-magnon spectrum in twisted bilayer graphene - Yahya Alavirad and Jay D. Sau, arXiv:1907.13633

2. Chiral supercurrent through a quantum Hall weak link - Yahya Alavirad, Junhyun Lee, Ze-Xun Lin and Jay D. Sau, Physical Review B 98 (21), 214504 (2018)

3. $\mathbb{Z}_3$ parafermionic zero modes without Andreev backscattering from the 2/3 fractional quantum Hall state - Yahya Alavirad, David Clarke, Amit Nag and Jay D. Sau, Physical Review Letters 119, 217701 (2017)

4. Role of boundary conditions, topology and disorder in the chiral magnetic effect in Weyl semimetals - Yahya Alavirad and Jay D. Sau, Physical Review B 94, 115160 (2016)

Other publications and preprints that I contributed to:

1. Measurement-induced topological entanglement transitions in symmetric random quantum circuits - Ali Lavasani, Yahya Alavirad and Maissam Barkeshli arXiv:2004.07243

2. Anomalies and unnatural stability of multi-component Luttinger liquids in $\mathbb{Z}_n \times \mathbb{Z}_n$ spin chains - Yahya Alavirad and Maissam Barkeshli, arXiv:1910.00589

3. Almost linear Haldane pseudopotentials and emergent conformal block wavefunctions in a Landau level - Yahya Alavirad, Phys. Rev. B 100, 075122 (2019)

4. Scrambling in the Dicke model - Yahya Alavirad and Ali Lavasani, Physical Review A 99 (4), 043602 (2019)

5. Spin-orbit coupled bosons in one dimension: emergent gauge field and Lifshitz transition - William S. Cole, Junhyun Lee, Khan W. Mahmud, Yahya Alavirad, I. B. Spielman and Jay D. Sau, Scientific Reports 9 (1), 7471 (2019)

6. Global phase diagram of a three dimensional dirty topological superconductor - Bitan Roy, Yahya Alavirad and Jay D. Sau, Physical Review Letters 118, 227002 (2017)

Bibliography

[1] G. D. Mahan, *Many-Particle Physics* (Springer Science & Business Media, 2000).

[2] W. Su, J. Schrieffer, and A. J. Heeger, Physical review letters **42**, 1698 (1979).

[3] K. Von Klitzing, Reviews of Modern Physics **58**, 519 (1986).

[4] C. Nayak, S. H. Simon, A. Stern, M. Freedman, and S. Das Sarma, Rev. Mod. Phys. **80**, 1083 (2008).

[5] Y. Alavirad and J. D. Sau, Phys. Rev. B **94**, 115160 (2016).

[6] Y. Alavirad, D. Clarke, A. Nag, and J. D. Sau, Phys. Rev. Lett. **119**, 217701 (2017).

[7] Y. Alavirad, J. Lee, Z.-X. Lin, and J. D. Sau, Phys. Rev. B **98**, 214504 (2018).

[8] Y. Alavirad and J. D. Sau, Ferromagnetism and its stability from the one-magnon spectrum in twisted bilayer graphene, 2019, arXiv:1907.13633.

[9] A. A. Burkov, Journal of physics. Condensed matter : an Institute of Physics journal **27**, 113201 (2015).

[10] P. Hosur and X. Qi, Comptes Rendus Physique **14**, 857 (2013).

[11] G. Xu, H. Weng, Z. Wang, X. Dai, and Z. Fang, Physical Review Letters **107**, 186806 (2011).

[12] X. Wan, A. M. Turner, A. Vishwanath, and S. Y. Savrasov, Physical Review B **83**, 205101 (2011).

[13] A. Sekine and K. Nomura, (2015), arXiv:1508.04590.

[14] S.-Y. Xu *et al.*, Science **349**, 613 (2015).

[15] B. Lv *et al.*, Physical Review X **5**, 031013 (2015).

[16] L. Lu *et al.*, Science **349**, 622 (2015).

[17] Z. K. Liu *et al.*, Nature materials **13**, 677 (2014).

[18] S. Borisenko *et al.*, Physical Review Letters **113**, 027603 (2014).

[19] S.-Y. Xu *et al.*, Science (New York, N.Y.) **347**, 294 (2015).

[20] A. C. Potter, I. Kimchi, and A. Vishwanath, Nature communications **5**, 5161 (2014).

[21] F. D. M. Haldane, (2014), arXiv:1401.0529.

[22] G. Xu, H. Weng, Z. Wang, X. Dai, and Z. Fang, Physical Review Letters **107**, 1 (2011), 1106.3125.

[23] S. Jeon *et al.*, Nature materials **13**, 851 (2014).

[24] H. Nielsen and M. Ninomiya, Physics Letters B **130**, 389 (1983).

[25] M. M. Vazifeh and M. Franz, Physical Review Letters **111**, 027201 (2013).

[26] P. Goswami and S. Tewari, arXiv **2**, 8 (2013), 1311.1506.

[27] J.-H. Zhou, H. Jiang, Q. Niu, and J.-R. Shi, Chinese Physics Letters **30**, 027101 (2013), arXiv:1211.0772v1.

[28] M.-C. Chang and M.-F. Yang, Physical Review B **91**, 1 (2015).

[29] Y. Chen, S. Wu, and a. a. Burkov, Physical Review B - Condensed Matter and Materials Physics **88**, 1 (2013), 1306.5344.

[30] G. Baar, D. E. Kharzeev, and H. U. Yee, Physical Review B - Condensed Matter and Materials Physics **89**, 1 (2014), 1305.6338.

[31] K. Landsteiner, Physical Review B - Condensed Matter and Materials Physics **89**, 1 (2014), 1306.4932.

[32] A. Zyuzin and A. A. Burkov, Physical Review B - Condensed Matter and Materials Physics **86**, 1 (2012), 1206.1868.

[33] A. G. Grushin, Physical Review D - Particles, Fields, Gravitation and Cosmology **86**, 1 (2012), 1205.3722.

[34] N. Yamamoto, Physical Review D **92**, 085011 (2015).

[35] J. Ma and D. A. Pesin, (2015), arXiv:1510.01304.

[36] S. Zhong, J. Moore, and I. Souza, (2015), arXiv:1510.02167.

[37] P. Goswami and S. Tewari, Physical Review B - Condensed Matter and Materials Physics **88**, 1 (2013), 1210.6352.

[38] M.-C. Chang and M.-F. Yang, (2015), arXiv:1508.05187.

[39] A. M. Essin, J. E. Moore, and D. Vanderbilt, Physical Review Letters **102**, 10 (2009), 0810.2998.

[40] P. Baireuther, J. A. Hutasoit, J. Tworzyd?o, and C. W. J. Beenakker, (2015), arXiv:1512.02144.

[41] J. R. Schrieffer, *Theory of Superconductivity* (Advanced Book Program, Perseus Books, 1983).

[42] E. Fradkin, *Field Theories of Condensed Matter Physics* (Cambridge University Press, 2013).

[43] A. Y. Kitaev, Physics-Uspekhi **44**, 131 (2001).

[44] J. Alicea, Reports on Progress in Physics **75**, 076501 (2012).

[45] M. Leijnse and K. Flensberg, Semiconductor Science and Technology **27**, 124003 (2012).

[46] C. Beenakker, Annual Review of Condensed Matter Physics **4**, 113 (2013).

[47] T. D. Stanescu and S. Tewari, Journal of Physics: Condensed Matter **25**, 233201 (2013).

[48] S. R. Elliott and M. Franz, Rev. Mod. Phys. **87**, 137 (2015).

[49] J. D. Sau, R. M. Lutchyn, S. Tewari, and S. Das Sarma, Phys. Rev. Lett. **104**, 040502 (2010).

[50] J. Alicea, Phys. Rev. B **81**, 125318 (2010).

[51] R. M. Lutchyn, J. D. Sau, and S. Das Sarma, Phys. Rev. Lett. **105**, 077001 (2010).

[52] Y. Oreg, G. Refael, and F. von Oppen, Phys. Rev. Lett. **105**, 177002 (2010).

[53] H.-H. Sun *et al.*, Phys. Rev. Lett. **116**, 257003 (2016).

[54] A. D. K. Finck, D. J. Van Harlingen, P. K. Mohseni, K. Jung, and X. Li, Phys. Rev. Lett. **110**, 126406 (2013).

[55] H. O. H. Churchill *et al.*, Phys. Rev. B **87**, 241401 (2013).

[56] A. Das *et al.*, Nat Phys **8**, 887 (2012).

[57] M. T. Deng *et al.*, Nano Letters **12**, 6414 (2012).

[58] V. Mourik *et al.*, Science **336**, 1003 (2012).

[59] H. Zhang *et al.*, Ballistic majorana nanowire devices, 2016, arXiv:1603.04069.

[60] J. Alicea and P. Fendley, Annual Review of Condensed Matter Physics **7**, 119 (2016).

[61] P. Fendley, Journal of Statistical Mechanics: Theory and Experiment **2012**, P11020 (2012).

[62] E. Fradkin and L. P. Kadanoff, Nuclear Physics B **170**, 1 (1980).

[63] L. Fidkowski and A. Kitaev, Phys. Rev. B **83**, 075103 (2011).

[64] A. M. Turner, F. Pollmann, and E. Berg, Phys. Rev. B **83**, 075102 (2011).

[65] D. J. Clarke, J. Alicea, and K. Shtengel, Nat Commun **4**, 1348 (2013).

[66] N. H. Lindner, E. Berg, G. Refael, and A. Stern, Phys. Rev. X **2**, 041002 (2012).

[67] M. Cheng, Phys. Rev. B **86**, 195126 (2012).

[68] M. Barkeshli and X.-L. Qi, Phys. Rev. X **2**, 031013 (2012).

[69] L. Fu and C. L. Kane, Phys. Rev. Lett. **100**, 096407 (2008).

[70] F. Amet *et al.*, Science **352**, 966 (2016).

[71] Z. Wan *et al.*, Nature communications **6** (2015).

[72] G.-H. Lee *et al.*, Inducing superconducting correlation in quantum hall edge states, 2016.

[73] H.-Y. Hui, J. D. Sau, and S. Das Sarma, Phys. Rev. B **90**, 064516 (2014).

[74] X.-G. Wen, *Quantum field theory of many-body systems: from the origin of sound to an origin of light and electrons* (Oxford University Press on Demand, 2004).

[75] X.-G. Wen, Advances in Physics **44**, 405 (1995).

[76] X.-G. Wen, Phys. Rev. B **41**, 12838 (1990).

[77] S. Bravyi, D. P. DiVincenzo, and D. Loss, Annals of Physics **326**, 2793 (2011).

[78] T. Giamarchi, *Quantum physics in one dimension* (Oxford university press, 2004).

[79] `http://itensor.org/`.

[80] The ground state energy splitting in expected to scale as $e^{-\xi/L}$ where ξ is the correlation length and l is the system size.

[81] S. Ganeshan and M. Levin, Phys. Rev. B **93**, 075118 (2016).

[82] $\alpha_{2j-1} = \sigma_j \prod_{i<j} \tau_i; \alpha_{2j} = -e^{i\pi/3}\tau_j\sigma_j \prod_{i<j} \tau_i$ where $\tau = \begin{pmatrix} 0 & 0 & 1 \\ 1 & 0 & 0 \\ 0 & 1 & 0 \end{pmatrix}$ is the "clock shift operator" and σ is defined in the main text.

[83] M. Barkeshli and X.-L. Qi, Phys. Rev. X **4**, 041035 (2014).

[84] M. Barkeshli, C.-M. Jian, and X.-L. Qi, Phys. Rev. B **88**, 241103 (2013).

[85] I. C. Fulga, A. Haim, A. R. Akhmerov, and Y. Oreg, New Journal of Physics **15**, 045020 (2013).

[86] J. Sau and S. Das Sarma, Nature communications **3**, 964 (2012).

[87] Y. Alavirad, D. Clarke, A. Nag, and J. D. Sau, Phys. Rev. Lett. **119**, 217701 (2017).

[88] M. Ma and A. Y. Zyuzin, EPL (Europhysics Letters) **21**, 941 (1993).

[89] J. A. M. van Ostaay, A. R. Akhmerov, and C. W. J. Beenakker, Phys. Rev. B **83**, 195441 (2011).

[90] M. Stone and Y. Lin, Phys. Rev. B **83**, 224501 (2011).

[91] M. P. A. Fisher, Phys. Rev. B **49**, 14550 (1994).

[92] H. Hoppe, U. Zülicke, and G. Schön, Phys. Rev. Lett. **84**, 1804 (2000).

[93] Y. Takagaki, Phys. Rev. B **57**, 4009 (1998).

[94] N. M. Chtchelkatchev, Journal of Experimental and Theoretical Physics Letters **73**, 94 (2001).

[95] T. D. Moore and D. A. Williams, Phys. Rev. B **59**, 7308 (1999).

[96] J. Eroms, D. Weiss, J. D. Boeck, G. Borghs, and U. Zülicke, Phys. Rev. Lett. **95**, 107001 (2005).

[97] U. Zlicke, H. Hoppe, and G. Schon, Physica B: Condensed Matter **298**, 453 (2001), International Conference on High Magnetic Fields in Semiconductors.

[98] Y. Ishikawa and H. Fukuyama, Journal of the Physical Society of Japan **68**, 954 (1999), https://doi.org/10.1143/JPSJ.68.954.

[99] F. Amet *et al.*, Science **352**, 966 (2016).

[100] G.-H. Lee *et al.*, Nature Physics **13**, 693 EP (2017), Article.

[101] A. W. Draelos *et al.*, (2018), arXiv:1801.01447.

[102] G.-H. Park, M. Kim, K. Watanabe, T. Taniguchi, and H.-J. Lee, Scientific reports **7**, 10953 (2017).

[103] J. P. Heida, B. J. van Wees, T. M. Klapwijk, and G. Borghs, Phys. Rev. B **57**, R5618 (1998).

[104] V. Barzykin and A. M. Zagoskin, Superlattices and Microstructures **25**, 797 (1999).

[105] T. D. Stanescu, J. D. Sau, R. M. Lutchyn, and S. Das Sarma, Phys. Rev. B **81**, 241310 (2010).

[106] S. Hart *et al.*, Nature Physics **10**, 638 (2014).

[107] J. Kanamori, Progress of Theoretical Physics **30**, 275 (1963).

[108] J. Stohr and H. C. Siegmann, Solid-State Sciences. Springer, Berlin, Heidelberg (2006).

[109] J. Hubbard and B. H. Flowers, Proceedings of the Royal Society of London. Series A. Mathematical and Physical Sciences **276**, 238 (1963).

[110] Y. Nagaoka, Phys. Rev. **147**, 392 (1966).

[111] D. J. Thouless, Proceedings of the Physical Society **86**, 893 (1965).

[112] E. H. Lieb, Phys. Rev. Lett. **62**, 1201 (1989).

[113] H. Tasaki, Journal of Statistical Physics **84**, 535 (1996).

[114] A. Mielke, Journal of Physics A: Mathematical and General **24**, L73 (1991).

[115] A. Mielke, Journal of Physics A: Mathematical and General **24**, 3311 (1991).

[116] A. Mielke, Physics Letters A **174**, 443 (1993).

[117] A. Mielke, Journal of Physics A: Mathematical and General **25**, 4335 (1992).

[118] A. Mielke and H. Tasaki, Communications in Mathematical Physics **158**, 341 (1993).

[119] H. Tasaki, Phys. Rev. Lett. **69**, 1608 (1992).

[120] H. Tasaki, Phys. Rev. Lett. **73**, 1158 (1994).

[121] H. Tasaki, Phys. Rev. Lett. **75**, 4678 (1995).

[122] H. Tasaki, Progress of Theoretical Physics **99**, 489 (1998).

[123] H. Katsura, I. Maruyama, A. Tanaka, and H. Tasaki, EPL (Europhysics Letters) **91**, 57007 (2010).

[124] H. Tasaki, The European Physical Journal B **64**, 365 (2008).

[125] A. Tanaka and H. Tasaki, Phys. Rev. Lett. **98**, 116402 (2007).

[126] B. Hunt *et al.*, Science **340**, 1427 (2013).

[127] Y. Cao *et al.*, Nature **556**, 43 EP (2018), Article.

[128] Y. Cao *et al.*, Nature **556**, 80 EP (2018).

[129] M. Yankowitz *et al.*, Science **363**, 1059 (2019).

[130] A. Kerelsky *et al.*, Magic angle spectroscopy, 2018, arXiv:1812.08776.

[131] Y. Choi *et al.*, Imaging electronic correlations in twisted bilayer graphene near the magic angle, 2019, arXiv:1901.02997.

[132] A. L. Sharpe *et al.*, Emergent ferromagnetism near three-quarters filling in twisted bilayer graphene, 2019, arXiv:1901.03520.

[133] S. Moriyama *et al.*, Observation of superconductivity in bilayer graphene/hexagonal boron nitride superlattices, 2019, arXiv:1901.09356.

[134] X. Lu *et al.*, Superconductors, orbital magnets, and correlated states in magic angle bilayer graphene, 2019, arXiv:1903.06513.

[135] C. Shen *et al.*, Observation of superconductivity with tc onset at 12k in electrically tunable twisted double bilayer graphene, 2019, arXiv:1903.06952.

[136] X. Liu *et al.*, Spin-polarized correlated insulator and superconductor in twisted double bilayer graphene, 2019, arXiv:1903.08130.

[137] G. Chen *et al.*, Tunable correlated chern insulator and ferromagnetism in trilayer graphene/boron nitride moir superlattice, 2019, arXiv:1905.06535.

[138] Y. Cao *et al.*, Electric field tunable correlated states and magnetic phase transitions in twisted bilayer-bilayer graphene, 2019, arXiv:1903.08596.

[139] Y. Cao *et al.*, Electric field tunable correlated states and magnetic phase transitions in twisted bilayer-bilayer graphene, 2019, arXiv:1903.08596.

[140] C. Shen *et al.*, Observation of superconductivity with tc onset at 12k in electrically tunable twisted double bilayer graphene, 2019, arXiv:1903.06952.

[141] M. Serlin *et al.*, Intrinsic quantized anomalous hall effect in a moir heterostructure, 2019, arXiv:1907.00261.

[142] G. Tarnopolsky, A. J. Kruchkov, and A. Vishwanath, Phys. Rev. Lett. **122**, 106405 (2019).

[143] E. Khalaf, A. J. Kruchkov, G. Tarnopolsky, and A. Vishwanath, Magic angle hierarchy in twisted graphene multilayers, 2019, arXiv:1901.10485.

[144] F. Haddadi, Q. Wu, A. J. Kruchkov, and O. V. Yazyev, Moir flat bands in twisted double bilayer graphene, 2019, arXiv:1906.00623.

[145] Y.-H. Zhang, D. Mao, and T. Senthil, Twisted bilayer graphene aligned with hexagonal boron nitride: Anomalous hall effect and a lattice model, 2019, arXiv:1901.08209.

[146] N. Bultinck, S. Chatterjee, and M. P. Zaletel, Anomalous hall ferromagnetism in twisted bilayer graphene, 2019, arXiv:1901.08110.

[147] R. Bistritzer and A. H. MacDonald, Proceedings of the National Academy of Sciences **108**, 12233 (2011).

[148] J. M. B. Lopes dos Santos, N. M. R. Peres, and A. H. Castro Neto, Phys. Rev. B **86**, 155449 (2012).

[149] M. Koshino *et al.*, Phys. Rev. X **8**, 031087 (2018).

[150] M. Yankowitz *et al.*, Nature **557**, 404 (2018).

[151] A. A. Zibrov *et al.*, Nature Physics **14**, 930 (2018).

[152] H. Kim *et al.*, Nano Letters **18**, 7732 (2018), PMID: 30457338.

[153] H. C. Po, L. Zou, A. Vishwanath, and T. Senthil, Phys. Rev. X **8**, 031089 (2018).

[154] N. F. Q. Yuan and L. Fu, Phys. Rev. B **98**, 045103 (2018).

[155] H. C. Po, H. Watanabe, and A. Vishwanath, Phys. Rev. Lett. **121**, 126402 (2018).

[156] H. C. Po, L. Zou, T. Senthil, and A. Vishwanath, Phys. Rev. B **99**, 195455 (2019).

[157] K. Hejazi, C. Liu, H. Shapourian, X. Chen, and L. Balents, Phys. Rev. B **99**, 035111 (2019).

[158] Z. Song *et al.*, All "magic angles" are "stable" topological, 2018, arXiv:1807.10676.

[159] S. Carr, S. Fang, Z. Zhu, and E. Kaxiras, An exact continuum model for low-energy electronic states of twisted bilayer graphene, 2019, arXiv:1901.03420.

[160] Z. Ma *et al.*, Topological flat bands in twisted trilayer graphene, 2019, arXiv:1905.00622.

[161] E. H. Hwang and S. D. Sarma, Impurity scattering induced carrier transport in twisted bilayer graphene, 2019, arXiv:1907.02856.

[162] F. Wu, E. Hwang, and S. Das Sarma, Phys. Rev. B **99**, 165112 (2019).

[163] J. Kang and O. Vafek, Phys. Rev. X **8**, 031088 (2018).

[164] J. M. Pizarro, M. Rsner, R. Thomale, R. Valent, and T. O. Wehling, Internal screening and dielectric engineering in magic-angle twisted bilayer graphene, 2019, arXiv:1904.11765.

[165] E. H. Hwang and S. Das Sarma, Phys. Rev. B **75**, 205418 (2007).

[166] Y.-H. Zhang, D. Mao, Y. Cao, P. Jarillo-Herrero, and T. Senthil, Phys. Rev. B **99**, 075127 (2019).

[167] M. Xie and A. H. MacDonald, On the nature of the correlated insulator states in twisted bilayer graphene, 2018, arXiv:1812.04213.

[168] S. Liu, E. Khalaf, J. Y. Lee, and A. Vishwanath, Nematic topological semimetal and insulator in magic angle bilayer graphene at charge neutrality, 2019, arXiv:1905.07409.

[169] F. Wu and S. D. Sarma, Ferromagnetism and superconductivity in twisted double bilayer graphene, 2019, arXiv:1906.07302.

[170] J. Kang and O. Vafek, Phys. Rev. Lett. **122**, 246401 (2019).

[171] S. L. Sondhi, A. Karlhede, S. A. Kivelson, and E. H. Rezayi, Phys. Rev. B **47**, 16419 (1993).

[172] K. Yang *et al.*, Phys. Rev. Lett. **72**, 732 (1994).

[173] K. Moon *et al.*, Phys. Rev. B **51**, 5138 (1995).

[174] D. P. Arovas, A. Karlhede, and D. Lilliehöök, Phys. Rev. B **59**, 13147 (1999).

[175] J. Alicea and M. P. A. Fisher, Phys. Rev. B **74**, 075422 (2006).

[176] K. Yang, S. Das Sarma, and A. H. MacDonald, Phys. Rev. B **74**, 075423 (2006).